Structural models of the manganese complex of Photosystem II and mechanistic implications

Alexander Grundmeier and Holger Dau*

Freie Universität Berlin, FB Physik Arnimallee 14, D-14195 Berlin, Germany

**correspondence to*

Prof. Holger Dau
Freie Universität Berlin, FB Physik
Arnimallee 14, D-14195 Berlin, Germany
Phone: +49-(0)30-838-53581, Fax: +49-(0)30-838-56299
E-mail: holger.dau@physik.fu-berlin.de

Keywords manganese complex, oxygen evolution, photosynthesis, crystal structure, water oxidation, X-ray absorption spectroscopy

Abstract. Photosynthetic water oxidation and O_2 formation is catalyzed by a Mn_4Ca complex bound to the proteins of photosystem II (PSII). The catalytic site, including the inorganic $Mn_4CaO_nH_x$ core and its protein environment, is denoted as oxygen-evolving complex (OEC). Earlier and recent progress in the endeavor to elucidate the structure of the OEC is reviewed, with focus on recent results obtained by (i) X-ray spectroscopy (specifically by EXAFS analyses), and (ii) X-ray diffraction (XRD, protein crystallography). Very recently, an impressive resolution of 1.9 Å has been achieved by XRD. Most likely however, all XRD data on the $Mn_4CaO_nH_x$ core of the OEC are affected by X-ray induced modifications (radiation damage). Therefore and to address (important) details of the geometric and electronic structure of the OEC, a combined analysis of XRD and XAS data has been approached by several research groups. These efforts are reviewed and extended using an especially comprehensive approach. Taking into account XRD results on the protein environment of the inorganic core of the Mn complex, 12 alternative OEC models are considered and evaluated by quantitative comparison to (i) extended-range EXAFS data, (ii) polarized EXAFS of partially oriented PSII membrane particles, and (iii) polarized EXAFS of PSII crystals. We conclude that there is a class of OEC models that is in good agreement with both the recent crystallographic models and the XAS data. On these grounds, mechanistic implications for the O-O bond formation chemistry are discussed.

1. Introduction

Powered by solar energy, plants and cyanobacteria oxidize water thereby providing the electrons (reducing equivalents) and protons needed for the reduction of carbon dioxide and eventually carbohydrate formation. The process of water oxidation is essential in photosynthesis and thus primary biomass formation. It has shaped the atmosphere by formation of molecular oxygen and is currently of special interest as a model or inspiration for future technological systems that might allow for the production of 'solar fuels' [1-7].

Photosynthetic water oxidation is catalyzed by a Mn_4Ca complex bound to the proteins of photosystem II (PSII), a cofactor-protein complex of impressive size and complexity. In intact organisms and in preparations of PSII-containing membrane particles, the PSII complex is embedded in a lipid bilayer membrane, the thylakoid membrane [8-9]. There are numerous fascinating facets of PSII, which are reviewed in the various articles of this special issue. We will describe recent progress in the endeavor to elucidate the structure of the catalytic site of PSII water oxidation, which mostly is denoted either as oxygen-evolving complex (OEC) or simply as manganese complex (Mn complex) [10-13]. Besides reviewing and evaluating alternative structural models, the role of the OEC structure for the mechanism of PSII water oxidation is addressed.

Today, it is well established that the OEC consists of four manganese and one calcium ion which are bound to specific (ionic) amino-acid residues of the PSII proteins (see figures discussed further below). Various experimental methods have been used for insight in the structure of the OEC, among others electron paramagnetic resonance (EPR) and electron nuclear double-resonance (ENDOR) spectroscopy [14-25] Fourier-transform infrared (FTIR) spectroscopy [26-29], X-ray absorption spectroscopy (XAS) [13, 30-35] and X-ray diffraction (XRD) on PSII crystals (protein crystallography) [36-44]. We will focus on findings obtained by the latter two methods, X-ray spectroscopy (XAS) and protein crystallography (XRD), and only occasionally refer to results of EPR and FTIR investigations.

Instead of XAS, often the acronyms XAFS (X-ray absorption fine-structure) or EXAFS (extended XAFS) are used. The EXAFS is the oscillatory fine-structure detectable to up to about 1000 eV after the rising part of the X-ray edge [45]. EXAFS analysis is the primary structural tool in X-ray spectroscopy [46]. It can facilitate the determination of (average) Mn-ligand distance at an accuracy of up to 0.02 Å. The XAS or XAFS data comprise the EXAFS as well as the edge-rise, the latter being related to the metal coordination geometry of the X-ray absorbing metal, its electronic structure and specifically its oxidation state. The edge region of the X-ray absorption spectrum also is denoted as X-ray absorption near-edge structure (XANES). The methodical aspects of the analysis of EXAFS and XANES spectra of the OEC have been reviewed elsewhere [47-49].

2. Structural models of the OEC

2.1. State-of-the-art in 2000

We will start by considering the state-of-the-art in the year 2000, before any crystallographic information became available. At that time, it was commonly believed that the OEC contained four manganese, one calcium and likely also one chloride ion [10-11, 50]; hypotheses on the amino acid residues of the D1 protein that might be Mn ligands had been developed on the basis of mutagenesis studies [51]. The XAS approach had been established as a highly useful approach for gaining insights in the OEC structure, in seminal studies by Klein, Sauer, Yachandra and their coworkers in Berkeley [10, 30, 32, 52]. On grounds of EXAFS

experiments, some early models had been rejected [10, 33, 53], specifically symmetric Mn_4O_n structures like butterfly and cubane arrangements (research groups of Christou and Dismukes [54-55]) or the cubane-adamantane model of Brudvig and Crabtree [56]. Mostly based on EPR and EXAFS results and comparison to synthetic model complexes [57-60], in 1992/93 the Berkeley group had proposed the so-called dimer-of-dimers model [32, 61-62], which, in 2000, not only had been employed in proposing and discussing mechanistic hypotheses but also had entered student textbooks.

In the dimer-of-dimer model (DoD), the Mn complex was assumed to be composed of two Mn 'dimers' each being a di-μ-oxo bridged Mn_2 unit (Fig. 1A). The evidence for two Mn—$(\mu_2\text{-O})_2$—Mn units came from EXAFS analysis indicating the presence of 2-3 vectors of ~2.72 Å length connecting Mn ions (Table 1), a distance that is characteristic for di-μ_2-oxo bridging between Mn^{III} or Mn^{IV} ions [57, 59], as discussed in [47]. (The symbol μ_2 indicates that the oxygen atoms are bridging between two transition metal ions, that is, two Mn ions.) In the DoD model, the two Mn—$(\mu_2\text{-O})_2$—Mn dimers are interconnected by mono-μ_2-oxo, bis-carboxylato bridging (3.3 Å distance between Mn ions, Table 1, Fig. 1A). The chloride ion was assumed to be a first-sphere ligand of a manganese ion (Cl bound to Mn^3 in Fig. 1A) and the Ca ion was put at a distance of about 3.4 Å to two Mn ions (Mn^1 and Mn^4), a Ca-Mn distance later confirmed in EXAFS investigations at the *K*-edge of calcium [63-64] and in an XAS study on cyanobacteria grown on media containing strontium instead of calcium [65-66]. The presence of a histidine ligand was concluded from pulsed EPR experiments [67].

When the DoD model was proposed in 1993, it was known from polarized EXAFS investigations on partially oriented PSII membrane particles that the two Mn-Mn vectors of about 2.7 Å length are at an average angle with respect to the membrane normal that exceeds the so-called magic angle of 54.7..° clearly [32, 68], a finding that has been repeatedly confirmed and detailed [34, 69-73]. Polarized EXAFS at the Sr *K*-edge (in PSII with Ca replaced by Sr) later yielded an angle between the membrane normal and Mn-Ca vector(s) clearly smaller than 55° [74], in line with the arrangement of metal ions of the DoD model depicted in Fig. 1A. The 3.3 Å Mn-Mn vector in Fig. 1A is aligned in parallel to the membrane normal; this suggestion was not confirmed in later polarized EXAFS investigations [73]. Moreover, also the presence of a chloride in the first coordination sphere of a manganese ion later has been disproven, as discussed further below.

We emphasize that the DoD model never was presented as a unique OEC model but merely was obtained as a chemically plausible combination of the necessarily fragmentary structural information obtained by XAS and other means. With the exception of the two points mentioned above (3.3 Å Mn-Mn distance and chloride ligand), the structural information used to construct this model is still valid and provides relevant constraints in the construction of OEC models. We note that, in XAS studies at room temperature, it was confirmed that the structural information obtained by experiments at cryogenic temperatures apply equally to the OEC at room temperature [75-78].

In 2000, Britt and coworkers concluded that their EPR data, specifically electron spin echo electron nuclear double resonance (ESE-ENDOR), are difficult to reconcile with the DoD model and they proposed the so-called *dangler* model (Fig. 1B), which represents an alternative arrangement of the buildings blocks previously used for the construction of the DoD model [79]. In the trimer-monomer arrangement of the dangler model, three Mn ions (Mn^1, Mn^2, and Mn^3 in Fig. 1B) are interconnected by di-μ-oxo bridges, so that they form a strongly exchange-coupled Mn_3 core; the fourth Mn ion (Mn^4, the 'dangler') is connected by a mono-μ-oxo bridge to the trinuclear core.

Especially eminent and inspiring among the various mechanistic proposals involving the DoD model had been the hydrogen-atom abstraction (HAA) model of Babcock and his coworkers [80-82]. In 1997, Hoganson and Babcock proposed that the two substrate water molecules are ligated to Mn^1 and Mn^4. At that time, it was already well established that, after light absorption by the PSII chlorophylls, a specific tyrosine (denoted a Tyr_Z or Y_Z), is rapidly oxidized and deprotonated; for details see contribution of S. Styring in this issue. Now Babcock and coworkers proposed that by oxidation and deprotonation a neutral Tyr_Z-radical is formed that abstracts H-atoms directly from the water species bound to the terminal Mn ions in the DoD model, Mn^1 and Mn^4, until eventually the O-O bond is formed between two Mn-oxo species ($Mn^1 = O \cdots O = Mn^4$). The example of the HAA model illustrates the close interrelation between structural and mechanistic models.

2.2. Protein crystallography and OEC structure

In 2001, Zouni, Fromme, Krauss, Saenger, Witt and coworkers (Berlin) presented the first crystallographic model with four Mn ions bound to the PSII proteins, at 3.8 Å resolution [36]. This breakthrough rooted, *inter alia*, in the use of PSII complexes prepared from a thermophilic cyanobacterium, that is *Synechococcus elongatus*, an organism with exceptional stability of its proteins. (Until today, all crystallographic models of Mn-containing PSII were obtained from thermophilic cyanobacteria.) At a resolution of 3.8 Å, Zouni *et al* [36] located the Mn complex and thus the amino acid residues in its environment, but could neither identify the ligands to the Mn complex nor the Ca ion. Two points were of special importance for models on structure and function of the OEC. Firstly, the blob of electron density assigned to the five metal ions was surprisingly compact. Its size essentially excluded the DoD or dangler arrangement shown in Fig. 1. Secondly, the distance between the Tyr_Z and the Mn complex was too large for direct abstraction of a hydrogen atom from a water species coordinated to a Mn ion. This means that two cornerstones of the H-atom abstraction (HAA) model of Babcock and coworkers were removed; the influential HAA model was no longer tenable. We note that, even though eventually invalidated, the hypothesis of Babcock has shaped the way researchers discuss the mechanism of water oxidation by emphasizing the necessity to understand the coupling of electron and proton transfer steps [13, 83-90]. In 2003, the results of Zouni *et al* were largely confirmed by Shen and his coworkers, at 3.7 Å resolution, and some protein ligands were identified [37].

In 2004, Barber and his coworkers in London (Ferreira, Iwata and others) presented a crystallographic model at 3.5 Å resolution [38]. By anomalous diffraction, they located the Ca ion at a distance of only 3-4 Å to three Mn ions, in agreement with the XAS results described above (see also Table 1). Thereby, it was firmly established that the tetranuclear Mn_4 complex indeed is a pentanuclear Mn_4Ca complex, as previously had been concluded from EXAFS results (as discussed further above). Moreover, Barber proposed that three Mn and the Ca ion form an elongated $CaMn_3(\mu\text{-}O)_4$ cubane together with four bridging oxygen atoms, as shown in Fig. 2. The fourth Mn ion (Mn^4 in Fig. 2) was connected to the cube by binding to one of the bridging oxygen atom, thereby becoming the 'dangler', in line with EPR results of Britt and coworkers [79]. The London group assigned several protein ligands and proposed a bicarbonate ligand (the bicarbonate is *not* shown in Fig. 2). All this could be done, at a resolution of 3.5 Å, only by combining crystallographic and spectroscopic results with inspired intuition. Later, the bicarbonate ligand was proven wrong and also the mode of protein ligation was only partially correct, whereas the $CaMn_3(\mu\text{-}O)_4$ proposed by Barber and coworkers is a feature of the OEC that largely has been confirmed (as discussed further below).

In 2005, the Berlin group headed by Zouni presented a PSII structure at 3.0 Å resolution [39]. Since at this resolution individual metal ions cannot be resolved and being aware of modifications in the electron density caused by X-ray exposure, Loll *et al* did not propose a specific structural model of the $Mn_4Ca(\mu\text{-}O)_n$ core of the metal complex. However, they could assign protein ligands clearly more reliable than previously possible. Eleven oxygen and one nitrogen ligand from amino acid residues of the D1 protein and the CP43 protein were identified as ligands of specific metal ions [42, 91]; only two of these later were assigned differently in the 1.9 Å structure of Shen and coworkers [44]. Figure 3 shows the ligation scheme of Loll *et al* in combination with a structural model of the metal-oxo core of the OEC developed by us [92] (and discussed in more detail further below). We note that the combination of the EXAFS-based model of the $Mn_4Ca(\mu\text{-}O)_n$ core with the crystallographic model of Loll *et al* implies a special role for Mn^4. It may bind the water substrate as only this Mn ion contains (two) terminally coordinated water molecules; one of these is in hydrogen bonding distance to the Asp61 of the D1 protein. Moreover the model implies that one water molecule bound to the Ca ion may participate in a branched hydrogen bond between Tyr_Z and His_{190}, as schematically shown in Fig. 3.

Other crystallographic studies addressed the location of the chloride cofactor. Employing the methodology developed for a vanadium peroxidase [93-94], in 2006 the chloride location was investigated by X-ray absorption spectroscopy at the bromine K-edge, after substitution of the chloride cofactor by bromide [95]. It was found that, as opposed to the OEC structure of Fig. 1, the halide cofactor is bound neither to a Mn nor to the Ca ion of the OEC [95]. In the following years, several crystallographic studies confirmed that the distance from bound halides to the metal ions of the OEC clearly exceeds 5 Å. One or two halides were found in the vicinity of the Mn complex; the locations detected in different studies were not always identical but often similar [40-42]. In a recent crystallographic study, preliminary evidence for two alternative locations of the same chloride ion were obtained (both at a distance from the OEC metal ions exceeding 5 Å) suggesting that also in functional PSII the chloride ion might move between different sites [43]. The role of the chloride ion either may be merely in optimizing the protein electrostatics or, more likely, it may be involved in controlling proton movements, *e.g.*, by tuning p*K* values [96]. In any event, all the above findings suggest that chloride is not directly involved in the chemical reactions taking place at the Mn complex. Consequently, the Mn complex is *not* a Mn_4CaCl complex, as previously often had been assumed.

At the international photosynthesis congress in 2010 (Beijing), Shen presented a stunning breakthrough in protein crystallography on PSII, namely a crystallographic model at 1.9 Å resolution [44]. At this resolution the binding mode of the protein-derived ligands can be literally seen in the electron density map, specifically the bridging between two metal ions by carboxylate groups versus monodentate binding to one metal ion only. Shen and coworkers (see Umena *et al* [44]) largely confirmed the ligand assignment of Loll *et al* [39], with two notable exceptions. In their structural model Asp170 is bridging between Mn and the Ca ion whereas Glu189 is not bridging between metal ions but merely a monodentate ligand to Mn^1. A comparison of the XRD models of Loll *et al* [39] and Umena *et al* [44] is facilitated by Fig. 5B (and Figs. S1, S2) and reveals that the differences in the position of the ligating residues are relatively small. Even the positions of Asp170 and Glu189 are not strikingly different. The difference in the ligation scheme of Loll *et al* (Asp170 … Ca—Glu189) and Umena *et al* (Asp170—Ca … Glu189) relates not only to the coordinates of Asp170 and Glu189 but also to the location of the Ca ion (see Fig. 5B).

The absence of pronounced differences in the positions of the residues surrounding the Mn complex is of relevance when judging the merits of the computational studies that employed

the coordinates *Loll et al* determined in 2005 [39]. Herein we describe and apply a specific protocol for development and evaluation of alternative OEC models (see section 3). As a starting point, we used the residue coordinates of Loll *et al* [39] and not the more precise coordinates of Umena *et al* [44]. In the course of the molecular modeling procedure, the starting coordinates were varied (see Figs. S8-S17). Consequently the outcome of the herein employed molecular modeling did not depend critically on the precise values of the starting coordinates. Therefore we believe that our conclusions are not affected seriously by the use of the less precise coordinates of Loll *et al*. (There is one notable exception. The difference in the ligation mode of Asp170 might affect the outcome of the herein used molecular modeling approach.)

In Umena *et al* [44], Shen and coworkers located, for the first time, the bridging oxygen atoms of the OEC core (O^a to O^e in Fig. 2). Another important progress had been the identification of numerous water molecules, around 1000 per PSII monomer. Hundreds of these are located in the 'protein matrix' at the lumenal side of PSII, which surrounds the OEC. Of special relevance could be the three hydrogen-bonded water molecules that connect the water coordinated to Mn^4 with a water molecule bound to the Ca ion and the H-bond between Tyr_Z and His_{190} (see also article by Styring, this issue). These water molecules in the second coordination sphere of the metal ions and the corresponding H-bond networks likely are of importance for the OEC function, as discussed further below. They also may affect the outcome of quantum chemical calculations that address mechanistic details.

2.3. Modifications by X-ray photoreduction (radiation damage)

In XAS studies on the Mn complex of PSII, we found that even at low temperatures (20 K) and relatively low doses (several orders of magnitudes below the level used in protein crystallography) the oxidation state of the Mn complex of PSII is modified, that is X-ray photoreduction of the Mn ions is observed [72, 78, 97]. On these grounds, we pointed out in 2004 [47] that the arrangement of metal ions in the OEC likely is affected by the exposure to the high doses of X-ray irradiation needed for crystallographic data collection on the PSII crystals. This means that the electron densities determined by the London group (Barber and coworkers) and the Berlin group (Zouni, Saenger and coworkers) mostly relate to a Mn complex which is reduced close to the all-Mn^{II} level, as confirmed in 2005 by a seminal XAS study on single-crystals of PSII [98]. This X-ray photoreduction of the metal ions represents a local radiation damage, affecting specifically the Mn complex due to the extraordinary electrophilicity of the high-valent manganese ions. A comprehensive investigation on X-ray induced modifications of the Mn complex PSII and a discussion of the underlying mechanisms has been presented elsewhere [99]; for a review comprising also the X-ray photoreduction phenomenon, see [13].

The most recent crystallographic model of Shen and his coworkers involved a protocol for data collection at the synchrotron radiation source that minimized the level of X-ray exposure [44]. However, it clearly has not been possible to avoid fully Mn photoreduction and concomitant modifications of bond lengths. Shen and coworkers could resolve all first-sphere ligands of the four Mn ions and determined Mn-ligand bond lengths that are clearly longer than predicted for the $Mn_4^{III,III,IV;IV}$ oxidation state of the Mn complex in its dark-stable S_1-state. Using bond-valence parameters of Brese and O'Keeffe [100-101], we estimated the oxidation state of the Mn ions in the crystallographic model of Umena *et al* [44] from the Mn-O bond lengths and obtained an average oxidation state of +2.5, which would correspond to a $Mn_4^{II,II,III,III}$ complex (see Table S2). This analysis suggests a reduction of the Mn complex by four electrons from the S_1-state prevalent in dark-adapted PSII to a reduced state that may be

denoted as S_{-3}. The calculated oxidation states for the individual Mn ions are: Mn^1, +2.8 (III); Mn^2, +2.7 (III); Mn^3, +2.5 (II); Mn^4, +2.1 (II), where the figures in parenthesis denote our oxidation-state estimate assuming fully localized valencies. We note that the herein used approach is highly approximative. The high resolution obtained by Shen and coworkers could facilitate new ways to address the radiation-induced modifications. Application of density functional theory (DFT) could result in an improved picture of the electronic structure in the Mn complex after X-ray exposure and its relation to the S_1-state structure.

Taking into account the estimated 4-electron reduction of the Mn complex, it does not surprise that also the Mn-Mn distances are modified by X-ray exposure. Only a single Mn-Mn vector of about 2.78 Å was identified in the crystallographic model, whereas the EXAFS clearly indicates the presence of (at least) two short Mn-Mn vectors (2.7 ± 0.4 Å) in the intact OEC in its dark-stable S_1-state [13, 30-35, 91, 102]. Because of the elongated Mn-O bonds and the loss of short Mn-Mn vectors, the EXAFS spectra calculated for the crystallographic model indeed are in stark disagreement with the experimental EXAFS (see Figs. S3, S4, S5).

Whereas the radiation-induced modifications of the atom coordinates of the Mn_4CaO_n core of the OEC is undisputable, it remains essentially unknown whether, and to what extent, the coordinates of nearby (ligating) residues are affected. On the one hand, at low temperatures (typically around 100 K during crystallographic data collection) the protein environment may be 'frozen' and thus the protein ligands (of the OEC) may be properly described by the crystallographic results. On the other hand, the X-ray exposure will create a highly energized situation. Each absorbed X-ray photon will create several hundred radicals [97]. Even at low temperatures, they could cause breaking of covalent bonds and possibly even result in the formation of gas molecules (O_2, H_2, CO_x). We believe that major modifications of the protein environment in the initial phase of X-ray photoreduction of the OEC cannot be excluded rigorously but that they are relatively unlikely.

2.4. Combining XAS and XRD data

Radiation damage is a potential problem not only in XRD but also in any XAS investigation on the OEC. Based on a quantitative assessment of the rate of X-ray photoreduction by XANES analysis, experimental protocols have been devised that limit the dose per irradiated area in XAS experiment such that the level of X-ray photoreduction is negligible (see Supporting Online Material of [78]). Therefore XAS data on the Mn complex of PSII—specifically in the EXAFS regime, which is very well understood on theoretical grounds [45, 103-111]— is well suited to support the development of structural OEC models. Taking into account the close relation between EXAFS data and geometric details of the OEC, on the one hand, and the limitations of the crystallographic data rooting in (i) limited resolution and (ii) radiation damage, on the other hand, several research groups approached the development of structural OEC models that are either based on XAS results or have been refined for agreement with selected XAS data sets.

In a joint effort of the XAS group in Berkeley (Yano, Yachandra, *et al*) and the protein crystallography group in Germany (Zouni, Saenger, Messinger, *et al*) polarized EXAFS data were collected on protein crystals and analyzed by comparative EXAFS simulations (see section 3, for further details) [91]. Mostly based on the thereby obtained results, Yano *et al* proposed four alternative (but similar) models for the $Mn_4(\mu\text{-}O)_n$ core of the OEC [91], which are schematically shown in Fig. 4. Yano *et al* used a radical approach with respect to radiation-induced modifications in the crystallographic model of the protein ligands. Assuming that severe modifications of the protein environment cannot be excluded, they did not take into account the crystallographic results when evaluating alternative OEC models.

Therefore, it does not come as a surprise that the four suggested models for structure and orientation (within the protein) of the OEC core are in more or less pronounced conflict with the crystallographic models of the protein environment of the OEC.

Batista, Brudvig, Sproviero and their coworkers developed structural models of the OEC in various states of its reaction cycle [12, 112-118]. They obtained structural models by means of DFT calculations (QM/MM methods were applied) using the crystallographic model of Ferreira *et al* [38] as a starting point. A geometry optimization by DFT calculations mostly results in structures that are close to the starting model. Consequently their favored OEC model is highly similar to the one proposed by Barber and coworkers (see Fig. 2). Recently they refined their OEC model by a small variation of the Mn-Mn distance such that good agreement with respect to the polarized EXAFS data collected on PSII crystals by Yano *et al* [91] was achieved [119].

Based on the ligand assignment of Loll *et al* [39] and on extended-range EXAFS data (see section 3), we proposed the structural model shown in Fig. 3 [13, 92]. Starting from the coordinates of the protein ligands of the crystallographic model, the model was obtained by a geometry optimization that was carried out using a classical molecular mechanics (MM) approach. The basic model of the $Mn_4Ca(\mu\text{-}O)_n$ core was derived from XAS results before starting the geometry optimization and introduced into the MM geometry optimization in form of additional constraints, as described further below (section 3). To account for the putative influence of radiation damage, significant deviations from the crystallographic model of Loll *et al* [39] were allowed for the protein environment of Mn^4. Moreover we assumed that Mn^1 is quasi-five-coordinated, meaning that O^a is at a distance to Mn^1 that exceeds 2.4 Å. This assumption roots in results that support a transition from five-coordinated Mn(III) to six-coordinated Mn(IV) in the $S_2 \rightarrow S_3$ transition of the reaction cycle [34, 48, 78, 120].

The model of Fig. 3 is similar to a model obtained by Siegbahn and coworkers by means of DFT calculations. Siegbahn also is assuming that Mn^1 is five-coordinated. Whereas we have proposed that the Jahn-Teller (JT) axis of Mn^1(III) is aligned along the O^a----Mn^1—N-His332 vector (extended Mn^1----O^a distance results in quasi five-coordinated Mn^1), Siegbahn finds by DFT calculations a direction of the JT axis along the O^d----Mn^1—O-Asp342 axis (extended Mn^1----O^d distance) [121-122]. Apart from this difference, the two OEC models are highly similar and both are close to the crystallographic model of Shen and coworkers (compare Fig. 3 and Fig. 5).

Each of OEC models shown in Figs. 2 to 4 was derived taking into account *some* EXAFS results. However, for each model holds that only a subset of the relevant EXAFS data sets was employed in model development or refinement. In the following, we will evaluate these and other OEC models by using a more comprehensive approach, that is, we will consider three types of EXAFS data sets: (i) extended range EXAFS spectra of isotropic samples, (ii) polarized EXAFS of partially oriented PSII membrane particles, and (iii) polarized EXAFS of PSII crystals.

3. Evaluation of alternative OEC models—methods

3.1. Experimental EXAFS spectra

To evaluate the validity of alternative structural models for the protein-bound Mn_4Ca complex, we used three types of EXAFS spectra, all collected at the *K*-edge of manganese, that is: (*Iso*) isotropic extended-range EXAFS of PSII membrane particles, (*Mem*) a set of

polarized EXAFS spectra for oriented PSII membrane particles, and (*Cry*) a set of polarized EXAFS spectra collected on single-crystals of dimeric PSII.

(*Iso*) *Isotropic extended-range EXAFS*. Using high-activity PSII membrane particles prepared from spinach [123], isotropic EXAFS spectra were collected; the resulting spectra are shown in [92]. In these experiments, EXAFS samples had been prepared by a centrifugation procedure [72, 124], which inevitably results in partial orientation of the PSII membrane particles. To obtain the isotropic EXAFS, that is the EXAFS spectra of PSII randomly oriented without any preferred orientation, spectra were collected at the so-called magic angle of linear dichroism spectroscopy (angle of about 54.7° between normal of the sample substrate and the electric field vector of the X-ray). To increase information content and distance-resolution, EXAFS data were collected for an extended data range of 1050 eV above the X-ray edge (16.5 $Å^{-1}$). In most EXAFS experiments, the used energy range extends up to 550 eV only (12 $Å^{-1}$) to avoid undesired contributions from the absorption edge of iron to the Mn-edge spectra. The approach used by us [92] to eliminate these contributions by means of a difference technique [125] is less elegant than an alternative approach described in [73, 126] but is more efficient and facilitates an especially good signal-to-noise ratio in the EXAFS data.

(*Mem*) *Polarized EXAFS of unidirectionally oriented membrane particles*. The first samples for these polarized EXAFS experiments were thylakoid membranes containing PSII, PSI and other protein complexes [68]. Later PSII membrane particles obtained by modifications of the so-called BBY protocol [127] have been prepared mostly from spinach but also from green alga [72, 123]. The preparation of PSII particles was followed by orientation of the membranes either by a paint-and-dry procedure [69, 71] or by a specific centrifugation protocol [72, 124]. Orientation also has been achieved for dimeric PSII core particles, but only a relatively imperfect orientation was achieved for the PSII particles (unpublished). In all experiments, the normal of the PSII-containing lipid bilayer membrane (*M* in Fig. 6A) was preferentially in parallel to the normal of the macroscopic sample holder (*S*). The achieved orientation is imperfect (partial orientation, mosaic spread) and mostly described by a Gaussian distribution function; the previously used approach of Blum *et al* [128] is corrected in [72]. Using these partially oriented samples, spectra were collected at distinct angles between the macroscopic sample normal (*S*) and the electric field vector (*E*-field vector, *E*) of the linearly polarized X-rays provided by a synchrotron radiation source. Due to the employment of partially oriented or ordered samples in combination with linearly polarized electromagnetic radiation, the described methodical approach can be denoted as linear dichroism (LD) spectroscopy. In the field of X-ray absorption spectroscopy on biological samples, the informal expression ‘polarized EXAFS’ is used more frequently.

Herein, we analyze EXAFS spectra collected at four excitation angles, namely 15°, 35°, 55°, and 75°. To improve the signal-to-noise ratio, the data sets described in [72] and [129] were averaged. These spectra cover an energy range up to 510 eV (11.6 $Å^{-1}$) above the edge. For the assessment of the validity of alternative structural models, the spectrum collected at 55° was replaced by the extended-range EXAFS spectrum obtained as described above.

(*Cry*) *Polarized EXAFS of PSII crystals.* Yano, Yachandra and their coworkers collected EXAFS spectra for single crystals of dimeric PSII [91]. In an extraordinary difficult set of experiments, they measured EXAFS spectra with the X-ray electric field vector in parallel to each of the three unit-cell axes (*a*, *b*, and *c*). The space group of the crystals was $P2_12_12_1$ (see Fig.6B). There are eight PSII monomers, each with a distinct orientation with respect to the crystal axis. This geometric complexity renders it impossible to ‘deduce’ structural information directly from the LD-EXAFS of the PSII crystal. Therefore, Yano *et al* [91] used the following approach: They constructed an extended set of hypothetical models of the

Mn_4Ca complex of PSII and evaluated whether or not, for any orientation of the respective structural model, the three calculated EXAFS spectra match the three experimental spectra detected for excitation along the *a*, *b*, and *c* axes. In our study, a similar approach is used for evaluation of alternative structural models. For quantitative comparison to simulated EXAFS spectra, herein the Fourier-transformed EXAFS spectra of Yano *et al* [91] were digitized and rescaled.

3.2. Simulations of EXAFS spectra

Linear dichroism. EXAFS spectra on a *k*-vector scale were weighted by k^3 and simulated employing equations derived by Dittmer and Dau [130] for analysis of the linear dichroism in the EXAFS spectra (for an extension to the XANES region, see [131]).

The absorption of X-rays by each of the four Mn atoms was considered; the backscattering atoms were O, N, C, Mn and Ca. In EXAFS analysis, typically atoms of the same type and similar distance to the X-ray absorbing atom are treated as a single 'backscatterer shell' (for backscattering of the photoelectron that is created at the X-ray absorbing atom). In our present work, each individual absorber-backscatterer (A-B) vector was treated as a distinct shell. Consequently, the number of shells was high, as four absorbing Mn ions and a high number of backscattering atoms were considered (*e.g.*, 326 A-B combinations for 84 atoms in EXAFS simulations for model C-II).

The final EXAFS spectrum, χ, is given by the sum of the contributions of *n* shells and is described by the following equation:

$$\chi(k,\theta_E) = \frac{1}{3}\sum_{i=1}^{n} N_i \left(\left(\chi_i^c(k) + 2\chi_i^s(k)\right) + \frac{1}{2}\left(\chi_i^c(k) - \chi_i^s(k)\right)\left(3(\cos\theta_E)^2 - 1\right)\left(3\left(\cos\bar{\theta}_{R,i}\right)^2 - 1\right) I_{ord} \right) \quad \text{(Eq. 1)}$$

with θ_E being the angle between the X-ray *E*-field vector and either the sample normal (*S*), for oriented membrane particles (Fig. 6A), or a specific unit cell vector (either *a* or *b* or *c*), for single-crystal EXAFS (Fig. 6B). The meaning and calculation of $\chi_i^c(k)$ and $\chi_i^s(k)$ has been described elsewhere [130] (see also equations given further below).

For partially oriented PSII samples, the angle $\bar{\theta}_{R,i}$ is the angle between the i^{th} absorber-backscatterer vector (A-B vector) and the membrane normal (*M*). In the case of polarized EXAFS on PSII crystals, spectra were collected with the *E*-field vector being exactly in parallel to the *a*-axis (or *b* or *c*), therefore θ_E equals zero. Then the value of $\bar{\theta}_{R,i}$ is the average angle between all absorber-backscatterer vectors (A-B vectors) of the i^{th} shell and the *a*-axis (or *b* or *c*, respectively). Such an averaged angle can be calculated from the individual angles of *m* absorber-backscatterer vectors $\theta_{R_j,i}$, $j = 1,\ldots,m$, of one shell according to the following equation:

$$\left(\cos\bar{\theta}_{R,t}\right)^2 = \frac{1}{m}\sum_{f=1}^{m}\left(\cos\theta_{R_f,t}\right)^2 .$$

(Eq. 2)

In the case of PSII crystals, the average angle for one unit cell consisting of four PSII dimers (see Fig. 6B) has to be taken into account. Due to the $P2_12_12_1$ symmetry of the crystal, the average angle for one shell can be calculated by averaging only the respective angles of A-B vectors in the two PSII monomers that form the PSII dimer (m = 2 in Eq. 2).

The value of the order parameter, I_{ord}, is

(i) zero for the isotopic PSII samples (*Iso*),

(ii) unity for the crystal EXAFS (*Cry*),

(iii) close 0.5 (0.47) for the partially oriented membrane particles (*Mem*), as has been determined by independent EPR measurements for the here used samples [72].

In the above paragraph, it has been described how to apply the LD-EXAFS equation (Eq. 1) to the dichroism in the EXAFS of single PSII crystals. We note that this approach is *not* generally valid for the analysis of EXAFS spectra collected on single crystals. However, it is valid in the case that the space group is of the $P2_12_12_1$ type, as encountered in the PSII crystals. The orientational averaging used for derivation of Eq. 1 [130] takes into account correctly the contributions to the EXAFS spectra resulting from the different orientations of the PSII dimers shown in Fig. 6B. However, for application of Eq. 1 to the PSII crystal EXAFS, additional averaging (by Eq. 2) is required because the Mn complexes in the two PSII monomers differ in their individual orientations with respect to the crystallographic axes.

Ab-initio calculation of EXAFS phase functions. The functions χ_i^c and χ_i^s [130] were used in the following form:

$$\chi_i^c(k) = \frac{S_0^2}{kR_i^2} e^{-2\sigma_i^2 k^2 - \frac{2R_i}{\lambda_i(k)}} f_i^c(k) \cos\left(2kR_i + \phi_i^c(k) + 2\delta_i^c(k)\right) \quad \text{(Eq. 3)}$$

$$\chi_i^s(k) = \frac{S_0^2}{kR_i^2} e^{-2\sigma_i^2 k^2 - \frac{2R_i}{\lambda_i(k)}} f_i^s(k) \sin\left(2kR_i + \phi_i^s(k) + 2\delta_i^s(k)\right). \quad \text{(Eq. 4)}$$

with R_i being the Mn-backscatterer distance, σ_i the EXAFS Debye-Waller parameter, and S_0^2 the amplitude reduction factor accounting for diverse loss processes. The program FEFF8.4 [104, 132-133] was used for *ab-initio* calculation of phase and amplitude functions (that is $\lambda_i^{c/s}$, $f_i^{c/s}$, $\phi_i^{c/s}$, $\delta_i^{c/s}$) employing a structural model that was sufficiently close to the discussed structural model. The determination functions, which are not included in standard output files of FEFF8.4, have been described elsewhere [130]. We also verified that multiple-scattering contributions to the EXAFS were small and that their neglect could not affect our conclusions.

All spectra were calculated using an S_0^2-value of 0.85 and a σ^2 value of 0.001 Å^2, for all individual A-B vectors. The EXAFS Fourier transforms were calculated for k-values ranging from 3.5 to 11.5 Å using a fractional cosine window, which spanned 10% of the above k-range at low k-values and 10% at high k-values. In the transformation from an energy to a k-vector scale, different shifts of E_0 were applied for the *Mem* and *Iso* data, on the one hand, and the *Cry* data, on the other hand, to account for the vastly different E_0 values that had been used for extraction of the EXAFS spectra (E_0=6547.0 eV for *Mem/Iso* data, E_0= 6561.3 eV for the *Cry* data).

The described method for calculation of EXAFS spectra differs from the one used by Yano *et al* [91] and Sproviero *et al* [119] but results in very similar spectra. Main advantages of the herein used approach, which is based on Eqs. 1-4, are (i) clearly smaller computational costs and (ii) the capability to treat correctly the spectra collected on partially oriented PSII membrane particles [130].

Spectra were calculated for several sets of OEC models:

Model of Yano et al (A-I, A-II, A-III, and A-IIa). The coordinates for the models I-III (and IIa) were taken from the supporting material of the respective publication [91].

Model of Sproviero et al (B-I and B-II). The DFT-QM/MM coordinates were taken from the supporting material of [119] (model B-I). (For the R-QM/MM model (B-II) of Sproviero, coordinates were used that had been personally communicated. These coordinates deviate slightly from the coordinates given in the supporting material of [119].)

Model of Dau et al (C-I) and related models (C-II, C-III, C-IV, D). The coordinates of these models were obtained as described in the following. The C-I model corresponds to the structural model presented in [92]. (The C and D models differ by the location of a five-coordinated Mn^{III} ion. In the C models, Mn^1 is five-coordinated; in the D model, Mn^3 is five-coordinated.)

3.3. Optimization of structural models

A series of models was obtained by variation of the OEC structure we had proposed earlier, namely the model shown in Fig. 3. Therefore, we used the coordinates of the crystallographic model of Loll *et al* [39] as a starting point for molecular mechanics simulations (MM+ force field of Hyperchem 7, Hypercube Inc.). These coordinates are mostly close to the ones recently determined by Shen and coworkers [44] (see Introduction section).

Step 1—Molecular mechanics modeling with restraints. In this step the crystallographic model of the protein environment of Loll *et al* [39] was refined to accommodate the respective OEC core of C-II, C-III, C-IV, and D (for model C-I, see [92] and comment further below). Strong harmonic restraints were introduced for all the Mn-Mn distances (with exception of the long Mn^2-Mn^4 distance), for the Mn-ligand distances of the first coordination sphere (Mn-O/N) and for selected bond angles of the Mn atoms. The Mn-Mn and Mn-Ca distances were chosen for good agreement with the isotropic spectrum (see 2.1—*Iso*), mostly based on the EXAFS simulation of [92]. The Mn-O/N bond lengths and bond angles were restrained to chemically reasonable values. After implementation of the appropriate restraints, a geometry optimization (steepest descent algorithm of Hyperchem) was carried out involving all atoms in a sphere of about 5.5 Å around Mn^1, Mn^2, and Mn^3 and of 6.5 Å around Mn^4. The sphere around Mn^4 was chosen larger because in this region the published crystallographic models differ significantly and the influence of prolonged X-ray exposure during data collection is especially strong [39]. All atoms outside of the four spheres remained at fixed positions. The described procedure corresponds to the protocol previously used to obtain the model shown in Fig. 3.

Step 2—Refined models by EXAFS simulations. This step aims mostly at the optimization of the Mn-Mn and Mn-Ca distances of the model. A refined model was obtained by maximizing the agreement between seven calculated and seven experimental EXAFS spectra. The three types of EXAFS data described above were used, namely the isotropic extended-range spectrum (2.1-*Iso*), the polarized EXAFS collected on PSII membrane particles (2.1-*Mem*), and the polarized EXAFS collected on PSII crystals (2.1-*Cry*). For calculation of these

spectra, all non-hydrogen atoms with a maximal distance of 6.5 Å to the Mn atoms were taken into account (typically around 80 atoms). For optimizing the structural model, an error sum was calculated for each individual spectrum by summing up the squared differences between experimental and simulated spectra. In the case of the *Iso* and *Mem* data, the error sum was calculated for the *k*-space data, *i.e.* without involving the calculation of a Fourier transform (FT). In the case of crystal spectra (*Cry*), the FTs were calculated for the simulated EXAFS spectra and compared to the experimental FT-amplitude spectra of [91]. For this comparison, the region between 1.1 and 3.2 Å of reduced distance was used.

A joint error sum was calculated by a weighted addition of the seven error sums of the seven spectra. This joint error sum was minimized using a Levenberg-Marquardt (LM) algorithm for variation of the atomic coordinates. Restraints were used as outlined in the following. The position of all atoms with a distance exceeding 5 Å to their nearest Mn atom was held constant resulting in around 50 moveable atoms. To keep the structure of the simulated Mn complex chemically reasonable, weak restraints were used for the length of internal Mn-O bonds. Stronger restraints were applied to the single 2.45 Å Mn-O distance (either Mn^1-O^a or Mn^1-O^d) of the Mn complex (preserving the overall idea of the current model) and short C-C, C-O, C-N distances to prevent changes in the (internal) geometry of the protein ligands. No restraints were used for the Mn-Mn and Mn-Ca distances or for the terminal oxygen ligands.

Step 3—Corrections in the molecular mechanics framework. In this step the geometry of the ligating amino acids and internal oxygen atoms was corrected. Some unreasonable positions of light atoms resulted from Step 2. Therefore in a second round of geometry optimization, these chemically unreasonable aspects of the structural model were removed. Geometry optimization was applied locally to critical ligating amino acids, to remove specifically chemically unreasonable geometries. Only in cases of obviously misplaced internal bridging oxygens, a geometry optimization was applied also to these atoms.

Step 4—Second refinement of the model. Moving of the light backscatterers in Step 3 necessarily affected the EXAFS spectra. Especially, the first peak often differed markedly from the original fit results of Step 2. To correct for this, a similar refinement as in Step 2 was applied. The main difference in comparison to the procedure of Step 2 was a strongly weighted additional contribution to the error sum, which was obtained by summation of the squared differences between the starting and current position of the atoms. As a result, all atoms moved only slightly (typically by about 0.07 Å) and therefore the outcome of the previous steps was mostly preserved. In the case of misplaced internal oxygen atoms (unrealistic Mn-O distances), a new geometry optimization was performed for the misplaced atoms (Step 3) before repeating the Step 4 procedure.

The C-I model has been presented previously [92]. The procedure in Dau *et al* [92] had involved a clearly less comprehensive comparison to experimental results than herein used for development of C-II, C-III, C-IV, and D. Specifically the polarized EXAFS data (*cry* and *mem*) had not been used in development of the C-I model.

4 Evaluation of alternative OEC models

First, we will evaluate recently proposed models of the Mn_4Ca complex and its ligand environment, which are discussed in section 2. As an indicator for the quality of the models serves the agreement between calculated and experimental spectra for the isotropic EXAFS collected over an extended energy range (Fig. 7, *Iso* data, one spectrum) and the EXAFS dichroism data collected on uni-directionally oriented PSII membrane particles (Fig. 8, *Mem* data, four spectra) as well as on single crystals of PSII (Fig. 9, *Cry* data, three spectra). A

detailed description of the used methodical approach is presented above in section 3.

To judge the validity of alternative models, the second peak of the EXAFS FTs is especially informative. It relates to Mn-Mn distances around 2.7 Å resulting from di-μ-oxo bridged pairs of Mn ions. The second FT peak (or the corresponding EXAFS oscillations) (i) represents a dominating and characteristic feature of the OEC spectra and (ii) is well above the noise level (as opposed, e.g., to the third FT peak in the *cry* data). In Fig. 10, the magnitudes of the second FT peaks are compared in form of a bar diagram. Already the qualitative comparison of these bar diagrams disfavor several of the investigated OEC models. A more detailed comparison is facilitated by Table 2, in which crucial structural parameters are given, namely all metal-metal distances and angles of the respective vector with the membrane normal. The error sum in the last row of Table 2 accounts for *all* deviations between experimental and calculated spectra (weighted sum of error sums of *iso, mem, cry* data; complete *k*-range).

Yano *et al* [91] have proposed a series of mutually related models (A-I, A-II, A-III, and A-IIa in Fig. 4), for which the calculated EXAFS spectra match the polarized EXAFS data obtained for PSII crystals (*Cry* data). In Fig. 10, results are shown for model A-IIa; the corresponding bar diagrams of the other three OEC models of Yano *et al* are shown in Fig. S6. The four OEC models of Yano *et al* have been constructed to match the polarized EXAFS spectra of PSII crystal (*Cry* data). As anticipated, also in our calculations the agreement between calculated and experimental spectra is good. However, all four models are qualitatively in stark conflict with the polarized EXAFS of PSII membrane particles (*Mem* data). For all four models holds that the dichroism predicted for PSII membrane particles is inverted with respect to the experimental findings (minimal peak amplitude at 15° in the experimental spectra but maximal in the simulated spectra). Because of this clear discrepancy and assuming that structure and orientation of the OEC are identical in the cyanobacterial (*Cry* data) and plant PSII (*Mem* data), we can rule out the models proposed by Yano *et al.*

Starting with a variant of the crystallographic model of Barber and coworkers [38], Sproviero *et al* [119] obtained an OEC model by DFT-QM/MM calculations (B-I, similar to Fig. 2). Subsequently they refined their DFT model by optimizing the agreement with the polarized EXAFS collected on PSII crystals (*Cry* data), a procedure that resulted in model B-II (shown in Fig. 2). As shown in Fig. 10, the B-II model is in reasonably good agreement with both the *Cry* data and the *Mem* data sets.

In Dau *et al* [92], the OEC model shown in Fig. 3 has been proposed, which has been based mostly (i) on the extended-range EXAFS data (*Iso* data) and (ii) on the crystallographic model of the protein ligands of Loll *et al* [39] (and was obtained by molecular mechanics modeling as described in section 3). This model corresponds to C-I. The coordinates of the originally proposed model were optimized for agreement with the isotropic, extended-range EXAFS data (*iso* data), but not for agreement with the polarized EXAFS data. As visible in Fig. 10, the C-I model is in clear conflict with both the *Cry* and the *Mem* data. Table 2 reveals the origin of the disagreement with the *Mem* data. In C-I, the Mn^3-Mn^4 vector (~2.7 Å) forms an angle with the membrane normal that is clearly smaller than the magic angle of 54.7°. Therefore the predicted dichroism is qualitatively in disagreement with the experimental findings. As opposed to the C-I model, the C-II model was obtained by the optimization procedure described in section 3 employing also the polarized EXAFS data sets, which results in an increase of the Mn^3-Mn^4 angle by 10°. This increase facilitates agreement with the *Mem* data and also relates to the improved agreement with the *Cry* data.

In 2001, we proposed that in the $S_2 \rightarrow S_3$ transition a five-coordinated Mn(III) is transformed into a six-coordinated Mn(IV) [34]. Later we could support this suggestion on the basis of an improved understanding of the changes in the XANES spectra in the $S_2 \rightarrow S_3$ transition [48,

64, 78]. (The XANES analyses suggested that there could be a sixth ligand to the five-cordinated Mn(III) that is at a distance exceeding 2.4 Å. In the following we consider any Mn ion with one ligand at a distance greater than 2.4 Å as being five-coordinated.) Already the dangler model (Fig. 1B) had involved a five-coordinated Mn(III) ion. Also recent computational studies point toward the presence of five-coordinated Mn(III) in the OEC, namely analyses of EPR parameter (by Lubitz, Messinger, Neese and their coworkers [25] and by Kaupp and coworkers [134]) and the computational work of Siegbahn on the mechanism of water oxidation [121-122]. We note that the question whether in the $S_2 \rightarrow S_3$ transition any manganese is oxidized (manganese-centered oxidation of the OEC) is still disputed (in X-ray spectroscopy, [34, 48, 78, 120, 124, 135] *versus* [136-138]) and additional experimental evidence is needed for clarification. For the time being, we assume that the presence of one five-coordinated Mn(III) in the OEC in its dark-stable S_1-state is sufficiently backed up by experimental and theoretical work to use this assumption in construction of OEC models. Therefore not only the models C-I and C-II, but also all the OEC models that are discussed in the following (C-III, C-IV, and D) involve the presence of a five-coordinated Mn(III) ion.

The C-III model differs from C-I and C-II in two relevant points:

(1) In C-III, the Mn^1 ion also is five-coordinated (Mn-O distance > 2.4 Å), but the open coordination site is assumed to be in *trans*-position to O-Asp342 (whereas in C-I and C-II it is in *trans*-position to N-His332), as has been proposed by Siegbahn on the basis of DFT calculations [121-122].

(2) In C-III, the Mn^3-Mn^4 distance is 3.0 Å (versus ~2.7 Å in C-I and C-II). Chemically, this relatively long Mn^3-Mn^4 distance might result from protonation of O^e or O^d.

Model C-IV represents a variant of C-III involving a longer Mn^1-Mn^4 distance (4.3 versus 3.7 Å in C-I, C-II, and C-III). Thereby, it is achieved that in C-IV, the 'baseplate atoms' (Mn^1, O^d, Mn^4, O^a, Mn^3, O^b) lie roughly within the same plane, as is the case for model C-I and C-II, but as opposed to C-III. Moreover, OEC model C-IV requires especially small variations of the coordinates of the protein atoms of Loll *et al* [39] (see overlay plot of the Loll structure and the herein discussed models shown in Figs. S8-S17).

There are also other closely related OEC models that are in reasonably good agreement with the EXAFS data sets. In model D, Mn^3 is assumed to be a five-coordinated Mn(III) ion (Fig. 11D; see Table S1 for more details). This assumption is not supported by DFT calculations [121-122, 134] but still might represent an option.

We considered also additional variants of OEC models, which are not presented herein. When scrutinizing these model variants we found that for specific positions of the light ligand atoms in the second and third coordination shell, also variants of model C-III and C-IV with a third short Mn-Mn vector (Mn^3—Mn^4 distance also below 2.9 Å) are in reasonable agreement with the EXAFS data and thus can not be excluded rigorously.

In conclusion, the A-class of models is difficult to reconcile with the crystallographic data and is in clear conflict with the polarized EXAFS of partially oriented PSII particles. In the B-class, the refined model of Sproviero *et al* [119] may be in reasonable agreement with the EXAFS results but is in clear conflict with the crystallographic models obtained by the Zouni group [39] and very recently by Shen's group [44]. The C-class of models (as well as model D) relates to an overall topology suggested by Dau *et al* [13, 92], Siegbahn [121-122], and Umena *et al* [44]. These closely related OEC models are in good agreement with the three types of EXAFS data (*Iso, Cry,* and *Mem* data) and thus may serve as a starting point for further investigations.

In the light-driven assembly of the Mn complex (photoactivation) [139-140], most likely a di-μ-oxo bridged manganese dimer is formed within the protein cavity that later harbors the intact Mn complex [141-143]. Presently however, the OEC models of the C-class do not provide any clear indications where this assembly intermediate is formed.

It is reassuring that the EXAFS-based approach of Dau *et al* (see [13, 92] and analysis described above) and the DFT-based approach of Siegbahn [121-122] (both in conjunction with the crystallographic model of Loll *et al* on the protein environment of the OEC [39]) result in very similar OEC models that are largely in line with the high-resolution crystallographic model of Shen and coworkers [44]. This mutual consistency suggests that the basic geometry of Shen's crystallographic model does not result from severe modifications by X-ray exposure, even though the specific coordinates may relate to a Mn complex in the S_{-3} state, that is, after X-ray photoreduction by about four electrons. We note that this mutual consistency does not necessarily include Asp170. A relatively strained and twisted geometry of Asp170 (see Fig. 13) is implied by the ligation scheme of the crystallographic model of Shen and his coworkers, a point that requires further scrutiny.

In the following, we assume that the OEC structure is described by one of the models of the C or D class discussed above and thus is close to the OEC models of Dau, Siegbahn, Shen and their respective coworkers (Fig. 3 and 5).

5. Mechanistic implications

5.1 Mode of O-O bond formation

Visualization of molecular structures satisfies the human want to understand by seeing. Now, we will go beyond visualization of the static OEC structure and discuss the implications of the recently gained structural information for the mechanism of photosynthetic water oxidation, without addressing all relevant mechanistic questions in detail. For review articles addressing the mechanism of PSII water oxidation, see [12-13]; for an overview on conceivable alternative routes toward water oxidation and O-O bond formation in PSII as well as in synthetic catalysts, see [89].

The OEC structure strongly suggests a special role for Mn^4. At least in the S_1 state of OEC, terminally coordinated water molecules are only found as ligands of Mn^4 (two H_2O or OH^-, see Fig. 3 or 5). This structural feature excludes that two water molecules coordinated to two different Mn ions are successively deprotonated until the O-O is formed between the two terminally coordinated oxides or oxyl radicals (Fig. 12A), as had been proposed (*e.g.*) by Babcock and coworkers [80-82, 144].

The O-O bond formation (Fig. 12B) between the oxygens of the two water molecules at Mn^4 (Figs. 3, 5, 13)) represents an option that recently has not been part of any prominent working hypotheses on the mechanism of photosynthetic water oxidation. Wyrdrzynski, Messinger, Hillier [145-151] and their coworkers have shown that there are two binding sites for the two substrate water molecules that are distinct and 'immiscible' meaning that the two substrate water can exchange their positions within the OEC only slowly (or not at all). Only if the two water-oxygens coordinated to Mn^4 were immiscible, the route of O-O bond shown in Fig. 12B would be in agreement with the water-exchange data. On a first glance, very fast mutual exchange of OW1 and OW2 (in Fig. 13) appears to be likely. However, a rapid exchange might be prevented by stabilizing hydrogen bonds implied by the crystallographic model of Shen and his coworkers (see Fig. 5A). Experimental or theoretical investigations addressing this point are still lacking.

The O-O bond formation between two bridging oxygens (Fig. 12C) has been proposed in the past, but is disfavored by the OEC structure which likely renders the respective μ-O pair too inert for bond formation. Most bridging oxygens are stabilized by their coordination bonds to three metal ions (μ_3-O). Only O^e clearly bridges between to Mn ions only (Mn^3—(μ_2-O^e)—Mn^4) but likely is stabilized by hydrogen bonding to Arg357. Additional stabilization by H-bond interactions are likely (O^b···His337(D1), O^c···Arg357(CP43), and others).

Also experimental findings on the exchange rate of the (substrate) water molecules disfavor O-O bond formation between bridging oxygens. Results obtained on synthetic Mn complexes suggest that the exchange of bridging oxygen generally is too slow [152-153] to account for the exchange rates observed for the substrate water in PSII [145-151].

In the oxygen-evolution transition ($S_3 \rightarrow S_0 + O_2$), one of the water species at Mn^4 may be present in from of an oxyl radical. Then O-O bond formation could involve the nucleophilic attack of a water or hydroxide that either is positioned by coordination to the Ca ion or stems from outer-sphere water (Fig. 12D-F). This nucleophilic-attack mechanism of O-O bond formation has been proposed frequently (see [12] and references therein), *inter alia*, by Barber and his coworkers on the basis of their crystallographic OEC model [38, 154-155] (Fig. 2). In 2001, Dau and coworkers proposed that the O-O bond involves a nucleophilic attack of an outer-sphere water and is facilitated by the coupling of Mn reduction to movement of one or more protons, specifically by the transfer of a proton from an outer-sphere substrate water to a bridging oxygen (Fig. 12E) [34]. Starting from the crystallographic model of Barber, a mechanism involving the nucleophilic attack by a Ca-bound water has been worked out in detail by means of quantum chemical studies by the researchers in Yale around Brudvig, Batista and Sproviero [12, 114-115, 118, 156] (Fig. 12F). A specific achievement of the researchers in Yale had been that they considered in detail the mechanistic role of protons in water oxidation and suggested that the Arg357 (of the CP43 protein) plays a crucial role in facilitating proton movements and serves as a catalytic base. Moreover, their mechanistic model also involved the transfer of a proton to a bridging oxide, as schematically shown in Fig. 12F.

The Yale researchers based their mechanistic models on the crystallographic model of Barber and coworkers [38] that is conflict with the more recent crystallographic models obtained by Zouni [39, 42], Shen [44] and their respective coworkers. Nonetheless, the modeling approach of the Yale researchers has highlighted that intricate protonation dynamics likely are crucial for the function of the OEC. In the recent crystallographic model of Shen and coworkers [44], Glu189 is not a Ca ligand but replaced by a second water molecule coordinated to the Ca ion (O^{W3} in Fig. 13). Taking into account this modification in the ligand scheme, a nucleophilic attack of a Ca-bound water molecule (O^{W3}) toward an oxyl group at Mn^4 (O^{W2}) becomes a possibility.

By DFT calculations, Siegbahn has derived a model for the OEC structure and its chemistry that predicts an S_1-state structure of the OEC similar to C-III and C-IV [121-122]. In the $S_2 \rightarrow S_3$ transition of the water oxidation cycle, a hydroxide binds at the open coordination site of Mn^1 and becomes a bridging ligand between Mn^1 and the Ca ion. This bound hydroxide is deprotonated and oxidized in the $S_3 \rightarrow S_4$ transition resulting in the formation of an oxygen radical. Subsequently, the O-O bond is formed between this oxygen radical and O^d, which is bridging between Mn^3, Mn^4, and the Ca ion (μ_{2Mn+Ca}-O^d), as shown in Fig. 12G. Siegbahn's DFT-based model predicts both a mechanism of water oxidation as well as OEC structures for all S-states. Presently, this is the only detailed DFT-based mechanistic model that (most likely) is in good agreement with the recent crystallographic and the currently available EXAFS data on the S_1-state of the OEC (model C-III and C-IV). (We note that the mechanism

of Siegbahn (Fig. 12G) is in conflict with the argument we used above, namely that an oxygen atom in bridging position between two Mn and one Ca ion is highly stabilized and thus too inert for participating in the O-O bond formation step. Siegbahn's calculations appear to disprove this argument, at least for the intricate mode of O-O bond formation proposed in [121-122].)

In conclusion, the now available information on the OEC structure rules out several modes of O-O bond formation as discussed above. Besides the specific mode of O-O bond formation proposed by Siegbahn, especially the nucleophilic attack toward a water species (likely an oxyl radical) bound to Mn^4 remains an attractive and viable option. The attacking substrate water could be either an outer-sphere water species or a hydroxide coordinated by the Ca ion. The putative substrate water molecules bound to Mn^4 (O^{W1}, O^{W2} in Fig. 13), two water molecules bound to Ca (O^{W2}, O^{W3} in Fig. 13), two or more outer-sphere water molecules, and the Tyr161-His190 moiety form a hydrogen-bonding network (see Fig. 5B). We feel that this arrangement could facilitate O-O bond formation mechanisms that have not been worked out by means of quantum chemical calculations yet. In a Grotthus-type mode, proton relocations over several Ångströms could be coupled to the Mn reduction in the O-O bond formation step, along the lines suggested elsewhere [89]. The OEC indeed may be 'wired for protons' [83].

5.2 Future challenges and perspectives

The above discussion of specific O-O bond formation steps should not obscure that the earlier steps in the reaction cycle of water oxidation are decisive for energetically efficient and kinetically competent water oxidation [13, 157-158]. In the following, this is highlighted by considering photosynthetic water oxidation and the classical process of electrochemical water oxidation in a similar conceptual framework (for details and references, see [89]).

It is commonly assumed that water oxidation generally involves four separate one-electron oxidation steps. In each oxidation step, either the catalytic site (manganese oxidation in PSII) or the water substrate itself is partially oxidized (early peroxide or $O^{\bullet}$ formation). In PSII, the oxidant is the Tyr_Z; in an electrochemical system it is a conducting electrode. In both systems, the potential of the oxidant is roughly the same for each one-electron oxidation step. In PSII, the relevant potential is the E_m of the $Tyr_Z^{\bullet}/Tyr_Z$ couple of about +1.2 V [158-162] (about the same in each S-state transition). In electrochemical water oxidation, it is the (fixed) electrical potential at the anode. In both systems, the crucial mechanistic problem lies in balancing the free energy losses in the four one-electron oxidation steps and the associated deprotonation reactions, *inter alia*, because the free-energy loss in one of the four steps cannot be regained in another one-electron step. In electrochemical water oxidation, the step associated with the largest potential requirement determines the overpotential needed to oxidize water (overpotential-determining step) and thus the energetic efficiency of the electrochemical process. In PSII, the overpotential is fixed at a comparatively low level (around 0.3 V at pH 5) and evolution had to tune the energetics of the individual steps of the reaction cycle accordingly. Moreover and as opposed to electrochemical systems, in PSII the reactions in water oxidation need to be so fast that they outcompete efficiently the charge recombination reactions [158, 163]. In conclusion, unraveling the secret of the still unsurpassed performance of water oxidation at the donor side of PSII will require an in-depth understanding of the individual steps in PSII water oxidation that occur before onset of O-O bond formation.

In PSII research, the processes in light-driven water oxidation at the donor side of PSII are discussed in the framework of the classical S-state cycle model proposed already in 1971 by Kok and coworkers [164-165]. Today it is known that the accumulations of four positive

charges proposed by Kok corresponds to four successive one-electron oxidations of the Mn complex, as schematically shown in Fig. 14. The S-state cycle model has been extended to include also the proton removal from the Mn complex [90, 102] (Fig. 15), as reviewed elsewhere [13]. Based on the now available structural information on the OEC and the PSII proteins in general, each step in the framework model of Fig. 15 needs to be addressed at the atomic level, aiming at a complete understanding of energetics (see also [158]) and kinetics of the reactions.

Siegbahn recently has developed an atomistic model of the OEC function and calculated structures and free-energy differences for each of the transitions indicated in Fig. 15 [121-122], an exceptional achievement. However, it is a still open question whether Siegbahn's most recent model is in agreement with (all) the information obtained in experimental studies. Moreover, the touchstones that have been provided by experimentalists for evaluation of computational models are insufficient. The free-energy differences for the steps in the reaction cycle of Fig. 15 are often unknown. In this respect, an important step forward was made recently by deriving estimates of four pK values experimentally (and thus of the ΔG values for deprotonation), for each of the four protons removed from the OEC in the course of the reaction cycle [166], in an extension of earlier investigations [167-168].

Also the information on the chemical and structural changes accompanying these steps is limited and rarely unambiguous [34, 65, 78, 169-170]. Addressing these points represents an enormous challenge to experimentalists. New methods may complement the arsenal of established experimental approaches. To provide the flavor of one of the new experimental avenues toward the electronic structure of the OEC, we conclude this article with Figure 16.

The electronic structure of the OEC, specifically the localization of the accumulated oxidation states, is of high interest. Pertinent questions as the one, which Mn ion is oxidized in a specific S-state transition, or whether ligand oxidation occurs cannot be addressed merely on the basis of crystallographic data. Experimental access can come from spectroscopic investigations involving advanced EPR methods, vibrational spectroscopy (FTIR), and X-ray spectroscopy, always in conjunction with computational approaches. Bergmann, Glatzel and their coworkers have developed the methodology for highly resolved detection of X-ray emission spectra and approached application of these new techniques to the OEC in cooperation with the group in Berkeley (detection of K_β emission, resonant inelastic X-ray scattering, K_β satellite lines) [126, 136, 171-175]. We approached a combination of emission-resolved X-ray spectroscopy with the linear dichroism approach (polarized X-ray spectroscopy) resulting in the data shown in Fig. 16. In polarized XAS studies on partially oriented PSII membrane particles, it has been found that the pre-edge feature, which is assignable to transition of the *1s* electron to partially occupied *3d* orbitals of manganese, is dichroic (that is, it depends on the excitation angle; θ_E in Fig. 6A) as illustrated by the lower inset of Fig. 16. Additionally we now find clear differences in the pre-edge feature (Fig. 16, upper inset) and in the edge-rise for detection at three distinct emission energies in the region of the Mn-K_α line. By a combination with appropriate theoretical and computational approaches, detailed new insights in the coordination geometry and electronic structure of the individual Mn ions may come from this and other novel methods.

Acknowledgement. Financial support by the Berlin cluster of excellence on Unifying Concepts in Catalysis (UniCat), the European Union (7th framework program, support to the *SOLAR-H2* consortium), and the German 'Bundesministerium für Bildung und Forschung' (BMBF, support to the *H_2 design cell* consortium) is gratefully acknowledged. X-ray absorption and emission data has been collected at the XAFS beamline of the EMBL

outstation at the DORIS ring of the DESY in Hamburg (supported by Dr. W. Mayer-Klaucke) and at the beamline ID26 of the ESRF (European Synchrotron Radiation Facility in Grenoble, supported by Drs. P. Glatzel and T.-C. Weng). We thank Drs. I. Zaharieva, M. Haumann, P. Chernev and Mr. M. Risch (Freie Universität Berlin) for collecting the high-resolution X-ray emission data at the ESRF and for stimulating discussions.

References

[1] D. Gust, T.A. Moore, Mimicking photosynthesis, Science 244 (1989) 35-41.

[2] L.C. Sun, M.K. Raymond, A. Magnuson, D. LeGourrierec, M. Tamm, M. Abrahamsson, P.H. Kenez, J. Martensson, G. Stenhagen, L. Hammarstrom, S. Styring, B. Akermark, Towards an artificial model for photosystem II: a manganese(II,II) dimer covalently linked to ruthenium(II) tris-bipyridine via a tyrosine derivative, J. Inorg. Biochem. 78 (2000) 15-22.

[3] N.S. Lewis, D.G. Nocera, Powering the planet: chemical challenges in solar energy utilization, Proc. Natl. Acad. Sci. USA 103 (2006) 15729-15735.

[4] L. Hammarstroem, S. Hammes-Schiffer, Special issue on artificial photosynthesis and solar fuels, Acc. Chem. Res. 42 (2009) 1859-2029.

[5] C. Herrero, B. Lassalle-Kaiser, W. Leibl, A.W. Rutherford, A. Aukauloo, Artificial systems related to light driven electron transfer processes in PSII, Coord. Chem. Rev. 252 (2008) 456-468.

[6] A.W. Rutherford, T.A. Moore, Mimicking photosynthesis, but just the best bits, Nature 453 (2008) 449.

[7] W. Lubitz, E.J. Reijerse, J. Messinger, Solar water-splitting into H_2 and O_2: design principles of photosystem II and hydrogenases, Energy Environ. Sci. 1 (2008) 15-31.

[8] D. Ort, C.F. Yocum, Oxygenic Photosynthesis: The Light Reactions, Kluwer Academic Publ., Dordrecht, 1996.

[9] R.E. Blankenship, Molecular Mechanisms of Photosynthesis, Blackwell Science, Oxford, England, 2002.

[10] V.K. Yachandra, K. Sauer, M.P. Klein, Manganese cluster in photosynthesis: where plants oxidize water to dioxygen, Chem. Rev. 96 (1996) 2927-2950.

[11] R.J. Debus, The manganese and calcium ions of photosynthetic oxygen evolution, Biochim. Biophys. Acta 1102 (1992) 269-352.

[12] J.P. McEvoy, G.W. Brudvig, Water-splitting chemistry of photosystem II, Chem. Rev. 106 (2006) 4455-4483.

[13] H. Dau, M. Haumann, The manganese complex of photosystem II in its reaction cycle—basic framework and possible realization at the atomic level, Coord. Chem. Rev. 252 (2008) 273-295.

[14] G.C. Dismukes, Y. Siderer, Intermediates of a polynuclear manganese center involved in photosynthetic oxidation of water, Proc. Natl. Acad. Sci. USA 78 (1981) 274-278.

[15] A.F. Miller, G.W. Brudvig, A guide to electron paramagnetic resonance spectroscopy of photosystem II membranes, Biochim. Biophys. Acta 1056 (1991) 1-18.

[16] R.J. Pace, P. Smith, R. Bramley, D. Stehlik, EPR saturation and temperature dependence studies on signals from the oxygen-evolving center of photosystem II, Biochim. Biophys. Acta 1058 (1991) 161-170.

[17] R.G. Evelo, S. Styring, A.W. Rutherford, A.J. Hoff, EPR relaxation measurements of photosystem II reaction centers: influence of S-state oxidation and temperature, Biochim. Biophys. Acta 973 (1989) 428-442.

[18] K. Hasegawa, T. Ono, Y. Inoue, M. Kusunoki, Spin-exchange interactions in the S_2-state manganese tetramer in photosynthetic oxygen-evolving complex deduced from g=2 multiline EPR signal, Chem. Phys. Lett. 300 (1999) 9-19.

[19] N. Ioannidis, J.H.A. Nugent, V. Petrouleas, Intermediates of the S_3 state of the oxygen-evolving complex of photosystem II, Biochemistry 41 (2002) 9589-9600.

[20] R.D. Britt, K.A. Campbell, J.M. Peloquin, M.L. Gilchrist, C.P. Aznar, M.M. Dicus, J. Robblee, J. Messinger, Recent pulsed EPR studies of the photosystem II oxygen-evolving complex: implications as to water oxidation mechanisms, Biochim. Biophys. Acta 1655 (2004) 158-171.

[21] L.V. Kulik, B. Epel, W. Lubitz, J. Messinger, ^{55}Mn pulse ENDOR at 34 GHz of the S_0 and S_2 states of the oxygen-evolving complex in photosystem II, J. Am. Chem. Soc. 127 (2005) 2392-2393.

[22] A. Haddy, EPR spectroscopy of the manganese cluster of photosystem II, Photosynth. Res. 92 (2007) 357-368.

[23] K. Olesen, L.E. Andreasson, The function of the chloride ion in photosynthetic oxygen evolution, Biochemistry 42 (2003) 2025-2035.

[24] C. Teutloff, S. Pudollek, S. Kessen, M. Broser, A. Zouni, R. Bittl, Electronic structure of the tyrosine D radical and the water-splitting complex from pulsed ENDOR spectroscopy on photosystem II single crystals, Phys Chem Chem Phys 11 (2009) 6715-6726.

[25] D.A. Pantazis, M. Orio, T. Petrenko, S. Zein, W. Lubitz, J. Messinger, F. Neese, Structure of the oxygen-evolving complex of photosystem II: information on the S_2 state through quantum chemical calculation of its magnetic properties, Phys. Chem. Chem. Phys. 11 (2009) 6788-6798.

[26] T. Noguchi, Fourier transform infrared analysis of the photosynthetic oxygen-evolving center, Coord. Chem. Rev. 252 (2008) 336-346.

[27] R.J. Debus, Protein Ligation of the Photosynthetic Oxygen-Evolving Center, Coord. Chem. Rev. 252 (2008) 244-258.

[28] T. Yamanari, Y. Kimura, N. Mizusawa, A. Ishii, T.-A. Ono, Mid- to low-frequency fourier transform infrared spectra of S-state cycle for photosynthetic water oxidation in *synechocystis* sp. PCC 6803, Biochemistry 43 (2004) 7479-7490.

[29] W. Hillier, G.T. Babcock, S-state dependent fourier transform infrared difference spectra for the photosystem II oxygen evolving complex, Biochemistry 40 (2001) 1503-1509.

[30] V.K. Yachandra, R.D. Guiles, A. McDermott, R.D. Britt, S.L. Dexheimer, K. Sauer, M.P. Klein, The state of manganese in the photosynthetic apparatus. 4. Structure of the manganese complex in photosystem II studied using EAFS spectroscopy. The S_1 state of the O_2-evolving photosystem II complex from spinach, Biochim. Biophys. Acta 850 (1986) 324-332.

[31] D.J. MacLachlan, B.J. Hallahan, S.V. Ruffle, J.H. Nugent, M.C. Evans, R.W. Strange, S.S. Hasnain, An e.x.a.f.s. study of the manganese O_2-evolving complex in purified Photosystem II membrane fractions. The S_1 and S_2 states, Biochem. J. 285 (1992) 569-576.

[32] V.K. Yachandra, V.J. DeRose, M.J. Latimer, I. Mukerji, K. Sauer, M.P. Klein, Where plants make oxygen: a structural model for the photosynthetic oxygen-evolving manganese cluster, Science 260 (1993) 675-679.

[33] J.E. Penner-Hahn, Structural characterization of the Mn site in the photosynthetic oxygen-evolving complex, in: H.A.O. Hill, P.J. Sadler, A.J. Thomson (Eds.), Metal Sites in Proteins and Models: Redox Centres, vol. 90, Springer, Berlin / Heidelberg, Germany, 1998, pp. 1-36.

[34] H. Dau, L. Iuzzolino, J. Dittmer, The tetra-manganese complex of photosystem II during its redox cycle: X-ray absorption results and mechanistic implications, Biochim. Biophys. Acta 1503 (2001) 24-39.

[35] K. Sauer, J. Yano, V.K. Yachandra, X-ray spectroscopy of the photosynthetic oxygen-evolving complex, Coord. Chem. Rev. 252 (2008) 318-335.

[36] A. Zouni, H.T. Witt, J. Kern, P. Fromme, N. Krauss, W. Saenger, P. Orth, Crystal structure of photosystem II from *Synechococcus elongatus* at 3.8 Å resolution, Nature 409 (2001) 739-743.

[37] N. Kamiya, J.-R. Shen, Crystal structure of oxygen-evolving photosystem II from *Thermosynechococcus vulcanus* at 3.7-Å resolution, Proc. Natl. Acad. Sci. USA 100 (2003) 98-103.

[38] K.N. Ferreira, T.M. Iverson, K. Maghlaoui, J. Barber, S. Iwata, Architecture of the photosynthetic oxygen-evolving center, Science 303 (2004) 1831-1838.

[39] B. Loll, J. Kern, W. Saenger, A. Zouni, J. Biesiadka, Towards complete cofactor arrangement in the 3.0 A resolution structure of photosystem II, Nature 438 (2005) 1040-1044.

[40] J.W. Murray, K. Maghlaoui, J. Kargul, N. Ishida, T.-L. Lai, A.W. Rutherford, M. Sugiura, A. Boussac, J. Barber, X-ray crystallography identifies two chloride binding sites in the oxygen evolving centre of photosystem II, Energy Environ. Sci. 1 (2008) 161-166.

[41] K. Kawakami, Y. Umena, N. Kamiya, J.R. Shen, Location of chloride and its possible functions in oxygen-evolving photosystem II revealed by X-ray crystallography, Proc. Natl. Acad. Sci. USA 106 (2009) 8567-8572.

[42] A. Guskov, J. Kern, A. Gabdulkhakov, M. Broser, A. Zouni, W. Saenger, Cyanobacterial photosystem II at 2.9-Å resolution and the role of quinones, lipids, channels and chloride, Nat. Struct. Mol. Biol. 16 (2009) 334-342.

[43] M. Broser, C. Glöckner, A. Gabdulkhakov, A. Guskov, J. Buchta, J. Kern, F. Müh, H. Dau, W. Saenger, A. Zouni, Structural basis of cyanobacterial photosystem II inhibition by the herbicide terbutryn, J. Biol. Chem. 286 (2011) 15964-15972.

[44] Y. Umena, K. Kawakami, J.-R. Shen, N. Kamiya, Crystal structure of oxygen-evolving photosystem II at a resolution of 1.9 Å, Nature 473 (2011) 55-60.

[45] B. Teo, EXAFS: Basic Principles and Data Analysis, Springer Verlag, Berlin, Germany, 1986.

[46] G.N. George, B. Hedman, K.O. Hodgson, An edge with XAS, Nat. Struct. Biol. 5 (1998) 645-647.

[47] H. Dau, P. Liebisch, M. Haumann, The structure of the manganese complex of photosystem II in its dark-stable S_1-state: EXAFS results in relation to recent crystallographic data, Phys. Chem. Chem. Phys. 6 (2004) 4781-4792.

[48] H. Dau, P. Liebisch, M. Haumann, X-ray absorption spectroscopy to analyze nuclear geometry and electronic structure of biological metal centers—potential and questions examined with special focus on the tetra-nuclear manganese complex of oxygenic photosynthesis, Anal. Bioanal. Chem. 376 (2003) 562-583.

[49] H. Dau, M. Haumann, X-ray absorption spectroscopy to watch catalysis by metalloenzymes: status and perspectives discussed for the water-splitting manganese complex of photosynthesis, J. Synchrotron Rad. 10 (2003) 76-85.

[50] C.F. Yocum, V.L. Pecoraro, Recent advances in the understanding of the biological chemistry of manganese, Curr. Opin. Chem. Biol. 3 (1999) 182-187.

[51] R.J. Debus, Amino acid residues that modulate the properties of tyrosine Y_Z and the manganese cluster in the water oxidizing complex of photosystem II, Biochim. Biophys. Acta 1503 (2001) 164-186.

[52] D.B. Goodin, V.K. Yachandra, R.D. Britt, K. Sauer, M.P. Klein, The state of manganese in the photosynthetic apparatus. 3. Light-induced changes in x-ray absorption (K-edge) energies of manganese in photosynthetic membranes, Biochim. Biophys. Acta 767 (1984) 209-216.

[53] R.M. Cinco, A. Rompel, H. Visser, G. Aromi, G. Christou, K. Sauer, M.P. Klein, V.K. Yachandra, Comparison of the manganese cluster in oxygen-evolving photosystem II with distorted cubane manganese compounds through x-ray absorption spectroscopy, Inorg. Chem. 38 (1999) 5988-5998.

[54] J.B. Vincent, G. Christou, A molecular double-pivot mechanism for water oxidation, Inorg. Chim. Acta 136 (1987) L41-L43.

[55] W. Rüttinger, G.C. Dismukes, Synthetic water-oxidation catalysts for artificial photosynthetic water oxidation, Chem. Rev. 97 (1997) 1-24.

[56] G.W. Brudvig, R.H. Crabtree, Mechanism for photosynthetic O_2 evolution, Proc. Natl. Acad. Sci. USA 83 (1986) 4586-4588.

[57] K. Wieghardt, The active-sites in manganese-containing metalloproteins and inorganic model complexes, Angew. Chem. Int. Ed. Engl. 28 (1989) 1153-1172.

[58] V.L. Pecoraro, W.-Y. Hsieh, The use of model complexes to elucidate the structure and function of manganese redox enzymes, Met. Ions Biol. Syst. 37 (2000) 429-504.

[59] S. Mukhopadhyay, S.K. Mandal, S. Bhaduri, W.H. Armstrong, Manganese clusters with relevance to photosystem II, Chem. Rev. 104 (2004) 3981-4026.

[60] G. Christou, Manganese carboxylate chemistry and its biological relevance, Acc. Chem. Res. 22 (1989) 328-335.

[61] K. Sauer, V.K. Yachandra, R.D. Britt, M.P. Klein, The photosynthetic water oxidation complex studied by EPR and x-ray absorption spectroscopy, in: V.L. Pecoraro (Ed.), Manganese Redox Enzymes, VCH, New York, N.Y., 1992, p. Chapter 8.

[62] M.P. Klein, K. Sauer, V.K. Yachandra, Perspectives on the structure of the photosynthetic oxygen evolving manganese complex and its relation to the Kok cycle, Photosynth. Res. 38 (1993) 265-277.

[63] R.M. Cinco, K.L.M. Holman, J.H. Robblee, J. Yano, S.A. Pizarro, E. Bellacchio, K. Sauer, V.K. Yachandra, Calcium EXAFS establishes the Mn-Ca cluster in the oxygen-evolving complex of photosystem II, Biochemistry 41 (2002) 12928-12933.

[64] C. Müller, P. Liebisch, M. Barra, H. Dau, M. Haumann, The location of calcium in the manganese complex of oxygenic photosynthesis studied by X-ray absorption spectroscopy at the Ca K-edge, Phys. Scr. T115 (2005) 847-850.

[65] Y. Pushkar, J. Yano, K. Sauer, A. Boussac, V.K. Yachandra, Structural changes in the Mn_4Ca cluster and the mechanism of photosynthetic water splitting, Proc. Natl. Acad. Sci. USA 105 (2008) 1879-1884.

[66] N. Ishida, M. Sugiura, F. Rappaport, T.L. Lai, A.W. Rutherford, A. Boussac, Biosynthetic exchange of bromide for chloride and strontium for calcium in the photosystem II oxygen-evolving enzymes, J. Biol. Chem. 283 (2008) 13330-13340.

[67] V.J. DeRose, V.K. Yachandra, A.E. McDermott, R.D. Britt, K. Sauer, M.P. Klein, Nitrogen ligation to manganese in the photosynthetic oxygen-evolving complex: continuous-wave and pulsed EPR studies of photosystem II particles containing ^{14}N or ^{15}N, Biochemistry 30 (1991) 1335-1341.

[68] G.N. George, R.C. Prince, S.P. Cramer, The manganese site of the photosynthetic water-splitting enzyme, Science 243 (1989) 789-791.

[69] I. Mukerji, J.C. Andrews, V.J. DeRose, M.J. Latimer, V.K. Yachandra, K. Sauer, M.P. Klein, Orientation of the oxygen-evolving manganese complex in a photosystem II membrane preparation: an X-ray absorption spectroscopy study, Biochemistry 33 (1994) 9712-9721.

[70] W. Liang, M.J. Latimer, H. Dau, T.A. Roelofs, V.K. Yachandra, K. Sauer, M.P. Klein, Correlation between structure and magnetic spin state of the manganese cluster in the oxygen-evolving complex of photosystem II in the S_2 state: determination by X-ray absorption spectroscopy, Biochemistry 33 (1994) 4923-4932.

[71] H. Dau, J.C. Andrews, T.A. Roelofs, M.J. Latimer, W. Liang, V.K. Yachandra, K. Sauer, M.P. Klein, Structural consequences of ammonia binding to the manganese center of the photosynthetic oxygen-evolving complex: an X-ray absorption spectroscopy study of isotropic and oriented photosystem II particles, Biochemistry 34 (1995) 5274-5287.

[72] H. Schiller, J. Dittmer, L. Iuzzolino, W. Dörner, W. Meyer-Klaucke, V.A. Sole, H.-F. Nolting, H. Dau, Structure and orientation of the oxygen-evolving manganese complex of green algae and higher plants investigated by X-ray absorption linear dichroism spectroscopy on oriented photosystem II membrane particles, Biochemistry 37 (1998) 7340-7350.

[73] Y. Pushkar, J. Yano, P. Glatzel, J. Messinger, A. Lewis, K. Sauer, U. Bergmann, V. Yachandra, Structure and orientation of the Mn_4Ca cluster in plant photosystem II membranes studied by polarized range-extended X-ray absorption spectroscopy, J. Biol. Chem. 282 (2007) 7198-7208.

[74] R.M. Cinco, J.H. Robblee, J. Messinger, C. Fernandez, K.L.M. Holman, K. Sauer, V.K. Yachandra, Orientation of calcium in the Mn_4Ca cluster of the oxygen-evolving complex determined using polarized strontium EXAFS of photosystem II membranes, Biochemistry 43 (2004) 13271-13282.

[75] C. Meinke, V.A. Sole, P. Pospisil, H. Dau, Does the structure of the water-oxidizing photosystem II-manganese complex at room temperature differ from its low-temperature structure? A comparative X-ray absorption study, Biochemistry 39 (2000) 7033-7040.

[76] M. Haumann, M. Grabolle, T. Neisius, H. Dau, The first room-temperature X-ray absorption spectra of higher oxidation states of the tetra-manganese complex of photosystem II, FEBS Lett. 512 (2002) 116-120.

[77] M. Haumann, P. Pospisil, M. Grabolle, C. Müller, P. Liebisch, V.A. Sole, T. Neisius, J. Dittmer, L. Iuzzolino, H. Dau, First steps towards time-resolved BioXAS at room temperature: state transitions of the manganese complex of oxygenic photosynthesis, J. Synchrotron Rad. 9 (2002) 304-308.

[78] M. Haumann, C. Müller, P. Liebisch, L. Iuzzolino, J. Dittmer, M. Grabolle, T. Neisius, W. Meyer-Klaucke, H. Dau, Structural and oxidation state changes of the photosystem II manganese complex in four transitions of the water oxidation cycle ($S_0 \rightarrow S_1$, $S_1 \rightarrow S_2$, $S_2 \rightarrow S_3$, and $S_{3,4} \rightarrow S_0$) characterized by X-ray absorption spectroscopy at 20 K and room temperature, Biochemistry 44 (2005) 1894-1908.

[79] J.M. Peloquin, K.A. Campbell, D.W. Randall, M.A. Evanchik, V.L. Pecoraro, W.H. Armstrong, R.D. Britt, ^{55}Mn ENDOR of the S_2-state multiline EPR signal of photosystem II: implications on the structure of the tetranuclear Mn cluster, J. Am. Chem. Soc. 122 (2000) 10926-10942.

[80] C.W. Hoganson, N. Lydakis-Simantiris, X.S. Tang, C. Tommos, K. Warncke, G.T. Babcock, B.A. Diner, J. McCracken, S. Styring, A hydrogen-atom abstraction model for the function of Y_Z in photosynthetic oxygen-evolution, Photosynth. Res. 46 (1995) 177-184.

[81] C.W. Hoganson, G.T. Babcock, A metalloradical mechanism for the generation of oxygen from water in photosynthesis, Science 277 (1997) 1953-1956.

[82] C. Tommos, G.T. Babcock, Oxygen production in nature: a light-driven metalloradical enzyme process, Acc. Chem. Res. 31 (1998) 18-25.

[83] T.J. Meyer, M.H.V. Huynh, H.H. Thorp, The possible role of proton-coupled electron transfer (PCET) in water oxidation by photosystem II, Angew. Chem. Int. Ed. 46 (2007) 5284-5304.

[84] S. Hammes-Schiffer, Theory of proton-coupled electron transfer in energy conversion processes, Acc. Chem. Res. 42 (2009) 1881-1889.

[85] C. Carra, N. Iordanova, S. Hammes-Schiffer, Proton-coupled electron transfer in a model for tyrosine oxidation in photosystem II, J. Am. Chem. Soc. 125 (2003) 10429-10436.

[86] M. Sjödin, S. Styring, B. Akermark, L.C. Sun, L. Hammarström, Proton-coupled electron transfer from tyrosine in a tyrosine-ruthenium-tris-bipyridine complex: comparison with $tyrosine_Z$ oxidation in photosystem II, J. Am. Chem. Soc. 122 (2000) 3932-3936.

[87] R.I. Cukier, D.G. Nocera, Proton-coupled electron transfer, Annu. Rev. Phys. Chem. 49 (1998) 337-369.

[88] S.Y. Reece, D.G. Nocera, Proton-coupled electron transfer in biology: results from synergistic studies in natural and model systems, Annu. Rev. Biochem. 78 (2009) 673-699.

[89] H. Dau, C. Limberg, T. Reier, M. Risch, S. Roggan, P. Strasser, The mechanism of water oxidation: from electrolysis via homogeneous to biological catalysis, ChemCatChem 2 (2010) 724-761.

[90] H. Dau, M. Haumann, Eight steps preceding O-O bond formation in oxygenic photosynthesis—a basic reaction cycle of the photosystem II manganese complex, Biochim. Biophys. Acta 1767 (2007) 472-483.

[91] J. Yano, J. Kern, K. Sauer, M.J. Latimer, Y. Pushkar, J. Biesiadka, B. Loll, W. Saenger, J. Messinger, A. Zouni, V.K. Yachandra, Where water is oxidized to dioxygen: structure of the photosynthetic Mn_4Ca cluster, Science 314 (2006) 821-825.

[92] H. Dau, A. Grundmeier, P. Loja, M. Haumann, On the structure of the manganese complex of photosystem II: extended-range EXAFS data and specific atomic-resolution models for four S-states, Phil. Trans. R. Soc. B 363 (2008) 1237-1244.

[93] H. Dau, J. Dittmer, M. Epple, J. Hanss, E. Kiss, D. Rehder, C. Schulzke, H. Vilter, Bromine K-edge EXAFS studies of bromide binding to bromoperoxidase from *Ascophyllum nodosum*, FEBS Lett. 457 (1999) 237-240.

[94] D. Rehder, C. Schulzke, H. Dau, C. Meinke, J. Hanss, M. Epple, Water and bromide in the active center of vanadate-dependent haloperoxidases, J. Inorg. Biochem. 80 (2000) 115-121.

[95] M. Haumann, M. Barra, P. Loja, S. Loscher, R. Krivanek, A. Grundmeier, L.E. Andreasson, H. Dau, Bromide does not bind to the Mn_4Ca complex in its S_1 state in Cl^--depleted and Br^--reconstituted oxygen-evolving photosystem II: evidence from X-ray absorption spectroscopy at the Br K-edge, Biochemistry 45 (2006) 13101-13107.

[96] R. Pokhrel, I.L. McConnell, G.W. Brudvig, Chloride regulation of enzyme turnover: application to the role of chloride in photosystem II, Biochemistry 50 (2011) 2725-2734.

[97] H. Dau, J. Dittmer, L. Iuzzolino, H. Schiller, W. Dörner, I. Heinze, V.A. Sole, H.-F. Nolting, X-ray absorption linear dichroism spectroscopy (XALDS) on the photosystem II manganese complex: Radiation damage and S_1-state K-edge spectra, J. Phys. IV 7 (1997) 607-610.

[98] J. Yano, J. Kern, K.-D. Irrgang, M.J. Latimer, U. Bergmann, P. Glatzel, Y. Pushkar, J. Biesiadka, B. Loll, K. Sauer, J. Messinger, A. Zouni, V.K. Yachandra, X-ray damage to the Mn_4Ca complex in single crystals of photosystem II: a case study for metalloprotein crystallography, Proc. Natl. Acad. Sci. USA 102 (2005) 12047-12052.

[99] M. Grabolle, M. Haumann, C. Müller, P. Liebisch, H. Dau, Rapid loss of structural motifs in the manganese complex of oxygenic photosynthesis by X-ray irradiation at 10-300 K, J. Biol. Chem. 281 (2006) 4580-4588.

[100] M. O'Keeffe, N.E. Brese, Atom sizes and bond lengths in molecules and crystals, J. Am. Chem. Soc. 113 (1991) 3226-3229.

[101] N.E. Brese, M. O'Keeffe, Bond-valence parameters for solids, Acta Crystallogr. B 47 (1991) 192-197.

[102] H. Dau, M. Haumann, Reaction cycle of photosynthetic water oxidation in plants and cyanobacteria (response letter), Science 312 (2006) 1471-1472.

[103] C.A. Ashley, S. Doniach, Theory of extended x-ray absorption edge fine structure (EXAFS) in crystalline solids, Phys. Rev. B: Condens. Matter 11 (1975) 1279-1288.

[104] J. Mustre de Leon, J.J. Rehr, S.I. Zabinsky, R.C. Albers, *Ab initio* curved-wave x-ray-absorption fine structure, Phys. Rev. B: Condens. Matter 44 (1991) 4146-4156.

[105] S.I. Zabinsky, J.J. Rehr, A.L. Ankudinov, R.C. Albers, M.J. Eller, Multiple-scattering calculations of x-ray-absorption spectra, Phys. Rev. B: Condens. Matter 52 (1995) 2995-3009.

[106] A.L. Ankudinov, B. Ravel, J.J. Rehr, S.D. Conradson, Real-space multiple-scattering calculation and interpretation of x-ray-absorption near-edge structure, Phys. Rev. B: Condens. Matter 58 (1998) 7565-7576.

[107] J.J.A. Rehr, A.; Zabinsky, S. I., New developments in NEXAFS/EXAFS theory, Catal. Today 39 (1998) 263-269.

[108] P. Eisenberger, B.M. Kincaid, EXAFS: new horizons in structure determinations, Science 200 (1978) 1441-1447.

[109] A. Bianconi, A. Di Cicco, N.V. Pavel, M. Benfatto, A. Marcelli, C.R. Natoli, P. Pianetta, J. Woicik, Multiple-scattering effects in the K-edge x-ray-absorption near-edge structure of crystalline and amorphous silicon, Phys. Rev. B: Condens. Matter 36 (1987) 6426–6433.

[110] M. Benfatto, C.R. Natoli, C. Brouder, R.F. Pettifer, M.F. Ruiz Lopez, Polarized curved-wave extended x-ray-absorption fine structure: Theory and application, Phys. Rev. B: Condens. Matter 39 (1989) 1936–1939.

[111] N. Binsted, S.S. Hasnain, State-of-the-art analysis of whole x-ray absorption spectra, J. Synchrotron Rad. 3 (1996) 185-196.

[112] E.M. Sproviero, M.B. Newcomer, J.A. Gascon, E.R. Batista, G.W. Brudvig, V.S. Batista, The MoD-QM/MM methodology for structural refinement of photosystem II and other biological macromolecules, Photosynth. Res. 102 (2009) 455-470.

[113] G.W. Brudvig, Water oxidation chemistry of photosystem II, Phil. Trans. R. Soc. B 363 (2008) 1211-1219.

[114] E.M. Sproviero, J.A. Gascon, J.P. McEvoy, G.W. Brudvig, V.S. Batista, Quantum mechanics/molecular mechanics structural models of the oxygen-evolving complex of photosystem II, Curr. Opin. Struct. Biol. 17 (2007) 173-180.

[115] J.P. McEvoy, J.A. Gascon, V.S. Batista, G.W. Brudvig, The mechanism of photosynthetic water splitting, Photochem. Photobiol. Sci. 4 (2005) 940-949.

[116] J.P. McEvoy, G.W. Brudvig, Structure-based mechanism of photosynthetic water oxidation, Phys. Chem. Chem. Phys. 6 (2004) 4754-4763.

[117] E.M. Sproviero, J.A. Gascon, J.P. McEvoy, G.W. Brudvig, V.S. Batista, Computational studies of the O_2-evolving complex of photosystem II and biomimetic oxomanganese complexes, Coord. Chem. Rev. 252 (2008) 395-415.

[118] E.M. Sproviero, J.A. Gascon, J.P. McEvoy, G.W. Brudvig, V.S. Batista, Quantum mechanics/molecular mechanics study of the catalytic cycle of water splitting in photosystem II, J. Am. Chem. Soc. 130 (2008) 3428-3442.

[119] E.M. Sproviero, J.A. Gascon, J.P. McEvoy, G.W. Brudvig, V.S. Batista, A model of the oxygen-evolving center of photosystem II predicted by structural refinement based on EXAFS simulations, J. Am. Chem. Soc. 130 (2008) 6728-6730.

[120] H. Dau, P. Liebisch, M. Haumann, The manganese complex of oxygenic photosynthesis: Conversion of five-coordinated Mn(III) to six-coordinated Mn(IV) in the S_2-S_3 transition is implied by XANES simulations, Phys. Scr. T115 (2005) 844-846.

[121] P.E. Siegbahn, Structures and energetics for O_2 formation in Photosystem II, Acc. Chem. Res. 42 (2009) 1871-1880.

[122] P.E. Siegbahn, A structure-consistent mechanism for dioxygen formation in photosystem II, Chem. Eur. J. 14 (2008) 8290-8302.

[123] H. Schiller, H. Dau, Preparation protocols for high-activity photosystem II membrane particles of green algae and higher plants, pH dependence of oxygen evolution and comparison of the S_2-state multiline signal by X-band EPR spectroscopy, J. Photochem. Photobiol. B 55 (2000) 138-144.

[124] L. Iuzzolino, J. Dittmer, W. Dörner, W. Meyer-Klaucke, H. Dau, X-ray absorption spectroscopy on layered photosystem II membrane particles suggests manganese-centered oxidation of the oxygen-evolving complex for the S_0-S_1, S_1-S_2, and S_2-S_3 transitions of the water oxidation cycle, Biochemistry 37 (1998) 17112-17119.

[125] Z.J. Gu, J. Dong, C.B. Allan, S.B. Choudhury, R. Franco, J.J.G. Moura, J. LeGall, A.E. Przybyla, W. Roseboom, S.P.J. Albracht, M.J. Axley, R.A. Scott, M.J. Maroney, Structure of the Ni sites in hydrogenases by x-ray absorption spectroscopy. Species variation and the effects of redox poise, J. Am. Chem. Soc. 118 (1996) 11155-11165.

[126] J. Yano, Y. Pushkar, P. Glatzel, A. Lewis, K. Sauer, J. Messinger, U. Bergmann, V. Yachandra, High-resolution Mn EXAFS of the oxygen-evolving complex in photosystem II: structural implications for the Mn_4Ca cluster, J. Am. Chem. Soc. 127 (2005) 14974-14975.

[127] D.A. Berthold, G. T. Babcock, et al., A highly resolved, oxygen-evolving photosystem II preparation from spinach thylakoid membranes: EPR and electron-transport properties FEBS Lett. 134 (1981) 231-234.

[128] H. Blum, J.C. Salerno, J.S.J. Leigh, A model for the simulation of EPR spectra of chromophores in partially oriented membrane multilayers, J. Magn. Reson. 30 (1978) 385-391.

[129] M. Haumann, M. Grabolle, M. Werthammer, L. Iuzzolino, J. Dittmer, W. Meyer-Klaucke, T. Neisius, H. Dau, The manganese complex of Photosystem II: A structural model for the S_1, S_2, and S_3 oxidation states derived from linear dichroism EXAFS spectroscopy at 20 K and at room temperature, PS2001: Proceedings of the 12th International Congress on Photosynthesis, CSIRO Publishing, Melbourne, Australia, Brisbane, Australia, 2001, pp. S10-013 011-015.

[130] J. Dittmer, H. Dau, Theory of the linear dichroism in the extended x-ray absorption fine structure (EXAFS) of partially vectorially ordered systems, J. Phys. Chem. B 102 (1998) 8196-8200.

[131] P. Liebisch, H. Dau, Linear dichroism in the XANES of partially oriented samples: theory and application to the photosynthetic manganese complex, ChemPhysChem 11 (2010) 1236-1247.

[132] A.L. Ankudinov, J.J. Rehr, Development of XAFS theory, J. Synchrotron Rad. 10 (2003) 366-368.

[133] J.J. Rehr, R.C. Albers, Theoretical approaches to x-ray absorption fine structure, Rev. Mod. Phys. 72 (2000) 621-654.

[134] S. Schinzel, J. Schraut, A.V. Arbuznikov, P.E.M. Siegbahn, M. Kaupp, Density functional calculations of ^{55}Mn, ^{14}N and ^{13}C electron paramagnetic resonance parameters support an energetically feasible model system for the S_2 state of the oxygen-evolving complex of photosystem II, Chem. Eur. J. 16 (2010) 10424-10438.

[135] T. Ono, T. Noguchi, Y. Inoue, M. Kusunoki, T. Matsushita, H. Oyanagi, X-ray detection of the period-four cycling of the manganese cluster in photosynthetic water oxidizing enzyme, Science 258 (1992) 1335-1337.

[136] J. Messinger, J.H. Robblee, U. Bergmann, C. Fernandez, P. Glatzel, H. Visser, R.M. Cinco, K.L. McFarlane, E. Bellacchio, S.A. Pizarro, S.P. Cramer, K. Sauer, M.P. Klein, V.K. Yachandra, Absence of Mn-centered oxidation in the $S_2 \rightarrow S_3$ transition: implications for the mechanism of photosynthetic water oxidation, J. Am. Chem. Soc. 123 (2001) 7804-7820.

[137] T.A. Roelofs, W. Liang, M.J. Latimer, R.M. Cinco, A. Rompel, J.C. Andrews, K. Sauer, V.K. Yachandra, M.P. Klein, Oxidation states of the manganese cluster during the flash-induced S-state cycle of the photosynthetic oxygen-evolving complex, Proc. Natl. Acad. Sci. USA 93 (1996) 3335-3340.

[138] J.H. Robblee, R.M. Cinco, V.K. Yachandra, X-ray spectroscopy-based structure of the Mn cluster and mechanism of photosynthetic oxygen evolution, Biochim. Biophys. Acta 1503 (2001) 7-23.

[139] R.L. Burnap, D1 protein processing and Mn cluster assembly in light of the emerging photosystem II structure, Phys. Chem. Chem. Phys. 6 (2004) 4803-4809.

[140] J. Dasgupta, G.M. Ananyev, G.C. Dismukes, Photoassembly of the water-oxidizing complex in photosystem II, Coord. Chem. Rev. 252 (2008) 347-360.

[141] P. Pospíšil, M. Haumann, J. Dittmer, V.A. Solé, H. Dau, Stepwise transition of the tetra-manganese complex of photosystem II to a binuclear $Mn_2(\mu\text{-}O)_2$ complex in response to a temperature jump: a timeresolved structural investigation employing X-ray absorption spectroscopy, Biophys. J. 84 (2003) 1370-1386.

[142] M. Barra, M. Haumann, P. Loja, R. Krivanek, A. Grundmeier, H. Dau, Intermediates in assembly by photoactivation after thermally accelerated disassembly of the manganese complex of photosynthetic water oxidation, Biochemistry 45 (2006) 14523-14532.

[143] M. Barra, M. Haumann, H. Dau, Specific loss of the extrinsic 18 kDa protein from photosystem II upon heating to 47 °C causes inactivation of oxygen evolution likely due to Ca release from the Mn-complex, Photosynth. Res. 84 (2005) 231-237.

[144] C. Tommos, C.W. Hoganson, M. Di Valentin, N. Lydakis-Simantiris, P. Dorlet, K. Westphal, H.A. Chu, J. McCracken, G.T. Babcock, Manganese and tyrosyl radical function in photosynthetic oxygen evolution, Curr. Opin. Chem. Biol. 2 (1998) 244-252.

[145] W. Hillier, T. Wydrzynski, ^{18}O-Water exchange in photosystem II: substrate binding and intermediates of the water splitting cycle, Coord. Chem. Rev. 252 (2008) 306-317.

[146] W. Hillier, T. Wydrzynski, Substrate water interactions within the photosystem II oxygen evolving complex, Phys. Chem. Chem. Phys. 6 (2004) 4882-4889.

[147] W. Hillier, T. Wydrzynski, Oxygen ligand exchange at metal sites—implications for the O_2 evolving mechanism of photosystem II, Biochim. Biophys. Acta 1503 (2001) 197-209.

[148] W. Hillier, G. Hendry, R.L. Burnap, T. Wydrzynski, Substrate water exchange in photosystem II depends on the peripheral proteins, J. Biol. Chem. 276 (2001) 46917-46924.

[149] W. Hillier, T. Wydrzynski, The affinities for the two substrate water binding sites in the O_2 evolving complex of photosystem II vary independently during S-state turnover, Biochemistry 39 (2000) 4399-4405.

[150] W. Hillier, J. Messinger, T. Wydrzynski, Kinetic determination of the fast exchanging substrate water molecule in the S_3 state of photosystem II, Biochemistry 37 (1998) 16908-16914.

[151] J. Messinger, M. Badger, T. Wydrzynski, Detection of *one* slowly exchanging substrate water molecule in the S_3 state of photosystem II, Proc. Natl. Acad. Sci. USA 92 (1995) 3209-3213.

[152] R. Tagore, H. Chen, H. Zhang, R.H. Crabtree, G.W. Brudvig, Homogeneous water oxidation by a di-μ-oxo dimanganese complex in the presence of Ce^{4+}, Inorg. Chim. Acta 360 (2007) 2983-2989.

[153] R. Tagore, H. Chen, R.H. Crabtree, G.W. Brudvig, Determination of μ-oxo exchange rates in di-μ-oxo dimanganese complexes by electrospray ionization mass spectrometry, J. Am. Chem. Soc. 128 (2006) 9457-9465.

[154] J. Barber, Photosynthetic energy conversion: natural and artificial, Chem. Soc. Rev. 38 (2009) 185-196.

[155] J. Barber, J.W. Murray, Revealing the structure of the Mn-cluster of photosystem II by X-ray crystallography, Coord. Chem. Rev. 252 (2008) 233-243.

[156] E.M. Sproviero, J.P. McEvoy, J.A. Gascón, G.W. Brudvig, V.S. Batista, Computational insights into the O_2-evolving complex of photosystem II, Photosynth. Res. 97 (2008) 91-114.

[157] H. Dau, M. Haumann, Considerations on the mechanism of photosynthetic water oxidation—dual role of oxo-bridges between Mn ions in (i) redox-potential maintenance and (ii) proton abstraction from substrate water, Photosynth. Res. 84 (2005) 325-331.

[158] H. Dau, I. Zaharieva, Principles, efficiency, and blueprint character of solar-energy conversion in photosynthetic water oxidation, Acc. Chem. Res. 42 (2009) 1861-1870.

[159] K. Cser, I. Vass, Radiative and non-radiative charge recombination pathways in Photosystem II studied by thermoluminescence and chlorophyll fluorescence in the cyanobacterium Synechocystis 6803, Biochim. Biophys. Acta 1767 (2007) 233-243.

[160] F. Rappaport, M. Guergova-Kuras, P.J. Nixon, B.A. Diner, J. Lavergne, Kinetics and pathways of charge recombination in Photosystem II, Biochemistry 41 (2002) 8518-8527.

[161] M. Grabolle, H. Dau, Energetics of primary and secondary electron transfer in Photosystem II membrane particles of spinach revisited on basis of recombination-fluorescence measurements, Biochim. Biophys. Acta 1708 (2005) 209-218.

[162] F. Rappaport, B.A. Diner, Primary photochemistry and energetics leading to the oxidation of the (Mn)4Ca cluster and to the evolution of molecular oxygen in Photosystem II, Coord. Chem. Rev. 252 (2008) 259-272.

[163] M. Grabolle, H. Dau, Efficiency and role of loss processes in light-driven water oxidation by PSII, Physiol. Plant. 131 (2007) 50-63.

[164] B. Kok, B. Forbush, M. McGloin, Cooperation of charges in photosynthetic O_2 evolution - I. A linear four-step mechanism, Photochem. Photobiol. 11 (1970) 457-475.

[165] H. Dau, M. Haumann, Time-resolved X-ray spectroscopy leads to an extension of the classical S-state cycle model of photosynthetic oxygen evolution, Photosynth. Res. 92 (2007) 327-343.

[166] I. Zaharieva, J.M. Wichmann, H. Dau, Thermodynamic limitations of photosynthetic water oxidation at high proton concentrations, J Biol Chem (2011).

[167] G. Bernat, F. Morvaridi, Y. Feyziyev, S. Styring, pH-dependence of the four individual transitions in the catalytic S-cycle during photosynthetic oxygen evolution, Biochemistry 41 (2002) 5830-5843.

[168] H. Suzuki, M. Sugiura, T. Noguchi, pH dependence of the flash-induced S-state transitions in the oxygen-evolving center of photosystem II from *Thermosynechoccocus elongatus* as revealed by Fourier transform infrared spectroscopy, Biochemistry 44 (2005) 1708-1718.

[169] W. Liang, T.A. Roelofs, R.M. Cinco, A. Rompel, M.J. Latimer, W.O. Yu, K. Sauer, M.P. Klein, V.K. Yachandra, Structural change of the Mn cluster during the $S_2 \rightarrow S_3$ state transition of the oxygen-evolving complex of photosystem II. Does it reflect the onset of water/substrate oxidation? Determination by Mn x-ray absorption spectroscopy, J. Am. Chem. Soc. 122 (2000) 3399-3412.

[170] J.H. Robblee, J. Messinger, R.M. Cinco, K.L. McFarlane, C. Fernandez, S.A. Pizarro, K. Sauer, V.K. Yachandra, The Mn cluster in the S_0 state of the oxygen-evolving complex of photosystem II studied by EXAFS spectroscopy: are there three di-μ-oxo-bridged Mn_2 moieties in the tetranuclear Mn complex?, J. Am. Chem. Soc. 124 (2002) 7459-7471.

[171] P. Glatzel, U. Bergmann, J. Yano, H. Visser, J.H. Robblee, W. Gu, F.M. de Groot, G. Christou, V.L. Pecoraro, S.P. Cramer, V.K. Yachandra, The electronic structure of Mn in oxides, coordination complexes, and the oxygen-evolving complex of photosystem II studied by resonant inelastic X-ray scattering, J. Am. Chem. Soc. 126 (2004) 9946-9959.

[172] H. Visser, E. Anxolabehere-Mallart, U. Bergmann, P. Glatzel, J.H. Robblee, S.P. Cramer, J.-J. Girerd, K. Sauer, M.P. Klein, V.K. Yachandra, Mn K-edge XANES and Kβ XES studies of two Mn-oxo binuclear complexes: investigation of three different oxidation states relevant to the oxygen-evolving complex of photosystem II, J. Am. Chem. Soc. 123 (2001) 7031-7039.

[173] U. Bergmann, P. Glatzel, F. deGroot, S.P. Cramer, High resolution K capture X-ray fluorescence spectroscopy: a new tool for chemical characterization, J. Am. Chem. Soc. 121 (1999) 4926-4927.

[174] U. Bergmann, M.M. Grush, C.R. Horne, P. DeMarois, J.E. Penner-Hahn, C.F. Yocum, D.W. Wright, C.E. Dube, W.H. Armstrong, G. Christou, H.J. Eppley, S.P. Cramer, Characterization of the Mn oxidation states in photosystem II by Kβ X-ray fluorescence spectroscopy, J. Phys. Chem. B 102 (1998) 8350-8352.

[175] G. Smolentsev, A.V. Soldatov, J. Messinger, K. Merz, T. Weyhermüller, U. Bergmann, Y. Pushkar, J. Yano, V.K. Yachandra, P. Glatzel, X-ray emission spectroscopy to study ligand valence orbitals in Mn coordination complexes, J. Am. Chem. Soc. 131 (2009) 13161-13167.

[176] I. Zaharieva, P. Chernev, M. Risch, L. Gerencsér, G. Berggren, G. Shevchenko, M. Anderlund, T.-C. Weng, M. Haumann, H. Dau, Towards a comprehensive X-ray approach for studying the photosynthetic manganese complex—XANES, Kα/Kβ/Kβ-satellite emission lines, RIXS, and comparative computational approaches for selected model complexes, J. Physics: Conf. Series 190 (2009) 012142, 012141-012146.

TABLES

Table 1. EXAFS results on metal-metal distances in the Mn_4Ca complex of PSII in its dark-stable state (S_1). The value of *n* given in the fourth column provides the number of Mn-Mn or Mn-Ca vectors of the length indicated in the third column; its value is not identical to the EXAFS coordination number but corresponds to the number of vectors per Mn_4Ca complex. (The here summarized results were all obtained without any significant bias towards a distinct model meaning that they are largely model-independent.)

no.		Distance	*n*	Assessment	avg. θ_R
1	Mn-Mn	2.65-2.8 Å	2	clearly present	> 60°
2	Mn-Mn	2.8-2.9 Å	0 or 1	presence disputed	(> 60°)
3	Mn-Mn	2.9-3.1 Å	n.d.	possibly present	--
4	Mn-Ca	3.2-3.6 Å	≥2	undisputed	< 45°
5	Mn-Mn	~3.3 Å	1?	repeatedly proposed	(> 60°)
6	Mn-Ca	~3.7 Å	?	in conflict with Ca/Sr-EXAFS (?)	--
7	Mn-Mn	~3.7 Å	1?	recently proposed [92]	--
8	Mn-Mn	~4.8 Å	1?	possibly present (this work)	--
9	Mn-Me	> 5 Å	n.d.	identification would be impossible	--

Table 2. Metal-metal distances (R) and angles between metal-metal vectors and membrane normal (θ_R). The header row indicates the respective OEC model, shown schematically in Fig. 4 (A-IIa), Fig. 2 (B-I, B-II), Fig. 11 (C-I, C-II, C-III, D), and Fig. 5A (E-A/E-B). In the crystallographic model of Umena *et al* [44], the coordinates determined for the two PSII monomers of the dimeric PSII are not identical; the abbreviations 'E-A' and 'E-B' refer to the monomers A and B, respectively. The second row indicates the open coordination site of a (quasi-)five-coordinated Mn(III) ion with a Mn^1-O^x distance exceeding 2.4 Å. In the last row, an error sum is given (in arbitrary units), which provides a measure of the deviations between calculated and experimental spectra taking into account the *Iso*, *Mem*, and *Cry* data sets (see section 3). The short Mn-Mn vectors are emphasized by bold printing and a grey background.

	A-IIa		**B-I**		**B-II**		**C-I**		**C-II**		**C-III**		**C-IV**		**E-A**		**E-B**	
> 2.4 Å							Mn^1-O^a		Mn^1-O^a		Mn^1-O^d		Mn^1-O^d					
atom pair	R/Å	θ_R	R/Å	θ_R	R/Å	θ_R	R/Å	θ_R	R/Å	θ_R	R/Å	θ_R	R/Å	θ_R	R/Å	θ_R	R/Å	θ_R
Mn^1-Mn^2	**2.80**	**57°**	**2.76**	**60°**	**2.74**	**58°**	2.99	77°	3.07	89°	**2.73**	**75°**	**2.73**	**72°**	**2.84**	**74°**	**2.76**	**74°**
Mn^1-Mn^3	**2.70**	**50°**	**2.82**	**65°**	**2.77**	**68°**	3.13	87°	3.22	86°	3.19	70°	3.17	78°	3.29	86°	3.30	87°
Mn^1-Mn^4	4.96	41°	3.34	54°	3.34	55°	3.72	59°	3.70	58°	3.72	70°	4.33	63°	5.00	64°	4.95	63°
Mn^2-Mn^3	3.28	86°	**2.76**	**86°**	**2.63**	**81°**	**2.69**	**79°**	**2.75**	**84°**	**2.71**	**82°**	**2.70**	**86°**	**2.89**	**78°**	**2.91**	**79°**
Mn^2-Mn^4	5.50	66°	5.38	52°	5.40	52°	4.85	58°	4.81	66°	4.79	66°	5.04	56°	5.44	56°	5.37	56°
Mn^3-Mn^4	**2.72**	**42°**	3.72	33°	3.68	37°	**2.73**	**40°**	**2.69**	**50°**	3.03	39°	3.03	31°	**2.97**	**35°**	**2.91**	**33°**
Mn^1-Ca	4.36	6°	3.31	50°	3.29	50°	3.26	41°	3.23	26°	3.64	50°	3.37	45°	3.51	45°	3.46	45°
Mn^2-Ca	3.39	34°	3.59	12°	3.57	8°	3.26	15°	3.38	29°	3.34	25°	3.27	9°	3.36	13°	3.29	12°
Mn^3-Ca	3.40	40°	3.95	33°	3.88	36°	3.37	39°	3.62	42°	3.67	22°	3.74	36°	3.41	38°	3.44	40°
Mn^4-Ca	3.61	81°	3.84	87°	4.12	87°	3.38	81°	3.44	74°	3.39	72°	3.72	83°	3.79	86°	3.80	87°
Mn-Ca avg. angle	3.69	41°	3.67	44°	3.72	44°	3.32	43°	3.42	42°	3.51	42°	3.53	43°	3.52	44°	3.50	44°
Error	5.6		18.2		5.8		5.2		1.4		1.2		1.3		50.2		42.9	

FIGURE CAPTIONS

Figure 1. In **A**, dimer-of-dimers model as proposed in 1993 by Yachandra *et al* [32] (for the Mn complex of PSII in its S_1 and S_2 state) and, in **B,** the 'dangler' arrangement of Britt and coworkers [79]. Oxygen atoms are depicted as open spheres; the other atom types are indicated in the scheme. (The shown schematic presentations were obtained by modification of the corresponding schemes in [32] and [79].)

Figure 2. OEC model derived by Batista, Brudvig, Sproviero, and their coworkers [114-115, 118-119] from the crystallographic model presented in 2004 by Barber and coworkers [38] (for the OEC in its S_1 state). The shown OEC model largely resembles the original proposal of Ferreira *et al* [38]. Important modifications have been the removal of the originally suggested bicarbonate ligand and complementation by additional water molecules (or hydroxides). The coordinates used in this presentation correspond to the refined model of Sproviero *et al* [119] obtained by optimizing the agreement with respect to the polarized EXAFS data of Yano *et al* [91]. All depicted residues are from the D1 protein of PSII, with the exception of Glu354, which is a residue of the CP43 protein. The indicated *z*-axis parallels the membrane normal; the *x*-axis parallels a vector that connects the two non-heme iron ions of the PSII dimer and points toward the monomer that does not contain the depicted Mn complex.

Figure 3. OEC model of Dau *et al* [92]. The protein ligands are assigned to Mn ions as proposed by Loll *et al* [39]. This OEC model was obtained by a combination of molecular mechanics modeling with results obtained by X-ray absorption spectroscopy. The overall geometry is similar to the DFT-based model of Siegbahn [121-122] and the recent crystallographic model of Shen and coworkers. Apart from the Tyr_Z proton (Tyr161) that is hydrogen-bonded to His190, protons are not shown. Hydrogen bonds are depicted in form of dashed lines. The Mn^1 ion is assumed to be quasi five-coordinated resulting in a relative long Mn^1-O^a distance (broken-stick presentation of this bond). Voids in the depicted OEC model suggest that 2-4 additional water molecules are located close to Mn^4. All depicted residues are from the D1 protein of PSII, with the exception of Glu354, which is a residue of the CP43 protein.

Figure 4. Alternative models for the OEC core proposed by Yano *et al* [91] (for the OEC in its S_1 state). All four models have been based on the polarized EXAFS spectra collected on PSII crystals.

Figure 5. Crystallographic OEC model of Umena *et al* [44] obtained by XRD at 1.9 Å resolution. In **A**, the same color code and perspective is used as in Figs. 2 and 3. All Mn-O bonds exceeding a length of 2.3 Å are depicted as broken sticks. The O atoms of selected water molecules are shown as red spheres; putative connections by hydrogen bonds are depicted in form of broken blue lines. In **B**, the crystallographic models of Loll *et al* [39] (blue ball-and-stick model) and Umena *et al* [44] (colored by element code) are compared. The spheres labeled by 1, 2, 3, 4, and Ca indicate the position of the metal ions in the model of Loll *et al,* whereas the primed numbers (and Ca') refer to the metal positions in the model of Umena *et al*.

Figure 6. Geometries in polarized EXAFS studies. In A, the geometry for polarized EXAFS on partially oriented PSII membrane particles is shown. The substrate plane (gray rectangle) and three exemplary thylakoid membrane sheets (white) are schematically shown. For one of the membrane sheets, also the PSII dimers and the direction of the membrane normal, *M*, are depicted. The vector labeled by *S* (sample normal) describes the normal of the macroscopic sample; *E* indicates the direction of the electric field vector of the X-ray beam. For

measurements and calculations of spectra, the excitation angle, θ_E, measured between *S* and *E* was varied. In B, the unit cell of crystallized PSII with its four PSII dimers is shown schematically (space group $P2_12_12_1$). The numbers 1 to 8 mark the positions of the eight Mn complexes of PSII within the unit cell. For the measurements described by Yano *et al* [91], the electric field vector of the X-ray beam was parallel to one of the three unit cell axes (either *a* or *b* or *c*). PSII coordinates and unit-cell size were taken from the XRD model of Loll *et al* [39].

Figure 7. Isotropic, extended-range EXAFS spectrum [92] (OEC in its S_1 state, *Iso* data). The experimental results are depicted as open circles, the EXAFS simulation for model C-II as a solid line. The original photon-energy scale of the EXAFS data has been converted to a *k*-scale and weighted by k^3 (*k* relates to the wavevector amplitude of the photoelectron). Typically an EXAFS spectrum is collected up to 11.5 $Å^{-1}$. The here shown spectrum extends to almost 17 Å, thereby increasing the information content of the EXAFS significantly. The Fourier-transformed EXAFS spectra shown in the following figures were obtained by Fourier transformation of the *k*-space data extending from 3.5 to 11.5 $Å^{-1}$.

Figure 8. Fourier transform of polarized EXAFS spectra collected on partially oriented PSII membrane particles (OEC in its S_1 state) at four excitation angles (θ_E in Fig. 6; *Mem* and *Iso* data). Spectra calculated for model C-II are shown in the lower panel.

Figure 9. Fourier transform of polarized EXAFS spectra collected by Yano *et al* on PSII crystals [91] (*Cry* data). For each spectrum, the X-ray electric field vector had been aligned along one of the three crystal axes (*a*, *b*, *c* in Fig. 6B) [91]. Spectra calculated for model C-II are shown in the lower panel.

Figure 10. Bar diagram of the magnitude of the second FT peak calculated for alternative structural models and in the experimental spectra. The upper panel relates to the polarized EXAFS spectra obtained from PSII crystals (*Cry* data); the lower panel relates to the polarized EXAFS collected on partially oriented PSII membrane particles (*Mem* data). The color coding in the lower and upper panel corresponds to the color codes used in Fig. 8 and Fig. 9, respectively. The error bars indicate the 2σ–error estimated from the FT amplitudes at reduced distances ranging from 5.5 to 8 Å, which are attributable to noise contributions only. (This error estimate itself also is associated with its own statistical error. We feel that the error in the 75°-spectrum of the *Mem* data likely is greater than suggested by the indicated error bar.)

Figure 11. Related models of the $Mn_4Ca(\mu\text{-}O)_4$ core of the OEC (in its S_1 state). The here shown structural models of the OEC core result in calculated EXAFS spectra that resemble the three experimental data sets (*Iso, Mem*, and *Cry*) reasonably well.

Figure 12. Alternative modes proposed for O-O bond formation.

Figure 13. Model C-II after modification of the protein environment according to the recent crystallographic model of Shen and coworkers [44]. The schematic representation illustrates that a nucleophilic attack of a water (or hydroxide) ligand of the Ca ion (O^{W3}) on a oxyl ligand of Mn^4 (O^{W2}) is sterically not excluded. It is indicated that O^{W3} and O^{W2} could approach each other up to distance of less than 3 Å without any sterical hindrance aside from the mutual repulsion of O^{W3} and O^{W2} by non-bonding interactions. The here selected perspective also illustrates a coordination geometry of Asp170 that is strongly twisted and appears to be highly strained, in clear contrast to the other bidentate carboxylate ligands of the $Mn_4Ca(\mu\text{-}O)_5$ core.

Figure 14. Classical S-state cycle of photosynthetic water oxidation (Kok cycle [164-165]). Starting in the dark-stable S_1 state, absorption of a photon causes formation of $Y_Z^{\bullet+}$ within

less than one μs. Reduction of $Y_Z^{\bullet+}$ by electron transfer (ET) from the Mn complex results in the $S_i \rightarrow S_{i+1}$ transition; typical time constants of the ET step are indicated. A plausible set of oxidation-state combinations of the four Mn ions is shown. We note that also the presence of Mn^{II} in S_0 and of a ligand radical in S_3 (as well as delocalized valencies) have been discussed.

Figure 15. Extended S-state cycle involving nine states of the Mn complex of PSII. Kok's classical S-state cycle model [164] is extended by including not only four oxidation but also four deprotonation steps [90, 102]. Four of the nine intermediates are stable for tens of seconds or fully dark-stable (S_1^n, S_2^+, S_3^+, and S_0^n). They correspond to the states S_1, S_2, S_3, and S_0 of Kok's reaction cycle and are marked by a rectangular frame. Electrons and protons are removed alternately from the Mn complex by electron transfer to the oxidized Tyr_Z ($Y_Z^{\bullet+}$) and proton relocation towards the aqueous phase, respectively. However for each of the individual S-state transition between semi-stable S-states (rectangular frame), a specific sequence of ET and proton removal from the OEC is predicted. We emphasize that proton removal from the catalytic site does not necessarily imply deprotonation of water species. The nine intermediate states of the Mn complex are denoted as $S_i^{+/n}$ where the subscript gives the number of accumulated oxidizing equivalents and the superscript indicates the relative charge: positive (+) or neutral (n) relative to the dark-stable S_1-state [13]. (The shown reaction cycle has been discussed previously [90, 102, 165] using a nomenclature where the nine states from S_0^+ to S_4^+ were numbered consecutively and denoted as I_0, I_1, …, I_8.)

Figure 16. Novel X-ray spectroscopy experiment on partially oriented PSII particles aiming at insights into the electronic structure of the OEC. In the measurement of fluorescence-detected X-ray absorption spectra, the X-ray fluorescence of the K_α emission line was detected at three emission energies (5898.0 eV, 5899.3 eV and 5900.0 eV) using a new experimental set-up for high-resolution X-ray emission spectroscopy (XES [173, 176]) at beamline ID26 of the European Synchrotron Radiation Facility (ESRF) in Grenoble. The shown edge spectra were collected for partially oriented PSII membrane particles at an angle of 15° between sample normal and the X-ray electric field vector. The spectra clearly depend on the selected emission energy. The pre-edge feature shown in the upper inset is of special interest because in this spectral region properties of the Mn *3d* orbitals are reflected. The pre-edge feature in the lower inset was obtained by averaging the spectra detected at the three emission energies, for excitation at 15° and 55°.

FIGURE 1

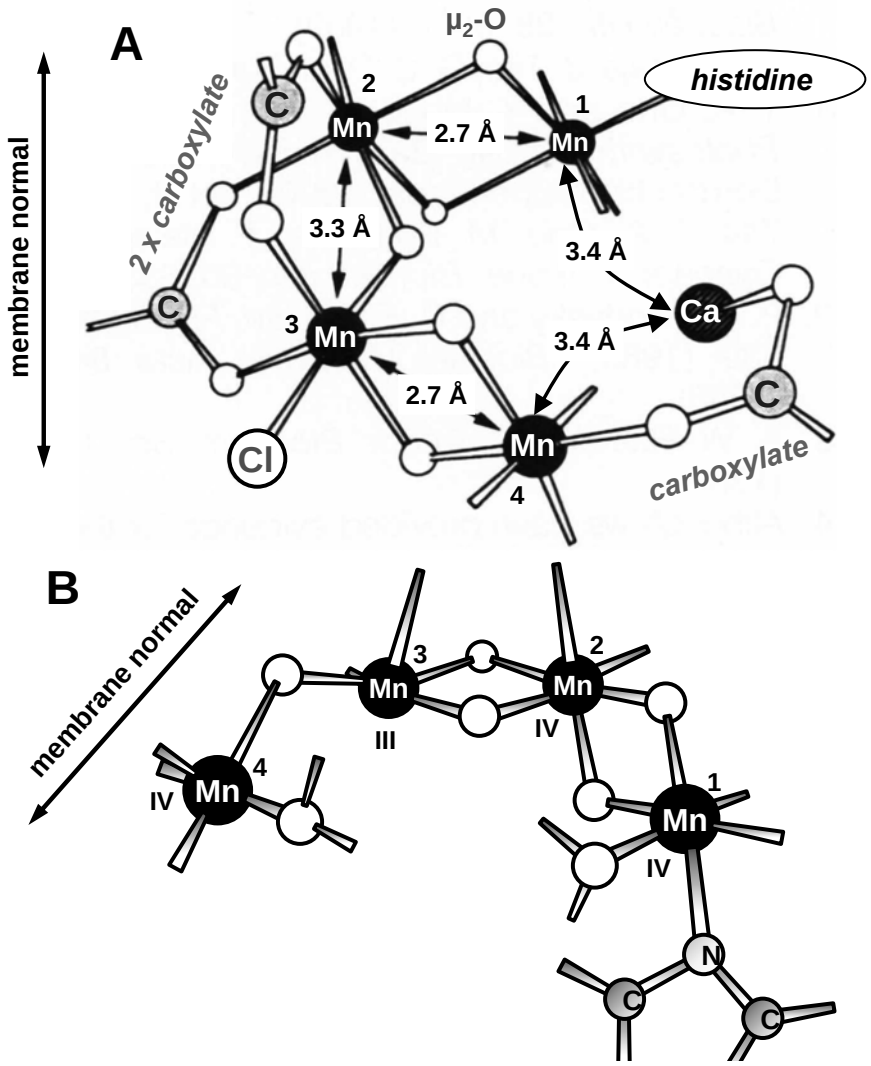

FIGURE 2

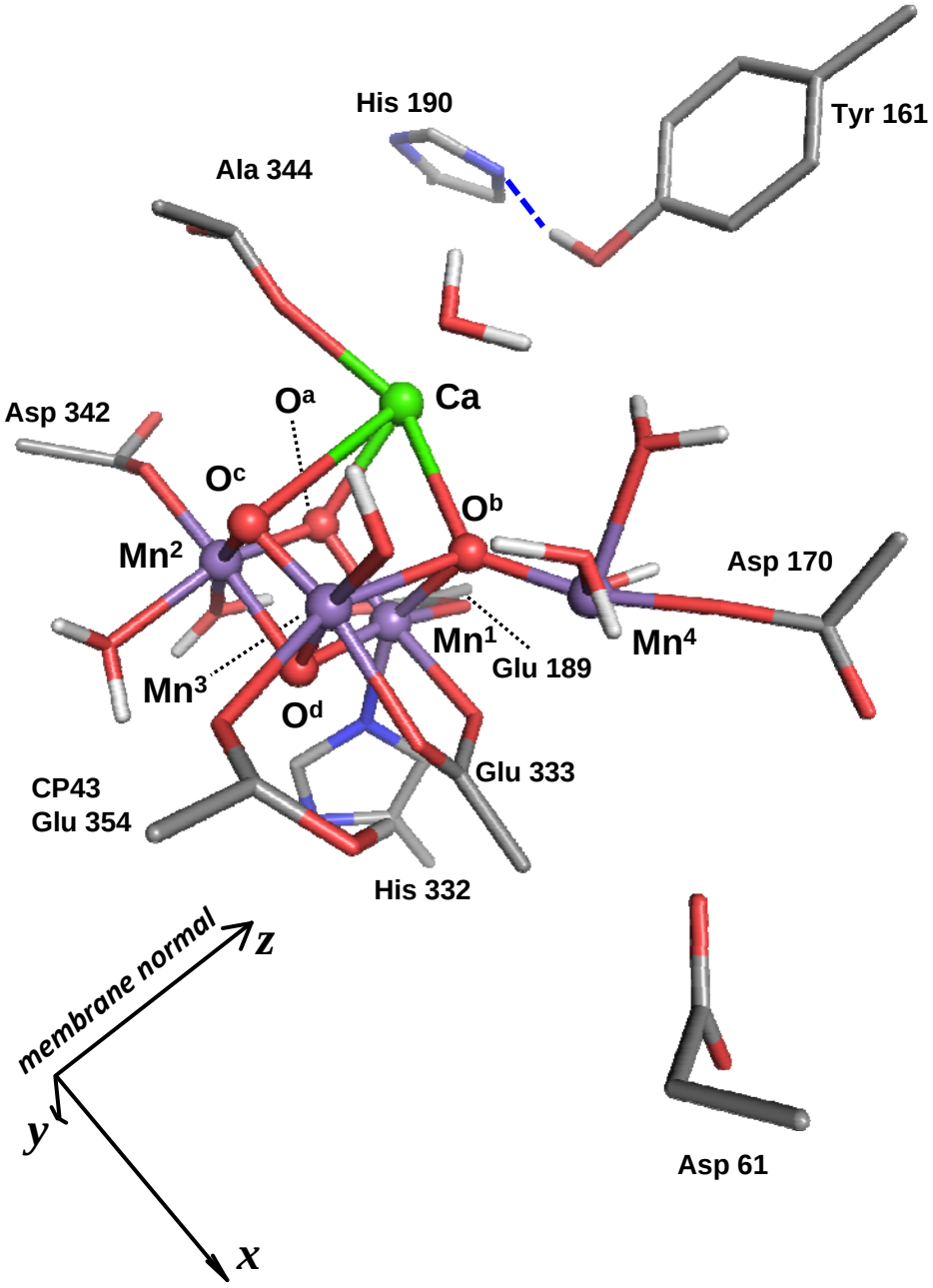

FIGURE 3

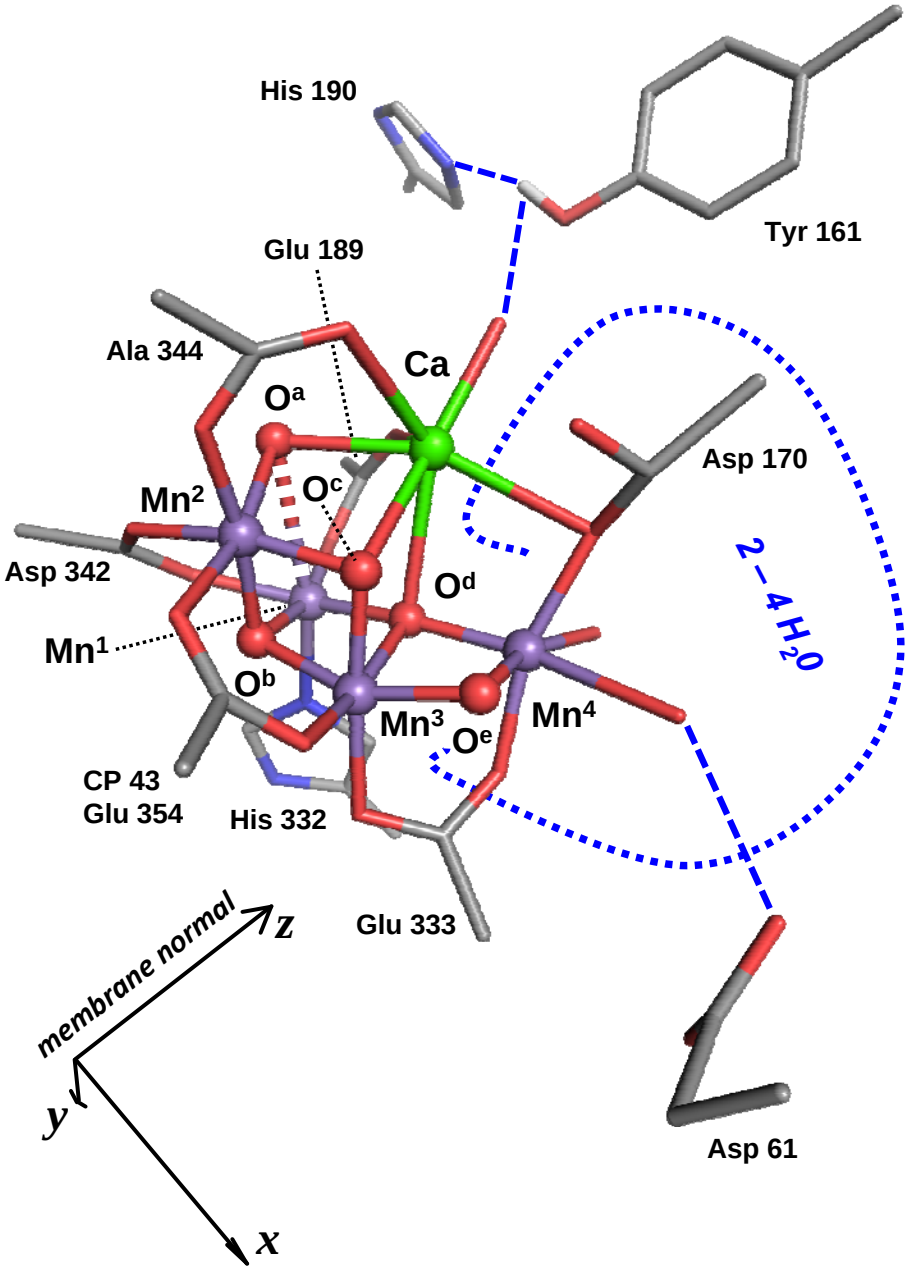

FIGURE 4

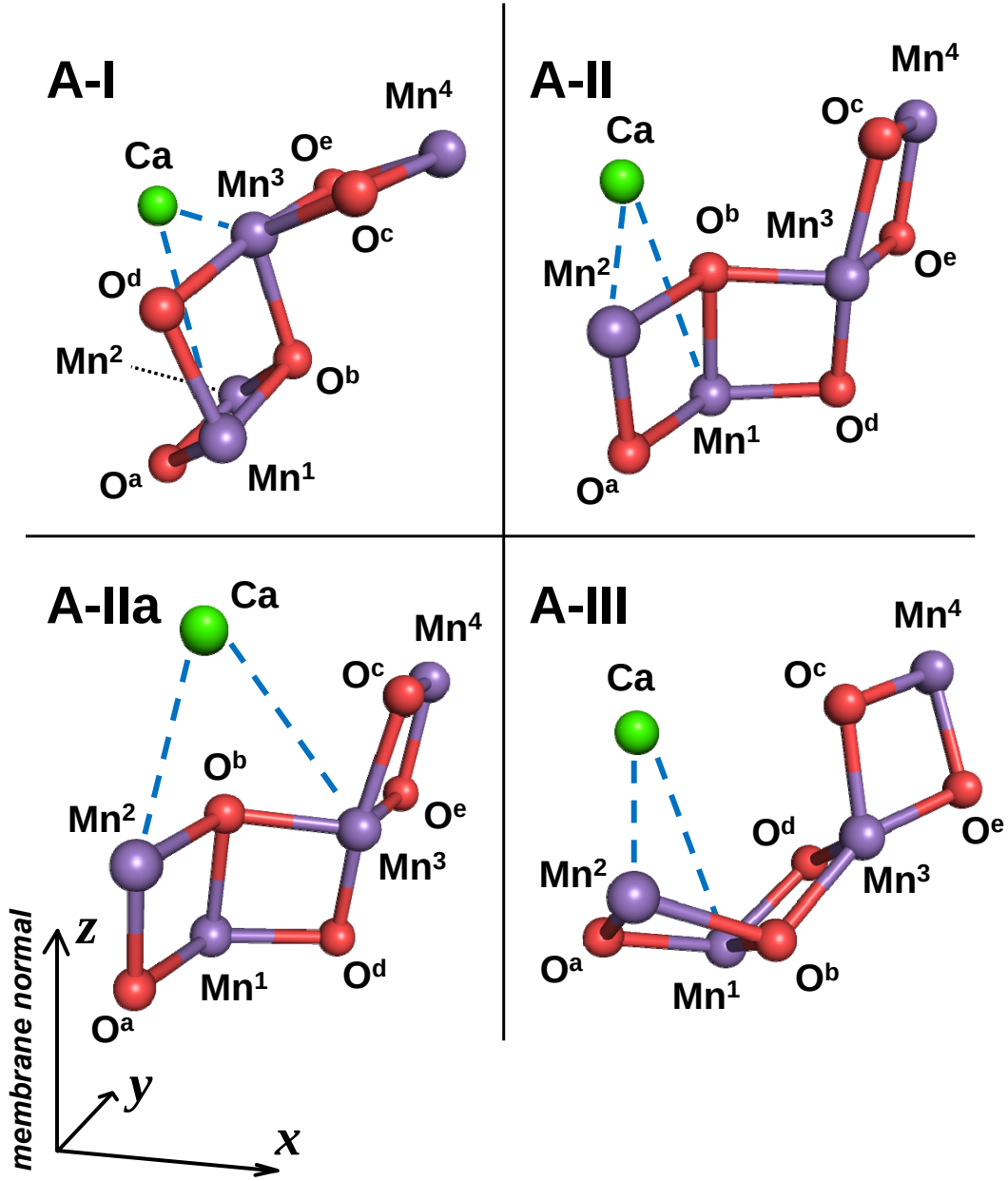

FIGURE 5A

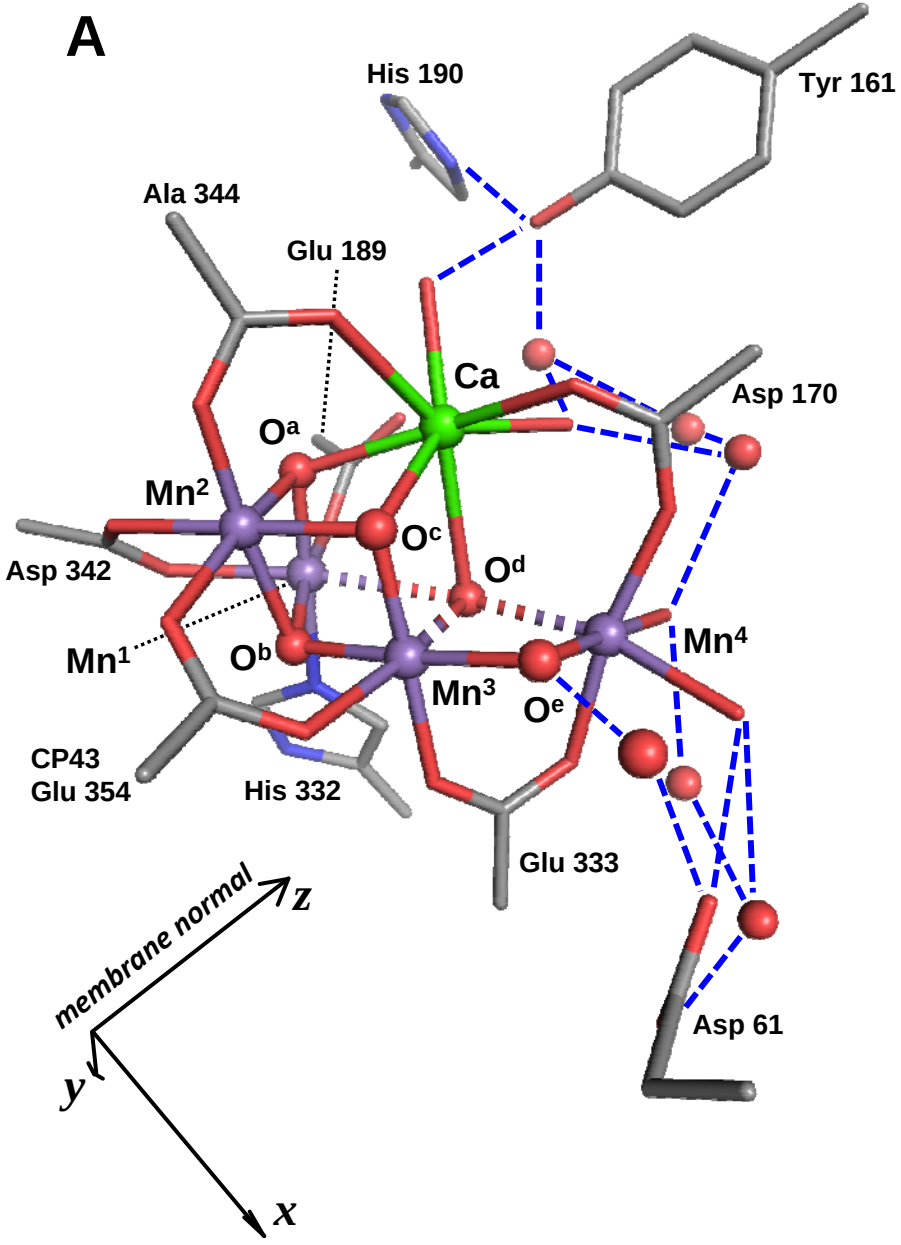

FIGURE 5B

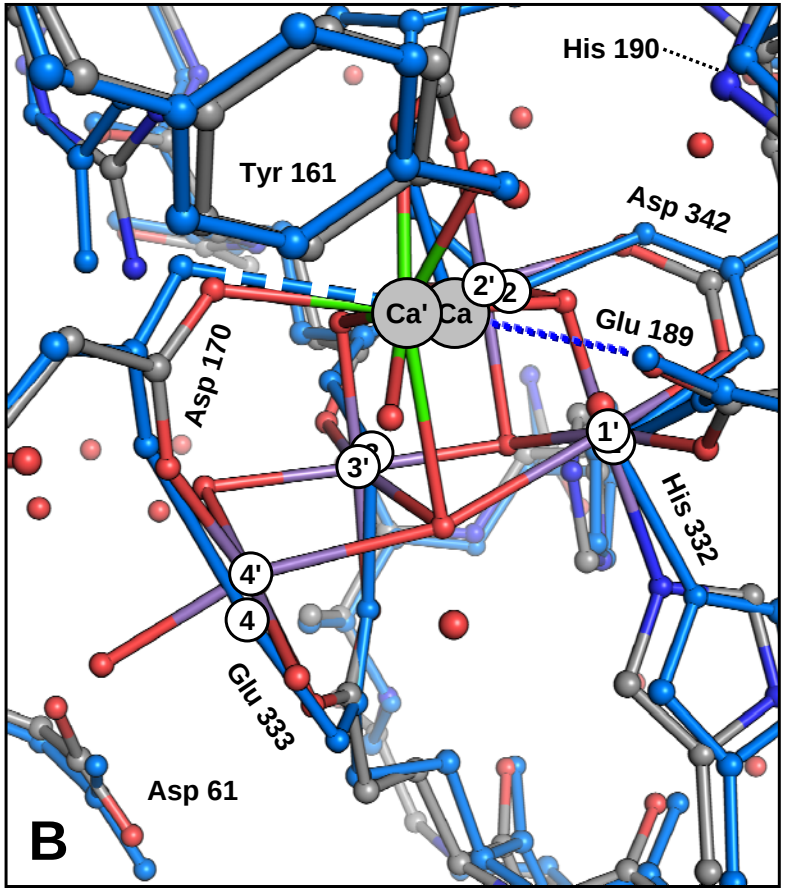

FIGURE 6

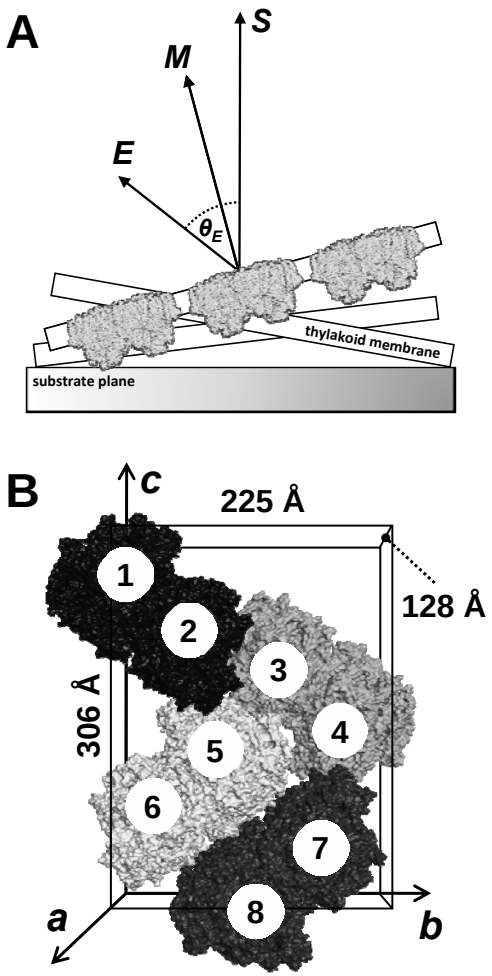

FIGURE 7

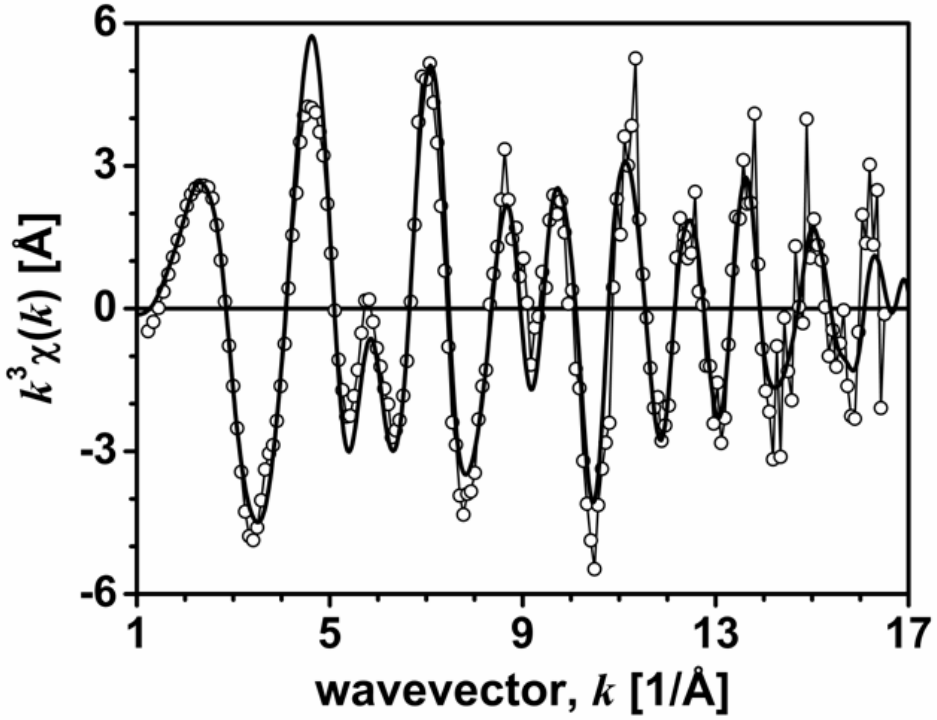

FIGURE 8

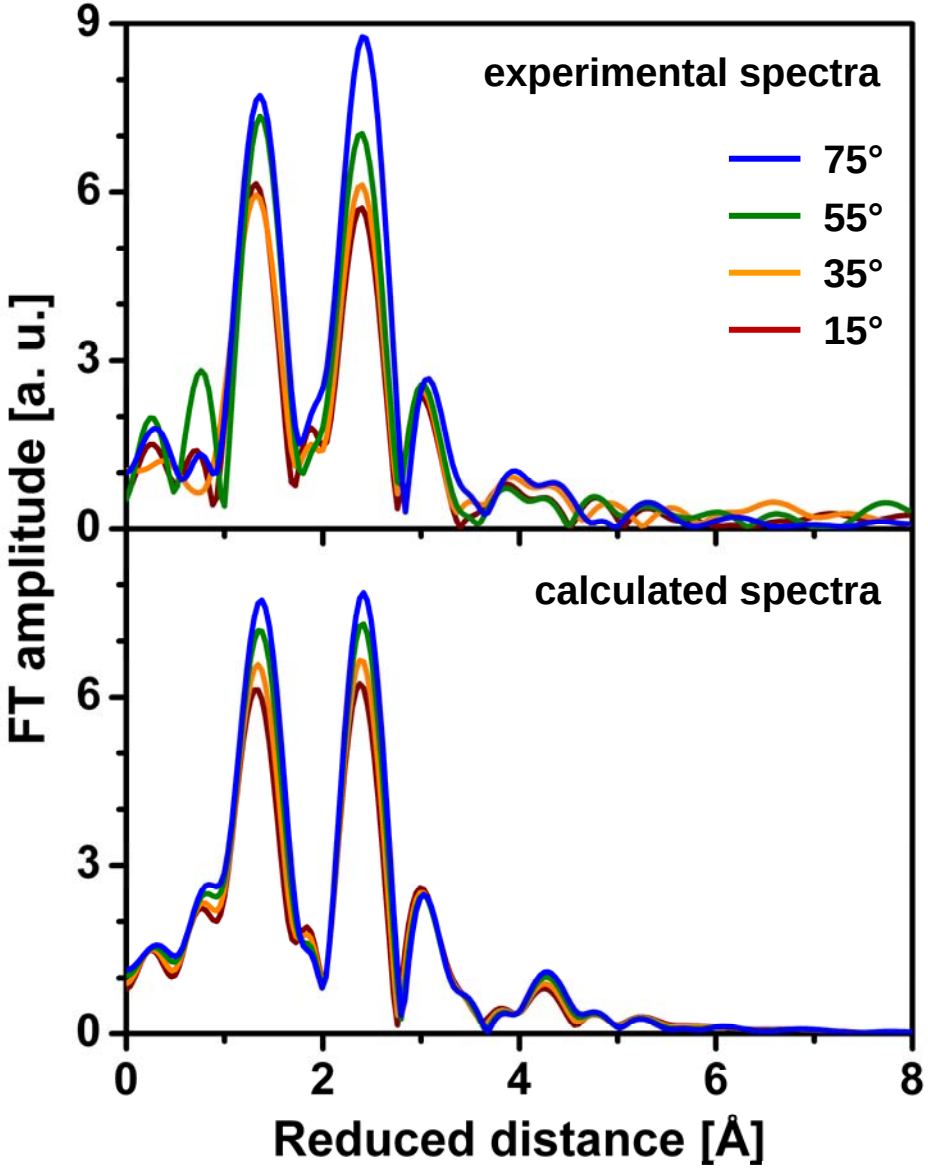

FIGURE 9

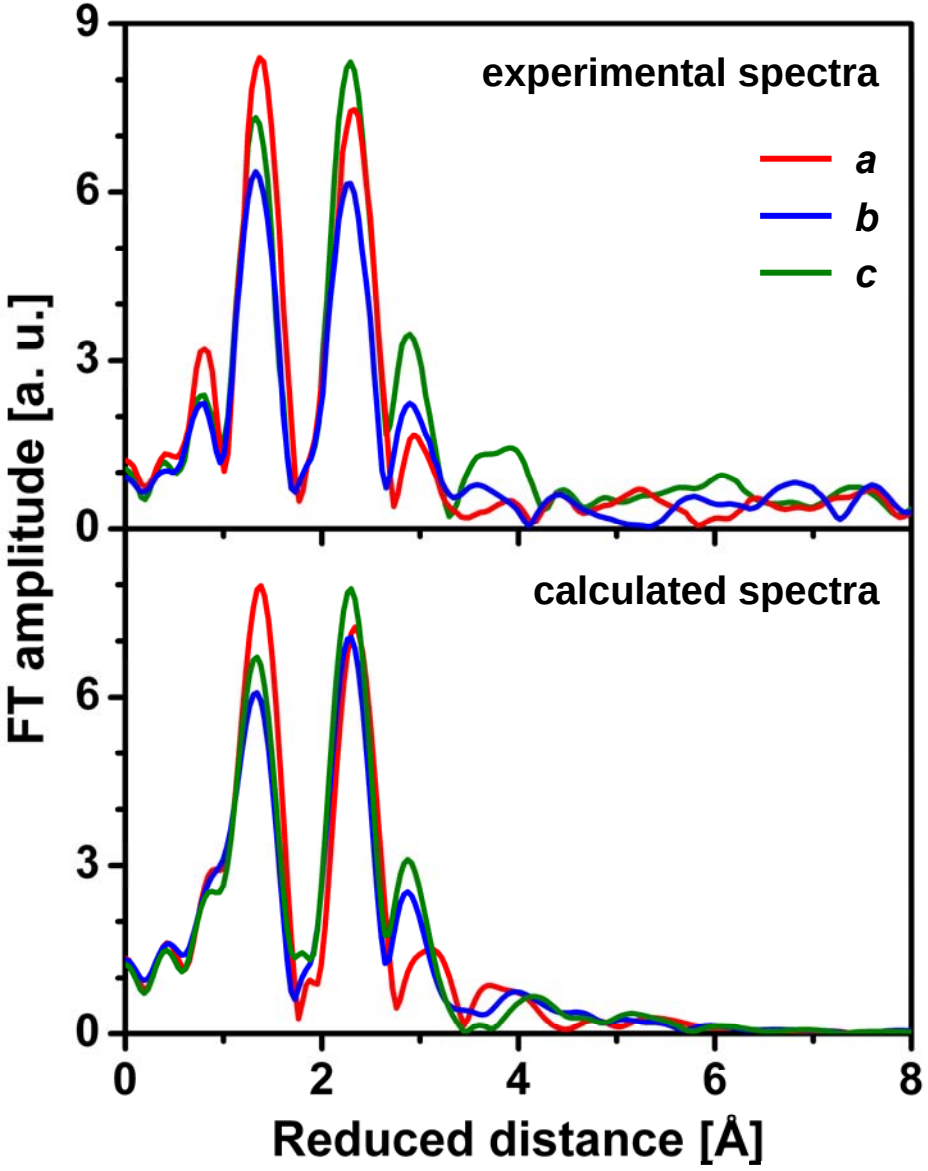

FIGURE 10

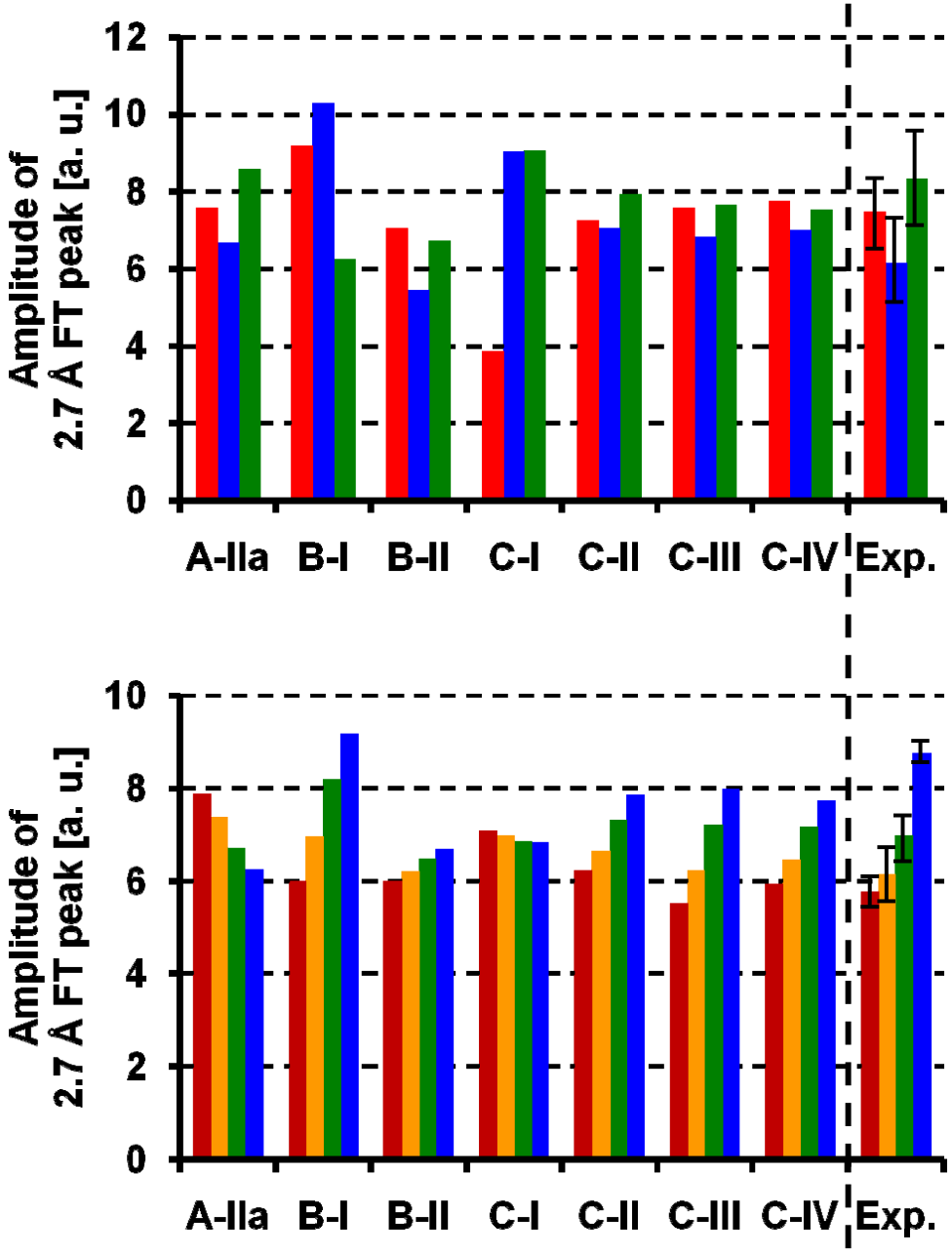

FIGURE 11

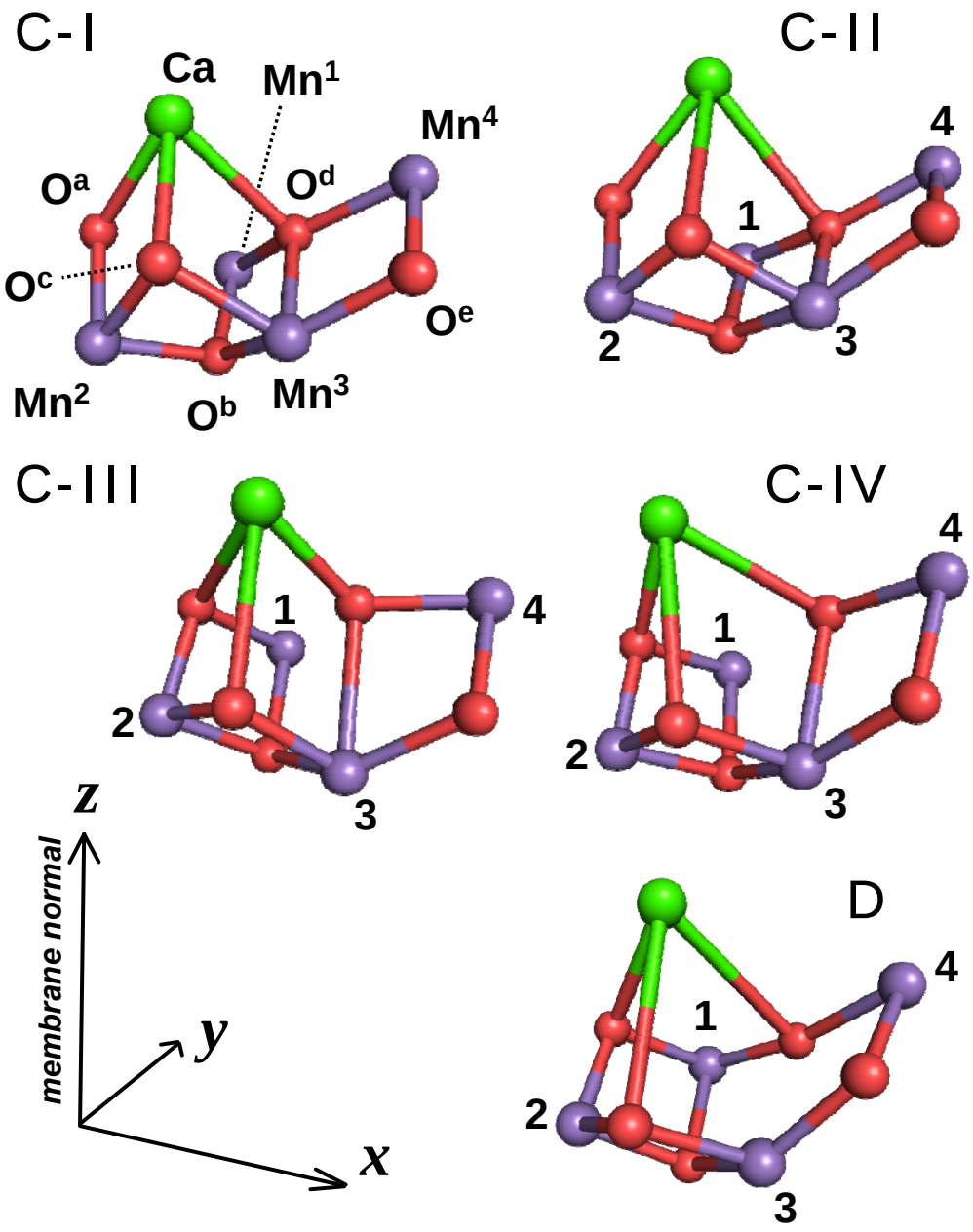

FIGURE 12

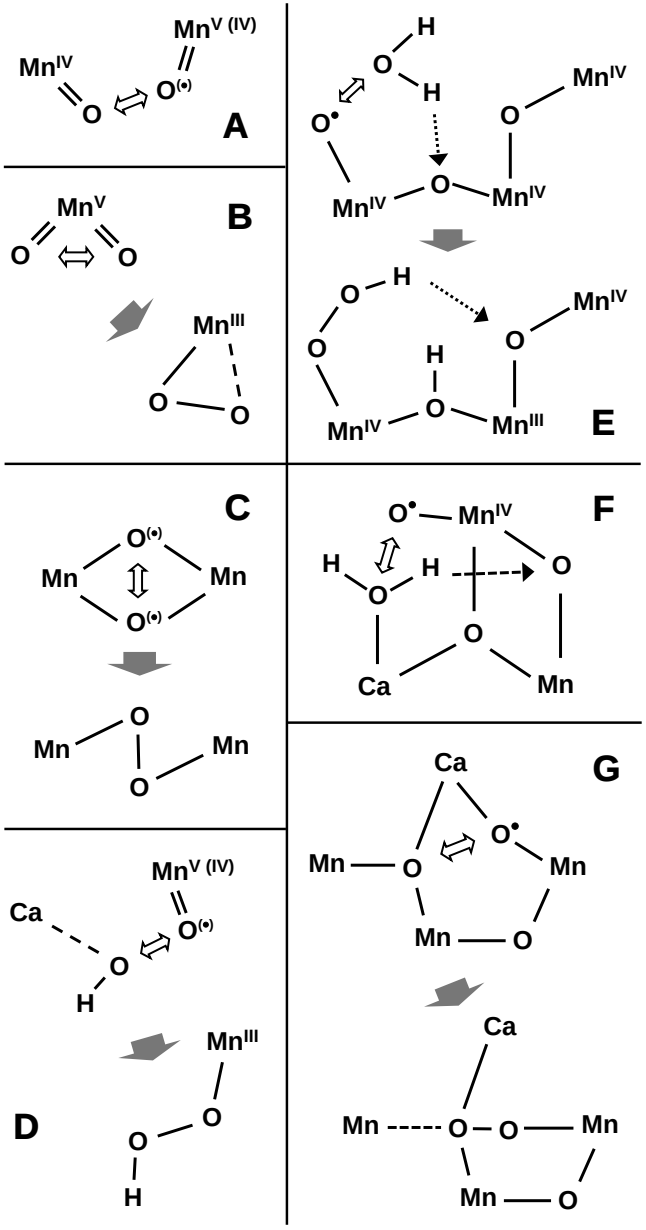

FIGURE 13

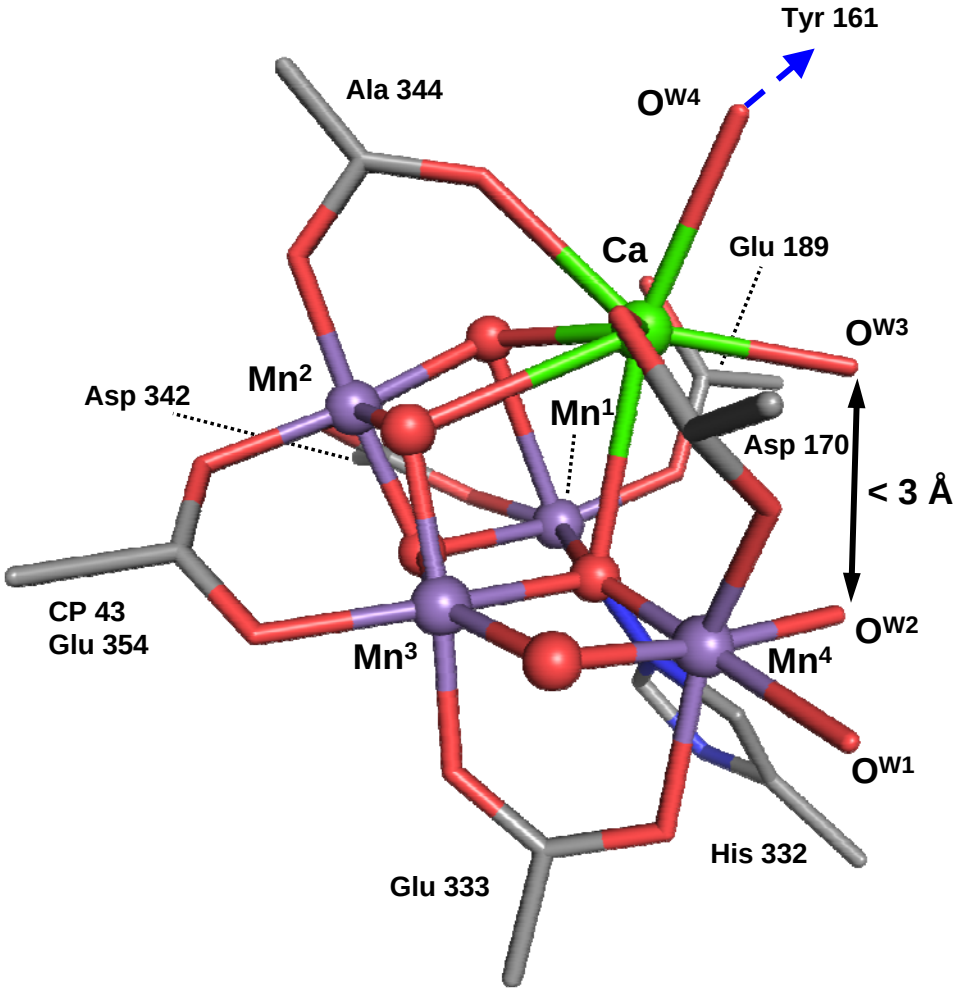

FIGURE 14

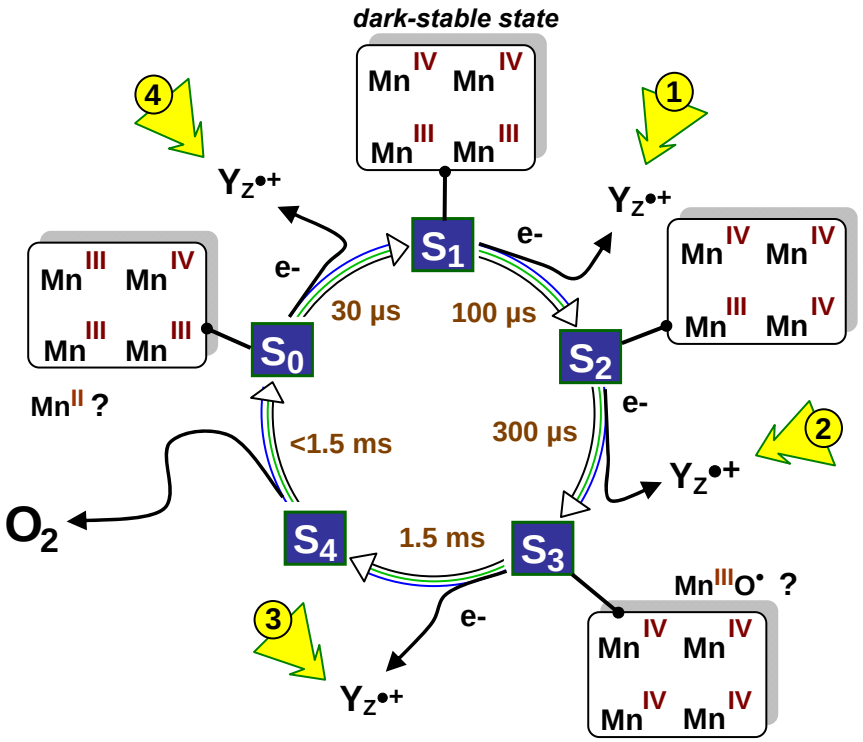

FIGURE 15

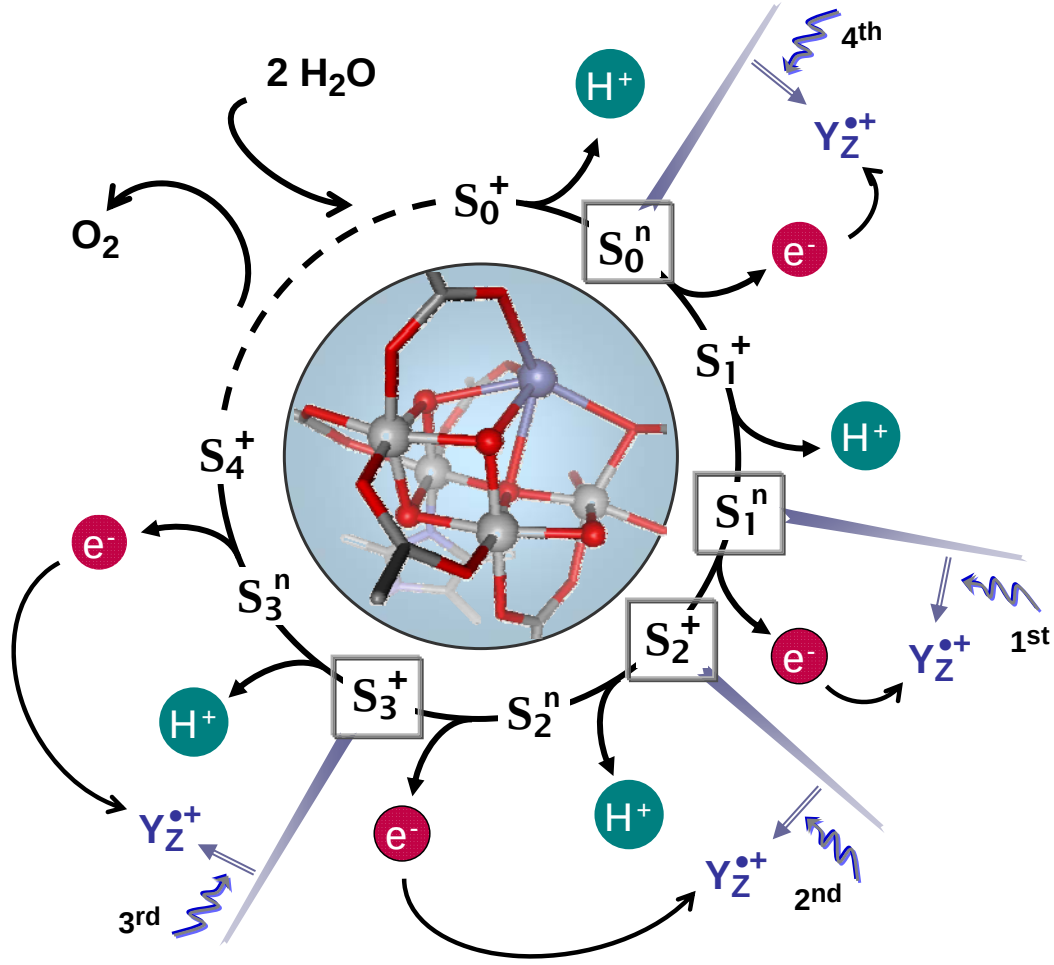

FIGURE 16

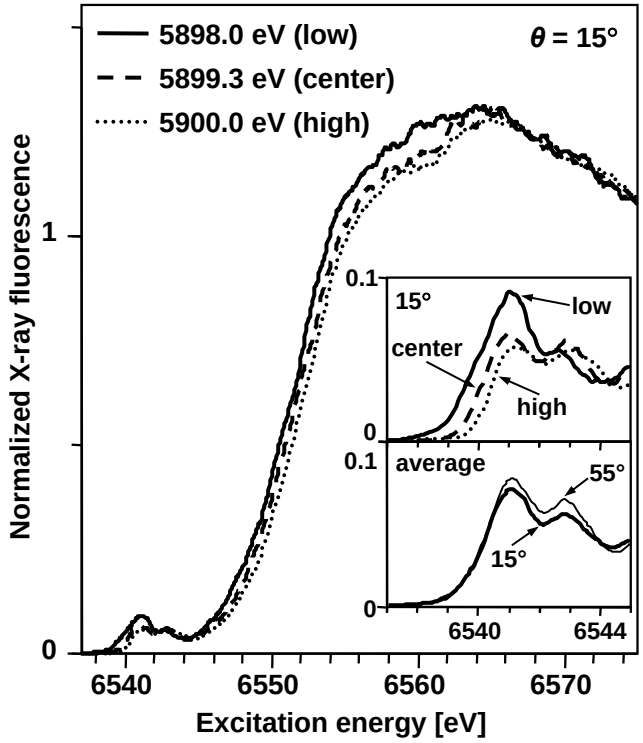
5898.0 eV (low)
5899.3 eV (center)
5900.0 eV (high)
θ = 15°
Normalized X-ray fluorescence
1
0
6540
6550
6560
6570
Excitation energy [eV]
0.1
15°
low
center
high
0
0.1
average
55°
15°
0
6540
6544

Figure S1

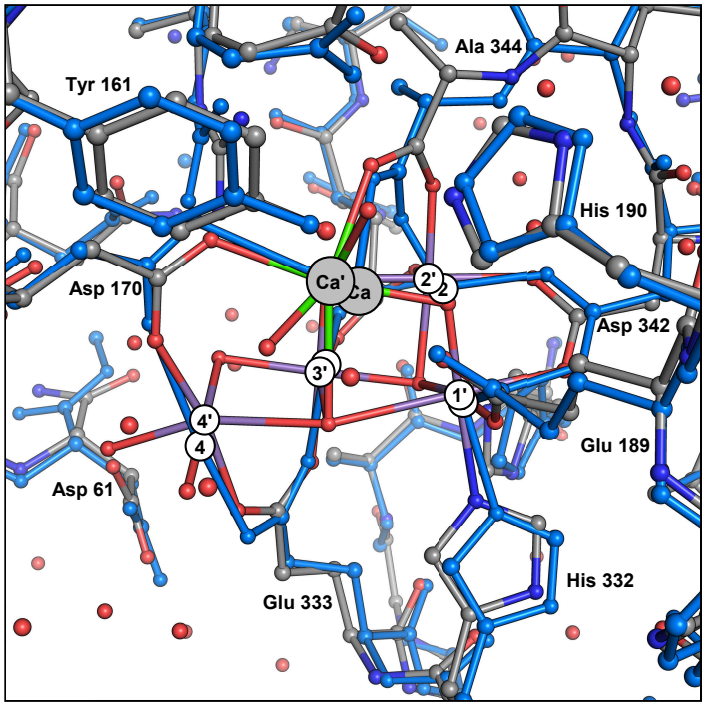

Overlay of the crystal structures determined by (i) Loll *et al,* Nature 438 (2005) 1040-1044 (protein data bank '2AXT'; blue) and (ii) Umena *et al,* Nature 473 (2011) 55-60 ('3ARC'; colored). The encircled numbers mark the positions of the respective Mn atoms for both XRD structures. Primed numbers as well as the label Ca' relate to the structure of Umena *et al*.

Figure S2

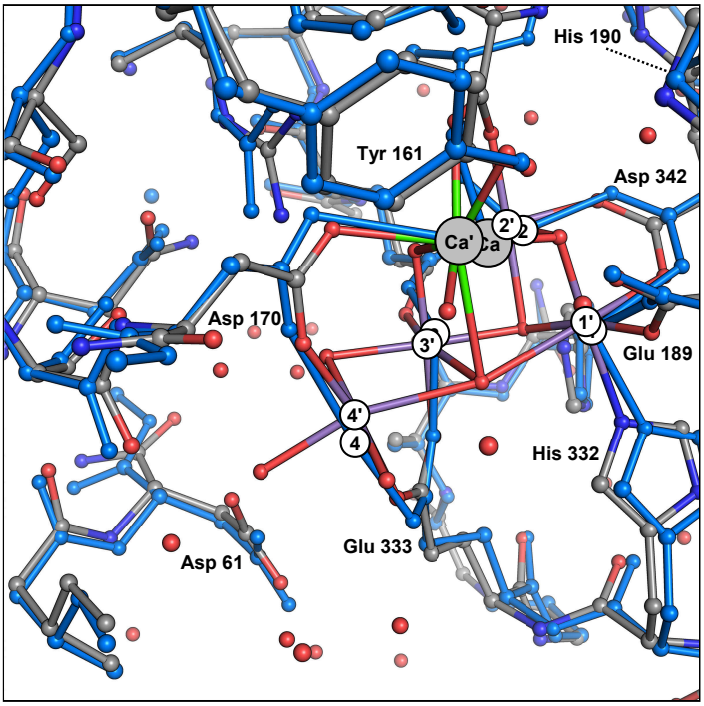

Overlay of the crystal structures determined by (i) Loll *et al,* Nature 438 (2005) 1040-1044 (protein data bank '2AXT'; blue) and (ii) Umena *et al,* Nature 473 (2011) 55-60 ('3ARC'; colored). The encircled numbers mark the positions of the respective Mn atoms for both XRD structures. Primed numbers as well as the label Ca' relate to the structure of Umena *et al*. This molecular graphic differs only by the viewing angle from Fig. S1.

Figure S3

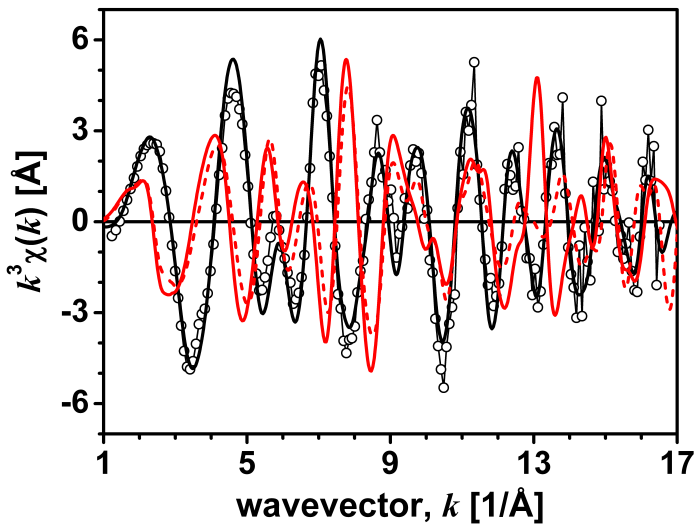

Comparison of experimental extended-range EXAFS data for isotropic PSII samples in the S_1 state (*Iso* data; open circles) with calculated spectra for (i) model D (black line) and (ii) monomer A (solid red line) and B (dashed red line) from XRD results ('3ARC') of Shen and coworkers (Umean *et al*, Nature 473 (2011) 55-60). The EXAFS data has been weighted by k^3. The spectra calculated for the individual PSII monomers differ only slightly at lower wavenumbers but more pronouncedly at higher wavenumbers. Both spectra calculated on the basis of the crystallographic coordinates are fully incompatible with the experimental spectra.

Figure S4

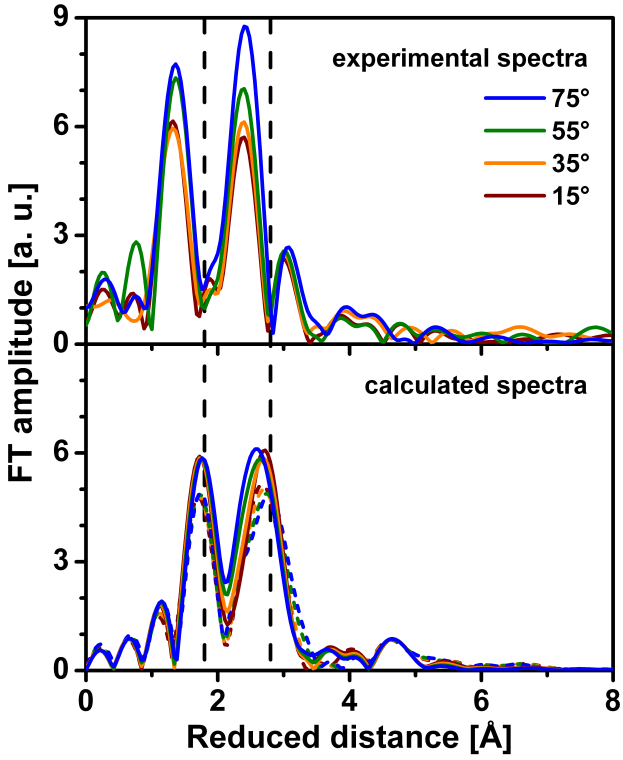

Fourier transform of polarized EXAFS spectra collected on partially oriented PSII membrane particles at four excitation angles (*Mem* and *Iso* data; top panel) and the corresponding spectra calculated for monomer A (solid lines) and B (dashed lines) of XRD results ('3ARC') from Shen and coworkers (Nature 473 (2011) 55-60; lower panel). Beginning and end of distance range covered by the second main peak of the experimental spectra are marked by dashed lines to emphasize the extreme deviations between experimental and the calculated spectra.

Figure S5

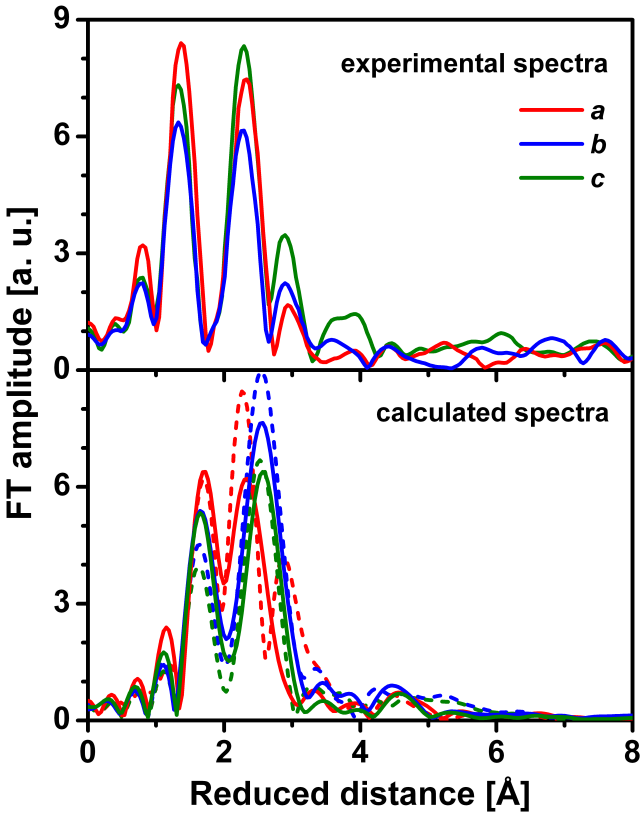

Fourier transform of polarized EXAFS spectra collected by Yano *et al* on PSII crystals (*Cry* data; top panel) and the corresponding spectra calculated for monomer A (solid lines) and B (dashed lines) of the XRD model ('3ARC') of Shen and coworkers (Nature 473 (2011) 55-60; lower panel). For both monomers, the calculated spectra differ pronouncedly from the experimental data.

Figure S6

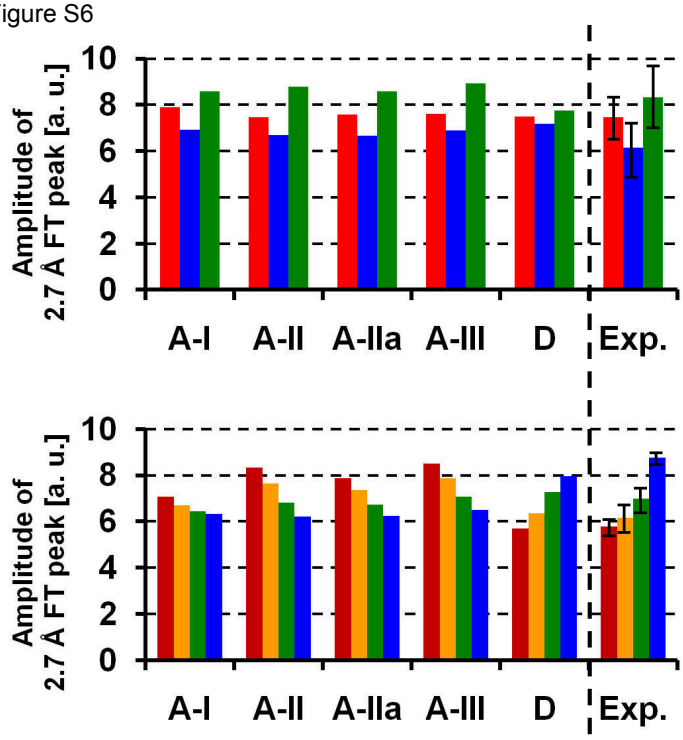

Bar diagram of the magnitude of the second FT peak calculated for models of Yano and coworkers (A-I, A-II, A-IIa, A-III; Science 314 (2006) 821-825) and a new model with a five-coordinated Mn^3 (D). The upper panel relates to the polarized EXAFS spectra obtained for PSII crystals (*Cry* data); the lower panel reflects the polarized EXAFS data collected on partially oriented PSII membrane particles (*Mem* data). The color coding in the lower and upper panel corresponds to the color codes used in Fig. 8 and Fig. 9, respectively. (The errors bars indicate the 2σ error estimated from the FT amplitudes at reduced distances ranging from 5.5 to 8.0 Å.)

Figure S7

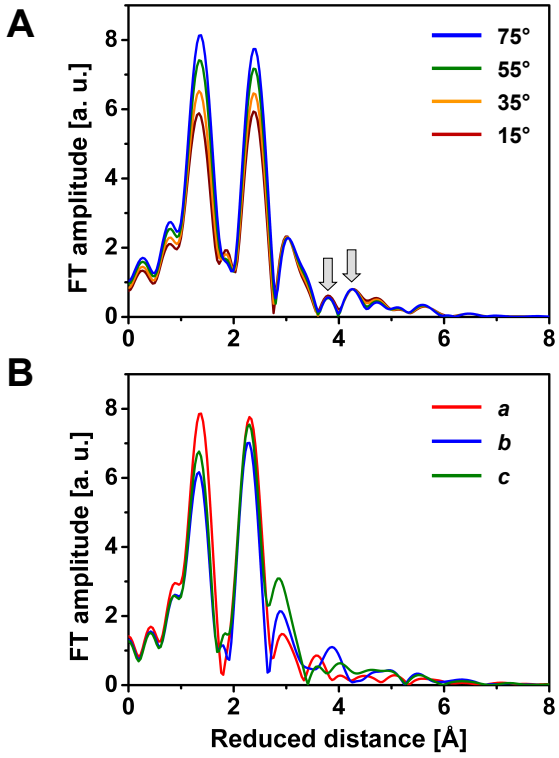

Fourier transform of calculated EXAFS spectra for model C-IV.
A. *Spectra for partially oriented PSII* membrane particles for four excitation angles (θ_E in Fig. 6).
B. *Spectra for PSII crystals* with the X-ray electric field vector aligned along one of the three crystal axes (*a*, *b*, *c*). The arrows in **A** mark Fourier peaks that may be present also in the experimental spectra. They relate to Mn-Mn vectors of about 4.3 Å and 4.8 Å length, respectively.

Figure S8

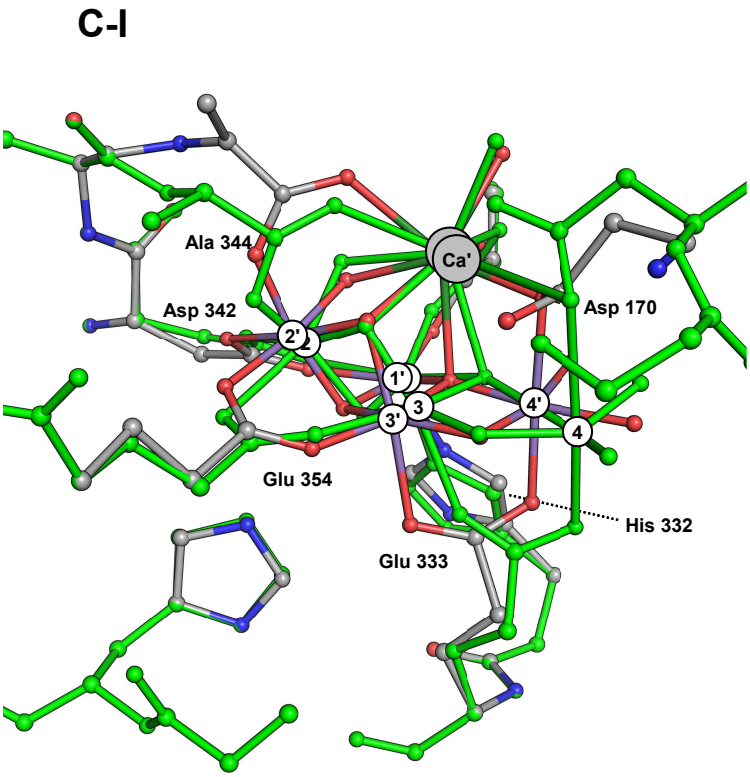

Overlay of (i) the crystal structure '2AXT' determined by Loll *et al,* Nature 438 (2005) 1040-1044 (bright green) and (ii) the OEC model C-I obtained by the optimization procedure described in section 3.3 (colored). The encircled numbers mark the positions of the Mn atoms for both structures. Primed numbers as well as the label Ca' relate to the structure of model C-I.

Figure S9

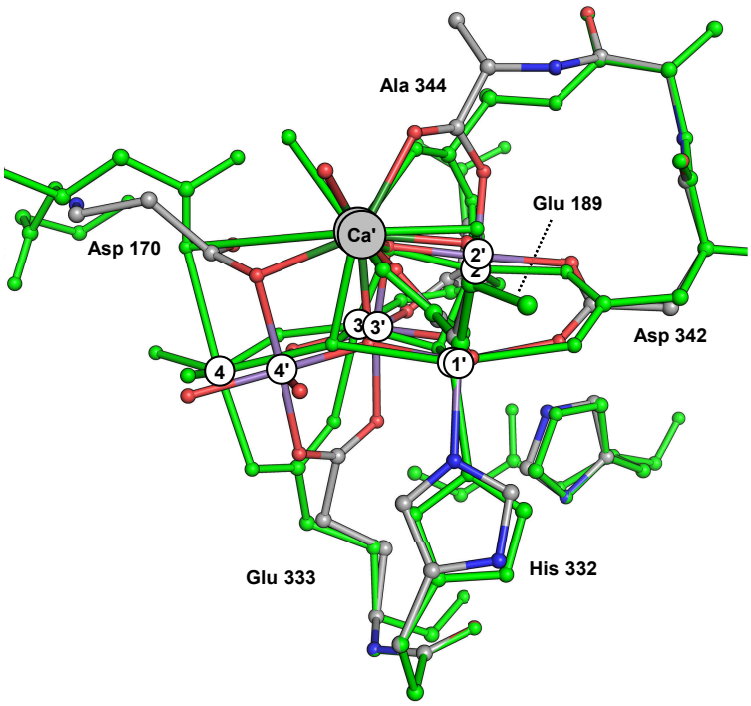

Overlay of (i) the crystal structure '2AXT' determined by Loll *et al,* Nature 438 (2005) 1040-1044 (bright green) and (ii) the OEC model C-I obtained by the optimization procedure described in section 3.3 (colored). The encircled numbers mark the positions of the Mn atoms for both structures. Primed numbers as well as the label Ca' relate to the structure of model C-I. This molecular graphic differs only by the viewing angle from Fig. S8.

Figure S10

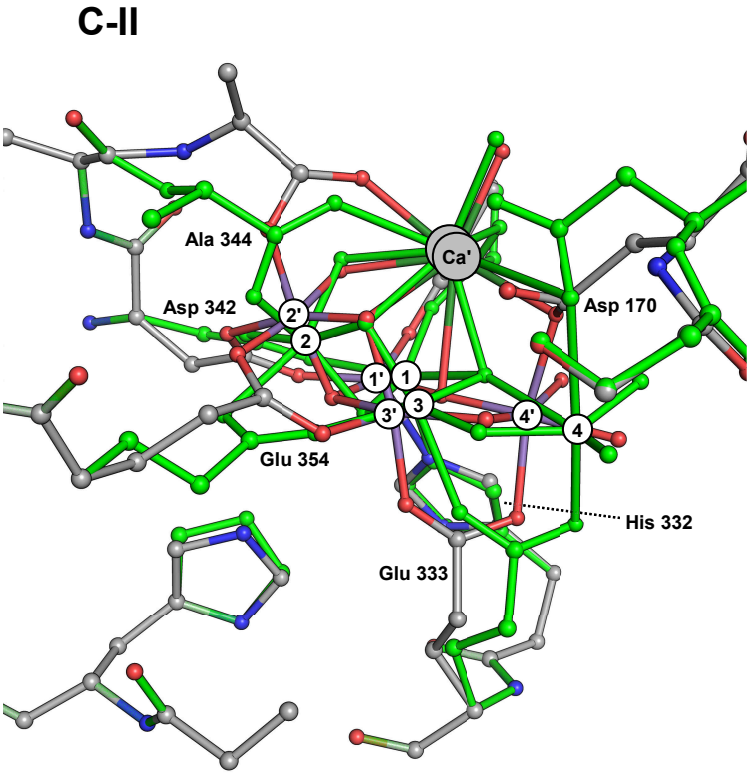

Overlay of (i) the crystal structure '2AXT' determined by Loll *et al,* Nature 438 (2005) 1040-1044 (bright green) and (ii) the OEC model C-II obtained by the optimization procedure described in section 3.3 (colored). The encircled numbers mark the positions of the Mn atoms for both structures. Primed numbers as well as the label Ca' relate to the structure of model C-II.

Figure S11

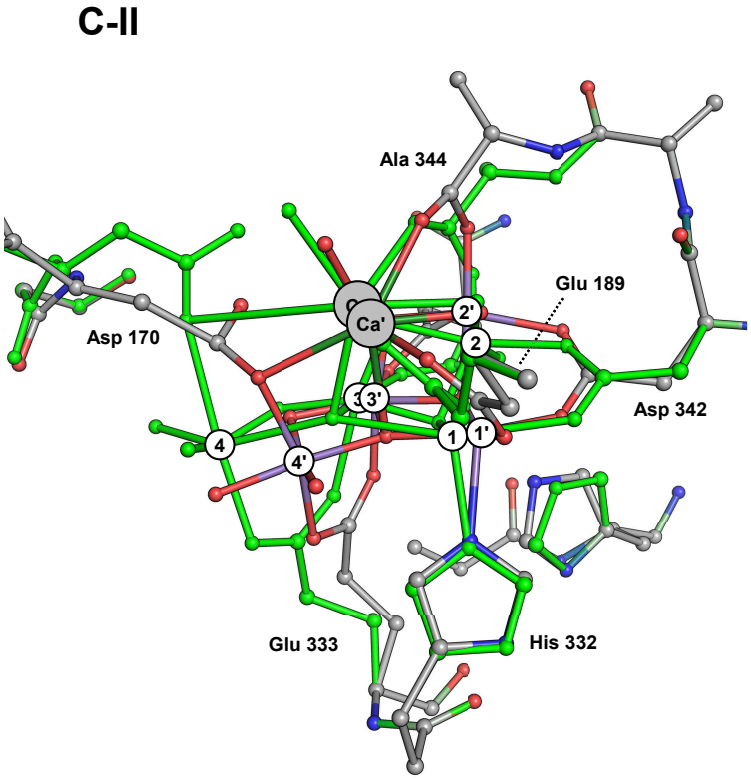

Overlay of (i) the crystal structure '2AXT' determined by Loll *et al,* Nature 438 (2005) 1040-1044 (bright green) and (ii) the OEC model C-II obtained by the optimization procedure described in section 3.3 (colored). The encircled numbers mark the positions of the Mn atoms for both structures. Primed numbers as well as the label Ca' relate to the structure of model C-II. This molecular graphic differs only by the viewing angle from Fig. S10.

Figure S12

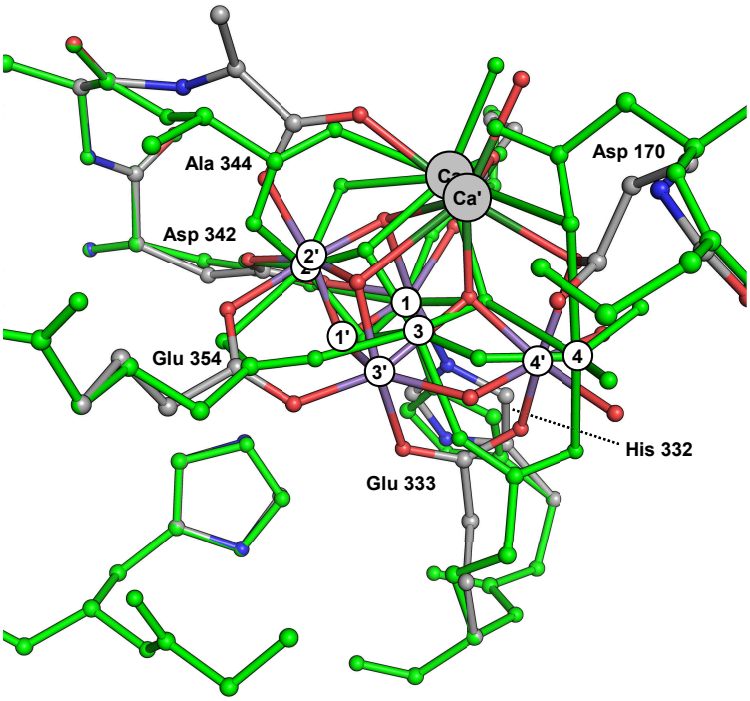

Overlay of (i) the crystal structure '2AXT' determined by Loll *et al,* Nature 438 (2005) 1040-1044 (bright green) and (ii) the OEC model C-III obtained by the optimization procedure described in section 3.3 (colored). The encircled numbers mark the positions of the Mn atoms for both structures. Primed numbers as well as the label Ca' relate to the structure of model C-III.

Figure S13

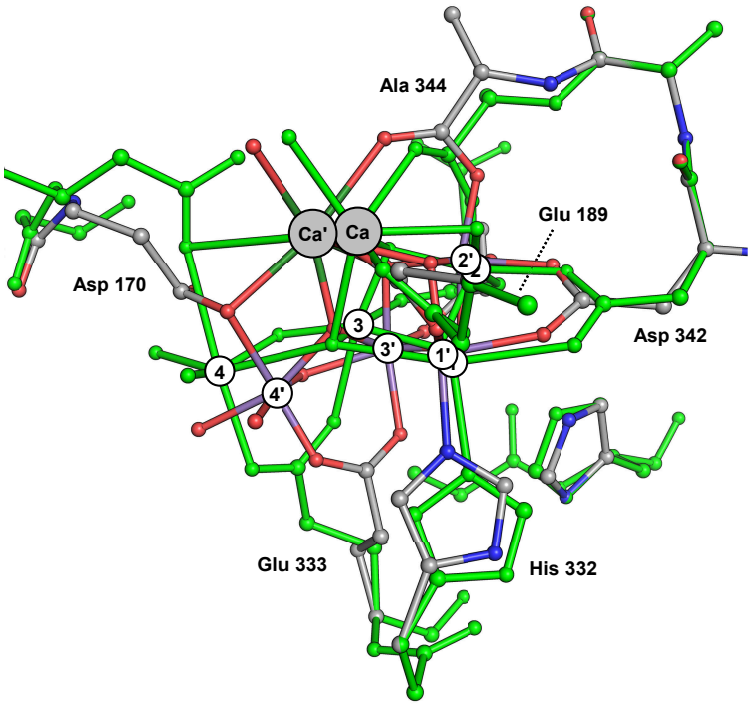

Overlay of (i) the crystal structure '2AXT' determined by Loll *et al,* Nature 438 (2005) 1040-1044 (bright green) and (ii) the OEC model C-III obtained by the optimization procedure described in section 3.3 (colored). The encircled numbers mark the positions of the Mn atoms for both structures. Primed numbers as well as the label Ca' relate to the structure of model C-III. This molecular graphic differs only by the viewing angle from Fig. S8.

Figure S14

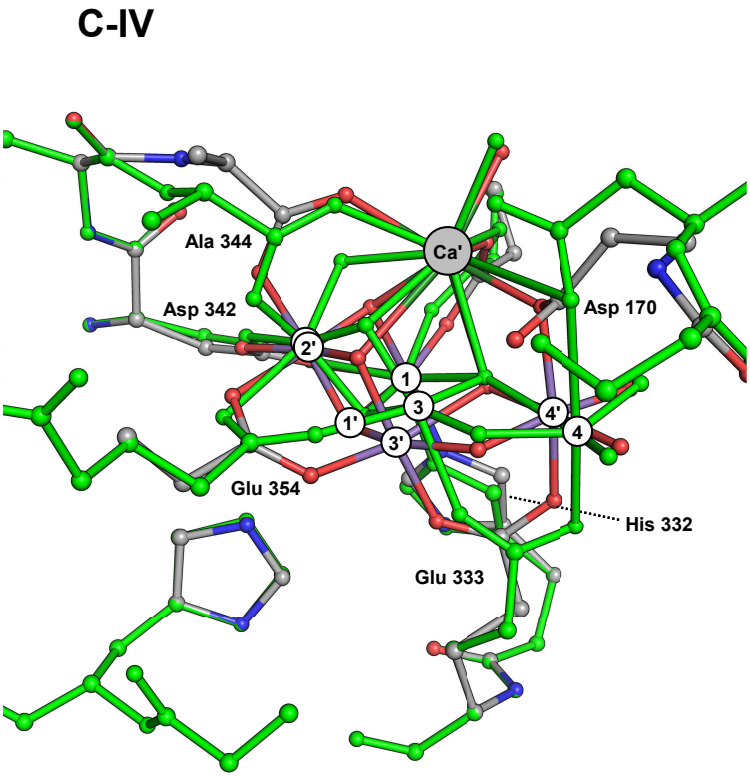

Overlay of (i) the crystal structure '2AXT' determined by Loll *et al,* Nature 438 (2005) 1040-1044 (bright green) and (ii) the OEC model C-IV obtained by the optimization procedure described in section 3.3 (colored). The encircled numbers mark the positions of the Mn atoms for both structures. Primed numbers as well as the label Ca' relate to the structure of model C-IV.

Figure S15

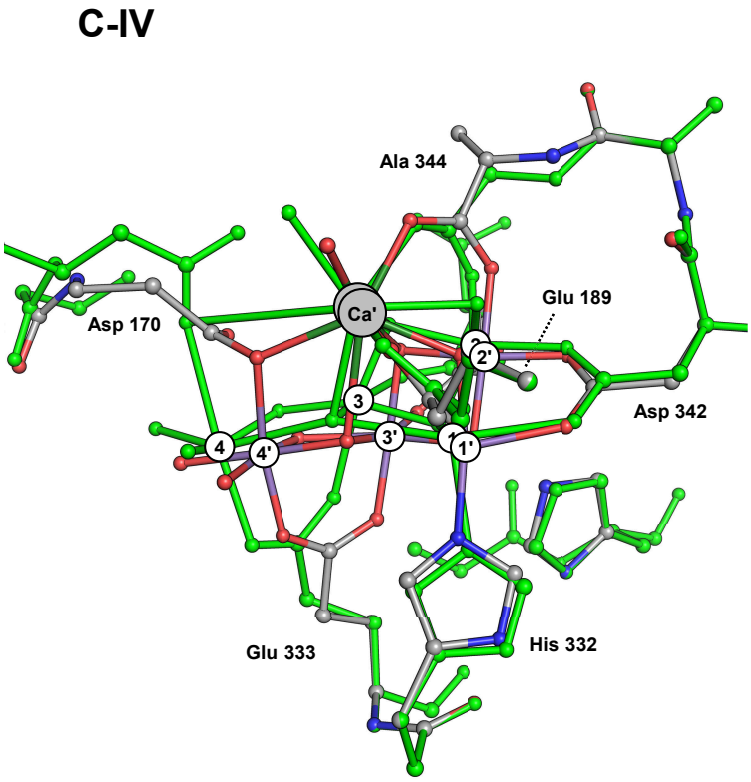

Overlay of (i) the crystal structure '2AXT' determined by Loll *et al,* Nature 438 (2005) 1040-1044 (bright green) and (ii) the OEC model C-IV obtained by the optimization procedure described in section 3.3 (colored). The encircled numbers mark the positions of the Mn atoms for both structures. Primed numbers as well as the label Ca' relate to the structure of model C-IV. This molecular graphic differs only by the viewing angle from Fig. S14.

Figure S16

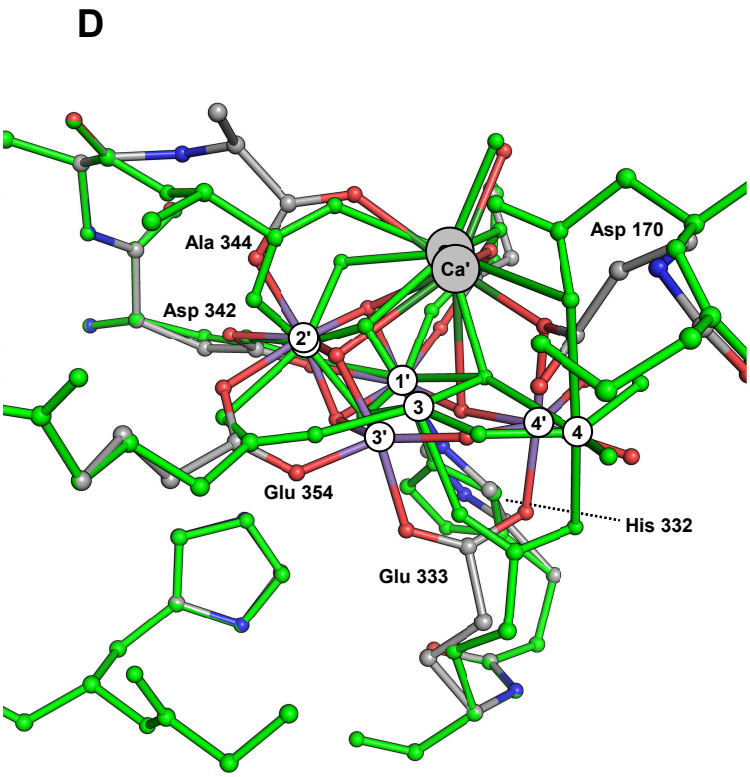

Overlay of (i) the crystal structure '2AXT' determined by Loll *et al,* Nature 438 (2005) 1040-1044 (bright green) and (ii) the OEC model D obtained by the optimization procedure described in section 3.3 (colored). The encircled numbers mark the positions of the Mn atoms for both structures. Primed numbers as well as the label Ca' relate to the structure of model D.

Figure S17

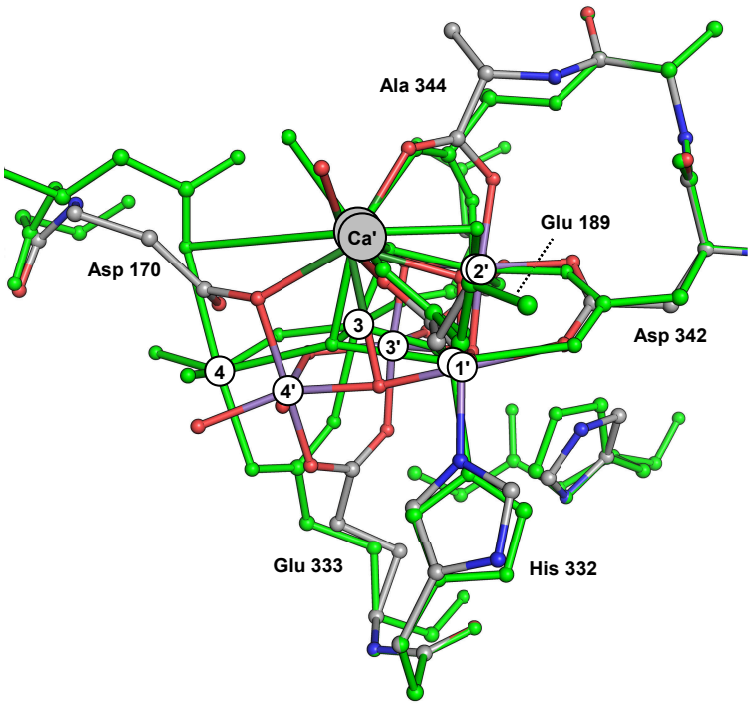

Overlay of (i) the crystal structure '2AXT' determined by Loll *et al,* Nature 438 (2005) 1040-1044 (bright green) and (ii) the OEC model D obtained by the optimization procedure described in section 3.3 (colored). The encircled numbers mark the positions of the Mn atoms for both structures. Primed numbers as well as the label Ca' relate to the structure of model D. This molecular graphic differs only by the viewing angle from Fig. S16.

Table S1

	A-I		A-IIa		A-II		A-III		D	
									Mn^3-O^d > 2.4 Å	
atom pair	*R*/Å	θ_R	*R*/Å	θ_R	*R*/Å	θ_R	*R*/Å	θ_R	*R*/Å	θ_R
Mn^1-Mn^2	**2.81**	**86°**	**2.80**	**57°**	**2.80**	**60°**	**2.80**	**63°**	**2.72**	**78°**
Mn^1-Mn^3	**2.70**	**23°**	**2.70**	**50°**	**2.70**	**46°**	**2.72**	**47°**	3.17	79°
Mn^1-Mn^4	4.74	40°	4.96	41°	4.96	36°	4.97	35°	3.70	63°
Mn^2-Mn^3	3.26	34°	3.28	86°	3.28	81°	3.25	80°	**2.71**	**89°**
Mn^2-Mn^4	4.94	38°	5.50	66°	5.49	61°	5.46	59°	4.82	62°
Mn^3-Mn^4	**2.73**	**65°**	**2.72**	**42°**	**2.72**	**38°**	**2.72**	**35°**	3.03	40°
Mn^1-Ca	4.94	58°	4.36	6°	3.41	29°	3.40	27°	3.34	41°
Mn^2-Ca	3.40	33°	3.39	34°	3.41	62°	3.40	59°	3.26	18°
Mn^3-Ca	3.40	88°	3.40	40°	3.75	73°	3.73	71°	3.63	30°
Mn^4-Ca	5.04	78°	3.61	81°	4.41	76°	4.38	76°	3.37	76°
Mn-Ca avg. angle	4.19	60°	3.69	41°	3.75	58°	3.73	56°	3.40	41°
Error	6.5		5.6		5.8		6.6		1.3	

Metal-metal distances (*R*) and angles between metal-metal vector and membrane normal (θ_R) for models A-I, A-II, A-IIa, and A-III proposed in Yano *et al*, Science 314 (2006) 821-825 (shown in Fig. 4) and the alternative model D with a five-coordinated Mn^3 (compare Fig. 11). In the last row, an error sum is given (in arbitrary units), which provides a measure of the deviations between calculated and experimental spectra taking into account the *Iso*, *Mem*, and *Cry* data sets (see section 3).

Table S2

(i)

N [1]	Mn-O [Å]	oxidation state
5	2.13	**2**
5	1.95	**3**
5	1.84	**4**
6	2.20	**2**
6	2.02	**3**
6	1.90	**4**

(ii) Dimer:

	N [1]	Mn-O [Å]	oxidation state
Mn^1	5	1.98	**2.8**
Mn^2	6	2.08	**2.7**
Mn^3	6	2.12	**2.5**
Mn^4	6	2.18	**2.1**
Mean oxidation state			**2.5**

(iii) Monomer A:

	N [1]	Mn-O [Å]	oxidation state
Mn^1	5	1.99	**2.7**
Mn^2	6	2.08	**2.6**
Mn^3	6	2.13	**2.4**
Mn^4	6	2.19	**2.0**

(iv) Monomer B:

	N [1]	Mn-O [Å]	oxidation state
Mn^1	5	1.97	**2.9**
Mn^2	6	2.07	**2.7**
Mn^3	6	2.10	**2.5**
Mn^4	6	2.17	**2.2**

Estimation of oxidation states from Mn-O bond lengths.

(i) *Typical lengths of Mn-O bonds* (second column) for five-coordinated (*N* = 5 in first column) and six-coordinated manganese ions (*N* = 6) for different formal oxidation states (third column). The bond lengths were calculated using the bond-valence method, assuming identical bond lengths for all ligands. (Values from Table 2 of Brese and O'Keeffe, Acta Cryst. B47, 1991, 192-197).

(ii) *Estimated formal oxidation states* for the Mn atoms of the PSII dimer (PDB coordinates '3ARC'; model of Umena *et al*, Nature 473 (2011) 55-60). In the third column, the averaged Mn-O distances for the two Mn complexes of the dimer are shown, assuming that Mn^1 is five-coordinated (*N* = 5) and the other Mn atoms are six-coordinated (*N* = 6). The fractional oxidation states in the fourth column were calculated from the average bond lengths using the data of Table (i) and linear interpolation. Averaged Mn-O distances and formal oxidation states for the two individual PSII monomers are shown in **(iii)** and **(iv)**.